



© Copyright by Ted Chu, December 2014  
All Rights Reserved

PART I - GEOSTATISTICAL INTERPOLATION OF RAIN FIELDS USING  
RADAR ESTIMATES AND GAUGE OBSERVATIONS: ALGORITHM DESIGN  
AND AUTOMATION

PART II - ENERGY DISSIPATION IN FLUID FLOWS AND WAVE  
TRANSFORMATION BY POROUS BARRIERS AND SUBMERGED CAVITIES

A Dissertation

Presented to

the Faculty of the Department of Civil Engineering

University of Houston

In Partial Fulfillment

of the Requirements for the Degree

Doctor of Philosophy

in Civil Engineering

by

Ted Chu

December 2014

PART I - GEOSTATISTICAL INTERPOLATION OF RAIN FIELDS USING  
RADAR ESTIMATES AND GAUGE OBSERVATIONS: ALGORITHM DESIGN  
AND AUTOMATION

PART II - ENERGY DISSIPATION IN FLUID FLOWS AND WAVE  
TRANSFORMATION BY POROUS BARRIERS AND SUBMERGED CAVITIES

---

Ted Chu

Approved:

---

Chair of the Committee  
Keh-Han Wang, Professor,  
Civil and Environmental Engineering

Committee Members:

---

Yi-Lung Mo, Professor,  
Civil and Environmental Engineering

---

Kyle B. Strom, Associate Professor,  
Civil and Environmental Engineering

---

Ali K. Kamrani, Associate Professor,  
Industrial Engineering

---

Hyongki Lee, Assistant Professor,  
Civil and Environmental Engineering  
Geosensing Systems Engineering and Science

---

Suresh K. Khator, Associate Dean,  
Cullen College of Engineering

---

Roberto Ballarini, Professor and Chair,  
Civil and Environmental Engineering

## Acknowledgements

I would like to thank my wife, Ruth, and son, Jayden, for accompanying me on this journey. There had been times when juggling between school and work became really difficult, especially in the past few months, and I am so thankful that both of you provided me with so much support, encouragement, and love so that I could finish this study.

I also want to thank Dr. Keh-Han Wang for his guidance and, most importantly, allowing me total freedom to carry out this research work. I was able to select the topics that I was interested in, and to design the strategies to conduct the experiments and other tasks as well as complete the dissertation.

Finally, the financial support provided by the Department of Education through the GAANN fellowship must be acknowledged.

PART I - GEOSTATISTICAL INTERPOLATION OF RAIN FIELDS USING  
RADAR ESTIMATES AND GAUGE OBSERVATIONS: ALGORITHM DESIGN  
AND AUTOMATION  
PART II - ENERGY DISSIPATION IN FLUID FLOWS AND WAVE  
TRANSFORMATION BY POROUS BARRIERS AND SUBMERGED CAVITIES

An Abstract of a Dissertation  
Presented to  
the Faculty of the Department of Civil Engineering  
University of Houston

In Partial Fulfillment  
of the Requirements for the Degree  
Doctor of Philosophy  
in Civil Engineering

by  
Ted Chu  
December 2014

## Abstract

This research consists of two parts. The first part aims to improve the accuracy of rain field interpolation with the utilization of radar rainfall during extreme storm events for a study watershed. The second part studies the head loss induced by fluids passing through porous screens and the wave transformation caused by porous barriers as well as submerged cavities. In the first part of the study, the regression-kriging (RK) and merging spatial interpolation techniques were applied to predict rain fields using radar rainfall estimates as an auxiliary variable for the Chenyulan River watershed in Taiwan. Severe property damage and loss of lives are often inevitable at the times of typhoons. Reliable warning systems are of great importance to provide the emergency response agencies with vital information for early action planning. The developed algorithms were tested against univariate methods, such as the ordinary kriging, with five historical typhoon events. The results have shown that the accuracy of rainfall prediction could be significantly improved by the proposed algorithms and multivariate techniques are superior to univariate methods, especially where sampling condition is inadequate. Porous media have many practical engineering applications. Porous screens are commonly seen at the inlets of wastewater treatment plants for the removal of coarse trash. Porous barriers are generally used to reduce wave motions in coastal regions by dissipating the incoming wave energy. This part of the research emphasized on the head loss induced by fluids passing through porous screens. The effects of screen pore size, porosity, and angle of inclination were investigated experimentally, and empirical relationships which could potentially be used to predict head loss were deduced. The wave transformation caused by porous barriers was the next topic to be studied. Analytical solutions based on the linear wave theory using a potential flow approach with the adoption of Darcy's law as a boundary condition were derived. The analytical results were validated by experimental data collected in this study. Finally, the induced vortices and fluid particle entrainment process as solitary waves propagated past a submerged cavity were studied experimentally. The PLIF technique was used to visualize the wave field and evolved vortices around the cavity zone. The maximum transporting distance of bottom fluid particles was analyzed with measured data and compared to the available numerical results.

# Table of Contents

<b>Acknowledgements</b> . . . . .	<b>v</b>
<b>Abstract</b> . . . . .	<b>vii</b>
<b>Table of Contents</b> . . . . .	<b>viii</b>
<b>List of Figures</b> . . . . .	<b>x</b>
<b>List of Tables</b> . . . . .	<b>xiii</b>
<b>Nomenclature</b> . . . . .	<b>xiv</b>
<b>I Geostatistical Interpolation of Rain Fields Using Radar Estimates and Gauge Observations: Algorithm Design and Automation</b> . . . . .	<b>1</b>
<b>1 Introduction</b> . . . . .	<b>2</b>
<b>2 Literature Review</b> . . . . .	<b>5</b>
<b>3 Study Area</b> . . . . .	<b>9</b>
<b>4 Rainfall Data</b> . . . . .	<b>12</b>
4.1 Rain Gauge Observations . . . . .	12
4.2 Radar Rainfall Estimates . . . . .	14
4.3 Historical Typhoon Events . . . . .	15
<b>5 Rain Field Interpolation</b> . . . . .	<b>19</b>
5.1 Regression-Kriging . . . . .	19
5.2 Merging . . . . .	22
<b>6 Automation</b> . . . . .	<b>26</b>
<b>7 Results</b> . . . . .	<b>28</b>
7.1 Typhoon Kalmaegi . . . . .	30
7.2 Typhoon Morakot . . . . .	36
7.3 Typhoons Fungwong, Sinlaku, and Fanapi . . . . .	41
7.4 Significance of Auxiliary Predictors . . . . .	45
<b>8 Conclusions and Future Studies</b> . . . . .	<b>63</b>

<b>II Energy Dissipation in Fluid Flows and Wave Transformation by Porous Barriers and Submerged Cavities . . . . .</b>	<b>65</b>
<b>9 Introduction . . . . .</b>	<b>66</b>
<b>10 Literature Review . . . . .</b>	<b>70</b>
<b>11 Theoretical Background . . . . .</b>	<b>74</b>
11.1 Head Loss . . . . .	74
11.2 Wave Transformation Caused by a Vertically Placed Porous Barrier . . . . .	75
<b>12 Experimentation on Head Loss Induced by Porous Screens and Wave Transformation Caused by Obstructing Structures . . . . .</b>	<b>83</b>
12.1 Head Loss Induced by Flows through a Porous Screen . . . . .	83
12.2 Wave Transformation Caused by a Porous Barrier . . . . .	85
12.3 Wave Transformation Caused by a Submerged Cavity . . . . .	89
<b>13 Results . . . . .</b>	<b>94</b>
13.1 Flow Head Loss Induced by a Porous Screen . . . . .	94
13.2 Wave Transformation Caused by a Porous Barrier . . . . .	101
13.3 Wave Transformation Caused by a Submerged Cavity and Visualization of Flow Patterns . . . . .	107
13.3.1 Flow Field Visualization . . . . .	110
13.3.2 Displacement of Moving Fluid Particles and Transport of Trench Contents . . . . .	115
<b>14 Conclusions and Future Studies . . . . .</b>	<b>122</b>
<b>References . . . . .</b>	<b>125</b>

## List of Figures

1.1	Road damage in Taiwan, caused by Typhoon Morakot in August 2009. . . . .	3
3.1	Location and elevation distribution of study area. . . . .	9
3.2	Slope distribution of study area. . . . .	11
4.1	Rain gauge network covering study area. . . . .	13
4.2	Sample time slice of radar rainfall, Typhoon Morakot in August 2009. . . . .	15
4.3	Track of Typhoon Kalmaegi, July 2008, photo courtesy of CWB. . . . .	16
4.4	Track of Typhoon Fungwong, July 2008, photo courtesy of CWB. . . . .	17
4.5	Track of Typhoon Sinlaku, September 2008, photo courtesy of CWB. . . . .	17
4.6	Track of Typhoon Morakot, August 2009, photo courtesy of CWB. . . . .	18
4.7	Track of Typhoon Fanapi, September 2010, photo courtesy of CWB. . . . .	18
5.1	Sample trend surface of rainfall variation, Typhoon Morakot in August 2009. . . . .	21
5.2	Sample residual surface of rainfall variation, Typhoon Morakot in August 2009. . . . .	22
5.3	Sample semivariogram fitted with spherical model, Typhoon Morakot in August 2009. . . . .	23
5.4	Sample gauge-based interpolated rainfall surface, Typhoon Morakot in August 2009. . . . .	24
5.5	Sample interpolated surface of adjustment values, Typhoon Morakot in August 2009. . . . .	25
6.1	Automated processing sequence of rain field interpolation. . . . .	26
7.1	Peak hour hyetograph comparisons, Typhoon Kalmaegi. . . . .	34
7.2	Full event hyetograph comparisons at station C1I060, Typhoon Kalmaegi. . . . .	35
7.3	Adjusted radar rainfall v.s. gauge observations, Typhoon Kalmaegi. . . . .	36
7.4	Peak hour hyetograph comparisons, Typhoon Morakot. . . . .	40
7.5	Full event hyetograph comparisons at station C1I060, Typhoon Morakot. . . . .	41
7.6	Adjusted radar rainfall v.s. gauge observations, Typhoon Morakot. . . . .	42
7.7	2-D rain fields, 23:00 08/08/2009, Typhoon Morakot. . . . .	43
7.8	2-D rain fields, 00:00 08/09/2009, Typhoon Morakot. . . . .	43
7.9	2-D rain fields, 01:00 08/09/2009, Typhoon Morakot. . . . .	44
7.10	Peak hour hyetograph comparisons for interpolation error investigation, Typhoon Fungwong. . . . .	53
7.11	Peak hour hyetograph comparisons for interpolation error investigation, Typhoon Fanapi. . . . .	54
7.12	Peak hour hyetograph comparisons, Typhoon Fungwong. . . . .	55
7.13	Peak hour hyetograph comparisons, Typhoon Sinlaku. . . . .	56
7.14	Peak hour hyetograph comparisons, Typhoon Fanapi. . . . .	57
7.15	Full event hyetograph comparisons at station C1I060, Typhoon Fungwong. . . . .	58
7.16	Full event hyetograph comparisons at station C1I060, Typhoon Sinlaku. . . . .	58

7.17	Full event hyetograph comparisons at station C1I060, Typhoon Fanapi. . . . .	59
7.18	Adjusted radar rainfall v.s. gauge observations, Typhoon Fungwong. . . . .	60
7.19	Adjusted radar rainfall v.s. gauge observations, Typhoon Sinlaku. . . . .	61
7.20	Adjusted radar rainfall v.s. gauge observations, Typhoon Fanapi. . . . .	62
9.1	Inlet bar screen system of a wastewater treatment plant, photo courtesy of <a href="http://kusterszima.com">http://kusterszima.com</a> . . . . .	66
9.2	Porous breakwater, photo courtesy of <a href="http://cdn.physorg.com">http://cdn.physorg.com</a> . . . . .	67
11.1	Profile view of fluid domain. . . . .	74
11.2	Profile view of fluid domain. . . . .	76
12.1	Flume (left) and main components of recirculation system (right). . . . .	84
12.2	1/4" diameter, 40.31% porosity (left), and 1/8" diameter, 40.31% porosity (right). . . . .	85
12.3	Speedy velocity sensor (left), and Ultra 5 controller (right) by Pulsar. . . . .	86
12.4	Wave maker. . . . .	87
12.5	Wave gauge calibration relationships. . . . .	87
12.6	Wave flume configuration with a porous screen. . . . .	88
12.7	Porous screen configured perpendicularly to direction of incident waves. . . . .	89
12.8	Wave flume configuration with a submerged cavity. . . . .	90
12.9	Configuration of laser module. . . . .	91
12.10	Laser sheet projected over submerged trench. . . . .	91
12.11	Configuration of fluorescent dye injection system. . . . .	92
12.12	Gravity driven injection apparatus. . . . .	92
12.13	Submerged cavity filled with fluorescent dye solution. . . . .	93
13.1	Free surface profiles downstream of screens, $\Phi = 40.31\%$ (left) and $\Phi = 22.67\%$ (right). . . . .	95
13.2	Relationships of head loss v.s. square of upstream averaged flow velocity, $V_1^2$ . . . . .	96
13.3	Effect of screen pore size on head loss for porosities of 40.31% and 29.61%. . . . .	97
13.4	Effect of screen pore size on head loss for porosities of 22.67% and 16.08%. . . . .	98
13.5	Effect of angle of inclination on head loss for pore diameter of 1/4". . . . .	99
13.6	Effect of angle of inclination on head loss for pore diameter of 1/8". . . . .	100
13.7	Relationships of head loss v.s. square of averaged pore velocity, $V_p^2$ , for pore diameters of 1/4" and 1/8". . . . .	101
13.8	Theoretical relationships of energy coefficients v.s. porous effect parameter. . . . .	103
13.9	Theoretical relationship of $C_T$ v.s. $k_0h$ . . . . .	104
13.10	Comparisons of theoretical and experimental $C_T$ values v.s. $G_0$ calculated with calibrated $b$ values under incident wave conditions 3 and 4. . . . .	106
13.11	Transmitted wave profiles from screens of 0.25" pore diameter and porosities of 40.31%, 29.61%, 22.67%, and 16.08% (from top to bottom) under incident wave condition 3. . . . .	108
13.12	Transmitted wave profiles from screens of 0.125" pore diameter and porosities of 40.31%, 29.61%, 22.67%, and 16.08% (from top to bottom) under incident wave condition 3. . . . .	109
13.13	Transmitted wave profiles from screens of 0.25" pore diameter and porosities of 40.31%, 29.61%, 22.67%, and 16.08% (from top to bottom) under incident wave condition 4. . . . .	110

13.14	Transmitted wave profiles from screens of 0.125" pore diameter and porosities of 40.31%, 29.61%, 22.67%, and 16.08% (from top to bottom) under incident wave condition 4. . . . .	111
13.15	Images extracted from a recorded video showing time evolution of flow field and induced vortices for a solitary wave of $\alpha = 0.27$ propagating past a trench with $D = 1$ and $W = 1$ . . . . .	113
13.16	Images extracted from a recorded video showing time evolution of flow field and induced vortices for a solitary wave of $\alpha = 0.27$ propagating past a trench with $D = 1$ and $W = 1.9$ . . . . .	114
13.17	Trajectories of a free surface particle for a solitary wave propagating in a domain of uniform depth. Black line denotes the observed data from Longuet-Higgins (1981) and white circle symbols represent the result from the 2-D viscous flow model by Chang, Chu, Wang, and Tang (2011). . . . .	117
13.18	Variations of maximum transported distance $S_{max}$ versus dimensionless wave height $\alpha$ for fluid particles initially positioned at the free surface and bottom. Dashed line: KdV first order theory; Hollow circle: Fenton's (1972) ninth-order analytical solution; Solid circle: experimental data from Longuet-Higgins (1981); Dotted line: 2-D inviscid model; Solid line: 2-D viscous model. . . . .	118
13.19	Fluorescent dye filled submerged cavity. . . . .	119
13.20	Variations of $S_{max}$ versus $\alpha$ for cases in combinations of $W = 0.5, 1.0, 2.0$ and $D = 0.5, 1.0$ and experimentally estimated data from limited cases. . .	120
13.21	Time variations of particle removal percentage from a trench by solitary waves of various wave heights. . . . .	121

## List of Tables

3.1	Elevation distribution of study area. . . . .	10
3.2	Slope distribution of study area. . . . .	10
4.1	Rain gauge station attributes. . . . .	13
4.2	Properties of typhoon events. . . . .	16
7.1	RMSE comparisons between RK, merging, and OK techniques for Typhoon Kalmaegi. . . . .	32
7.2	CE comparisons between RK, merging, and OK techniques for Typhoon Kalmaegi. . . . .	33
7.3	RMSE comparisons between RK, merging, and OK techniques for Typhoon Morakot. . . . .	38
7.4	CE comparisons between RK, merging, and OK techniques for Typhoon Morakot. . . . .	39
7.5	Summaries of error analysis between RK, merging, and OK techniques for Typhoons Fungwong, Sinlaku, and Fanapi. . . . .	45
7.6	Significance of auxiliary predictors. . . . .	46
7.7	RMSE comparisons between RK, merging, and OK techniques for Typhoon Fungwong. . . . .	47
7.8	CE comparisons between RK, merging, and OK techniques for Typhoon Fungwong. . . . .	48
7.9	RMSE comparisons between RK, merging, and OK techniques for Typhoon Sinlaku. . . . .	49
7.10	CE comparisons between RK, merging, and OK techniques for Typhoon Sinlaku. . . . .	50
7.11	RMSE comparisons between RK, merging, and OK techniques for Typhoon Fanapi. . . . .	51
7.12	CE comparisons between RK, merging, and OK techniques for Typhoon Fanapi. . . . .	52
12.1	Screen specifications. . . . .	84
12.2	Incident waves generated for wave transformation by porous screen tests. . . . .	88
13.1	Incident wave conditions generated for determination and verification of $b$ values. . . . .	104
13.2	Calibrated $b$ values of porous screens tested. . . . .	105
13.3	Values of $G_0$ and corresponding $C_T$ for porous screens tested under incident wave conditions 3 and 4. . . . .	105
13.4	Wave reduction percentage comparisons. . . . .	107

## Nomenclature

$A_1$	Upstream flow area
$A_2$	Downstream flow area
$A_{out}$	Total amount of transported fluid particle
$A_p$	Total opening area of porous screen
$a$	Coefficient for $Z - R$ relationship
$a$	Wave amplitude
$b$	Exponent for $Z - R$ relationship
$b$	Material constant of porous barrier
$C$	Center to center distance between two pores of porous screen
$C_R$	Coefficient of reflection
$C_T$	Coefficient of transmission
$CE(\mathbf{x}_i)$	Coefficient of efficiency at $\mathbf{x}_i$
$D$	Dimensionless depth of submerged cavity
$D$	Pore diameter of porous screen
$D^*$	Depth of submerged cavity
$E(\mathbf{x}_i)$	Elevation at $\mathbf{x}_i$
$E(\mathbf{x}_p)$	Elevation at $\mathbf{x}_p$
$F$	Function representing free surface
$f$	Oscillating frequency of wave maker

$G_0$	Porous effect parameter
$g$	Gravitational constant
$g_k(\mathbf{x}_i)$	Value of auxiliary variable at $\mathbf{x}_i$
$H$	Wave height
$h$	Gauge separation distance
$h$	Undisturbed water depth
$I_0$	Coefficient pertaining to incident wave
$k_0$	Wave number of progressive wave mode
$k_n$	Wave number of evanescent wave mode
$m$	Effective wave number
$n(h)$	Total number of paired data with separation distance of $h$
$Q$	Flow rate
$R$	Rainfall rate
$R(\mathbf{x}_i)$	Radar rainfall at $\mathbf{x}_i$
$R(\mathbf{x}_p)$	Radar rainfall at $\mathbf{x}_p$
$\hat{R}(\mathbf{x}_p)$	Interpolated rainfall at $\mathbf{x}_p$
$R_0$	Coefficient pertaining to reflected wave
$R_e$	Reynolds number
$R_g(\mathbf{x}_i)$	Rainfall observation at $\mathbf{x}_i$
$\overline{R}_g(\mathbf{x}_i)$	Average of rainfall measurement at $\mathbf{x}_i$
$R_{gt}(\mathbf{x}_i)$	Gauge measurement at $\mathbf{x}_i$ and time $t$

$\hat{R}_{ini}(\mathbf{x}_p)$	Initial rainfall at $\mathbf{x}_p$
$R_n$	Coefficient pertaining to evanescent wave upstream of porous barrier
$\hat{R}_t(\mathbf{x}_i)$	Interpolated rainfall at $\mathbf{x}_i$ and time $t$
$RMSE(\mathbf{x}_i)$	Root-mean-square error at $\mathbf{x}_i$
$S$	Stroke length of wave maker
$S_{max}$	Dimensionless maximum transporting distance of fluid particle
$S_{max}^*$	Maximum transporting distance of fluid particle
$T$	Dimensionless time
$T_0$	Coefficient pertaining to transmitted wave
$T_n$	Coefficient pertaining to evanescent wave downstream of porous barrier
$t$	Time
$u$	Velocity component in $x$ direction
$\mathbf{u}$	Velocity vector
$V_1$	Upstream averaged flow velocity
$V_2$	Downstream averaged flow velocity
$V_{normal}$	Velocity component normal to porous screen
$V_p$	Averaged pore velocity
$W$	Dimensionless width of submerged cavity
$W^*$	Width of submerged cavity
$w$	Velocity component in $z$ direction
$\mathbf{x}_i$	Position vector of $i$ th gauge station

$\mathbf{x}_p$	Position vector of ungauged location
$Y_1$	Upstream uniform depth
$Y_2$	Downstream uniform depth
$Z$	Radar reflectivity
$Z$	Undisturbed original vertical position of fluid particle
$Z_1$	Upstream elevation of flume bottom
$Z_2$	Downstream elevation of flume bottom
$\alpha$	Dimensionless solitary wave height
$\beta$	First approximation of wave expansion coefficient
$\beta_0$	Intercept of regression line
$\beta_k$	Regression coefficient
$\gamma(h)$	Semivariance for gauge separation distance of $h$
$\Delta h$	Head loss induced by porous screen
$\Delta R_r(\mathbf{x}_p)$	Rainfall adjustment at $\mathbf{x}_p$
$\varepsilon$	Dimensionless sinusoidal wave height
$\varepsilon(\mathbf{x}_i)$	Residual at $\mathbf{x}_i$
$\varepsilon(\mathbf{x}_i + h)$	Residual at neighboring station with separation distance of $h$
$\hat{\varepsilon}(\mathbf{x}_p)$	Residual at $\mathbf{x}_p$
$\eta$	Free surface elevation
$\bar{\eta}$	Averaged vertical displacement of fluid particle
$\eta_0$	Wave elevation of incident wave

$\eta_1$	Wave elevation upstream of porous barrier
$\eta_2$	Wave elevation downstream of porous barrier
$\theta$	Angle of inclination of porous screen
$\lambda$	Wave length of incident wave
$\mu$	Dynamic viscosity of fluid
$\mu$	Lagrange multiplier
$\nu$	Kinematic viscosity of fluid
$\bar{\xi}$	Averaged horizontal displacement of fluid particle
$\bar{\xi}_{max}$	Averaged maximum horizontal displacement of fluid particle
$\rho$	Density of fluid
$\Phi$	Porosity of porous screen
$\phi$	Velocity potential
$\phi_1$	Velocity potential upstream of porous barrier
$\phi_2$	Velocity potential downstream of porous barrier
$\phi_{E1}$	Velocity potential of evanescent wave upstream of porous barrier
$\phi_{E2}$	Velocity potential of evanescent wave downstream of porous barrier
$\phi_I$	Velocity potential of incident wave
$\phi_R$	Velocity potential of reflected wave
$\phi_T$	Velocity potential of transmitted wave
$\psi$	Stream function
$\omega$	Angular frequency of incident wave

$\omega$	Vorticity
$\omega_{ip}$	Kriging weight determined at $\mathbf{x}_i$ with respect to $\mathbf{x}_p$
$\%_{red}$	Reduction percentage of incident wave height
$\nabla^2$	Laplace operator

# Part I

## GEOSTATISTICAL INTERPOLATION OF RAIN FIELDS USING RADAR ESTIMATES AND GAUGE OBSERVATIONS: ALGORITHM DESIGN AND AUTOMATION

# Chapter 1

## Introduction

Global climate changes over the past few decades have altered the weather patterns around the world. The increasing occurrence and intensity of extreme events has been observed. The 2003 European heat wave, for instance, resulted in one of the hottest summers on record in Europe. In 2004, an unusually high number of typhoons passed through East Asia. Severe property damage and loss of lives were unavoidable in many countries within the region as the result of devastating landslides, debris flows, and floods that were induced by the tremendous amount of rain brought by the typhoons. On a larger scale, a country's economy could be affected due to the impact suffered by the agricultural, tourism and other industries. Evidences have shown that the increasing frequency and intensity of typhoons in East Asia is due to the westward shifting of two prevailing typhoon tracks in the western North Pacific (Wu, Wang, & Geng, 2005).

On average, four typhoons with the intensity of moderate or higher strike Taiwan every year. Typhoon Morakot in August 2009 was responsible for a death toll at over 650 and damages estimated at \$3.3 billion dollars. The entire village of Xiaolin was buried in mudslide during the event. More than 500 people were reportedly killed, and many still remain missing. Figure 1.1 shows roads that were destroyed by Typhoon Morakot. With roads destroyed, transportation between towns in the mountains was impossible, which made sending medical supplies and food to the impacted areas as well as carrying out rescue missions extremely challenging.

Implementation of early warning systems in watershed management and rain-induced disaster mitigation has been proven to be essential in terms of monitoring covered areas and providing vital hydrologic information, such as rainfall amount and water surface level in riverine systems, for early action planning during an event. Successful examples of implementation of flood warning systems include the FAS 1 and FAS 2 systems at the Texas



**Figure 1.1:** Road damage in Taiwan, caused by Typhoon Morakot in August 2009.

Medical Center in Houston, Texas (Fang, Bedient, Benavides, & Zimmer, 2008). The systems utilize gridded rainfall data extracted from the weather radar as inputs for hydrologic response modeling of storm events. The runoff prediction accuracy and sensitivity of a distributed hydrologic model were evaluated for reservoir operations and water resources management at the Yongdam and Namgang basins of Korea (Vieux, Park, & Kang, 2009). With accurate runoff information not only can reservoir release be better regulated during the wet seasons, but the volume of water to be preserved for the dry seasons can be estimated more accurately.

Physically based warning systems are typically integrations of geographic information systems (GIS), hydrologic and hydraulic models with additional system configurations for real-time operations. The input data for hydrologic and hydraulic models consist of various hydro-meteorological and geophysical variables. Among all model inputs, rainfall data undoubtedly have the most critical influence on modeling results. Since precipitation is such a highly dynamic and intermittent process, high resolution space-time data are often required to achieve satisfactory modeling outcomes. Rainfall data are traditionally recorded at the selected gauge stations in a targeted area. The observations only represent the time variation of an event at the points where they were recorded. In order to represent the spatial rainfall distribution (rain field) at a specific time during an event, interpolation methods ranging from simple approaches such as Thiessen polygon (Thiessen & Alter, 1911) and inverse distance weighted (IDW) to a more advanced and geostatistically based kriging (Krige, 1951) method are required to obtain rainfall information at the ungauged locations.

However, the results of interpolation are heavily dependent on rain gauge network density (Duncan, Austin, Fabry, & Austin, 1993). Inadequate sampling can significantly affect the interpolated values and leads to unrealistic representation of rain fields.

With the recent technology advancement in distributed (or gridded) hydrologic modeling and meteorological observation, especially, the use of high resolution space-time rainfall estimates from the weather radar as model inputs (Cole & Moore, 2009), considerable improvement of the accuracy of streamflow prediction has been demonstrated in numerous studies (e.g., Cole & Moore, 2009; Fang et al., 2008; Vieux et al., 2009; Wang & Xu, 2011). Although radar estimates preserve the spatial and temporal characteristics of an event, the uncertainties and system errors existing in the estimated rainfall values still remain an issue. Since gauge observations are widely accepted as ground truth, techniques to combine the spatial details of radar estimates and accuracy of gauge measurements to construct reliable rain fields have been proposed and validated by many researchers (Krajewski, 1987; Krämer & Verworn, 2009; Orasi, Lasinio, & Ferrari, 2009; Severino & Alpuim, 2005).

This study was to develop an automated rain field generation algorithm using combined radar and gauge rainfall for the Chenyulan River watershed in Taiwan. The watershed is highly susceptible to flash flooding during the typhoon season. The early warning system that is currently in operation for flood forecasting relies solely on its rain gauge network as the rainfall data source for hydrologic and hydraulic simulations. The ultimate goals of this study would be to integrate the developed algorithm into the system and enhance the accuracy of rainfall input with the much detailed high resolution space-time rainfall data. The expected simulation results should provide the emergency response agencies with confidence in early action planning to reduce chance of catastrophes. The algorithm was based on the regression-kriging (RK) spatial interpolation method and written in R (R Core Team, 2013) statistical programming language. The performance of the method was evaluated on five historical typhoon events (Kalmaegi, Fungwong, Sinlaku, Morakot, and Fanapi). The interpolated results along with the results obtained using the ordinary kriging (OK) and merging methods were compared against the observed rainfall values at the gauge locations. Finally, the completed algorithm was configured to be executed at a preset time interval in batch mode for automated operation.

## Chapter 2

### Literature Review

Hydrologic predictions in terms of surface runoff are critically important to disaster mitigation as well as water resources planning and management. Tremendous efforts have been dedicated to the development of numerical models by researchers over the years in attempts to accurately simulate the hydrologic responses of targeted areas during severe weather events. With the increase of computational power and availability of high resolution spatial and temporal data, physically based distributed models have rapidly gained popularity over empirically based lumped models. Complex governing equations can now be solved using advanced numerical methods without compromising computational efficiency. Meanwhile, an increase in streamflow prediction accuracy can be achieved with the inclusion of the detailed geophysical and meteorological characteristics of areas of interest. The performances of distributed and lumped models have been assessed (e.g., Cole & Moore, 2009; Khakbaz, Imam, Hsu, & Sorooshian, 2012; Paudel, Nelson, Downer, & Hotchkiss, 2011). The studies of implementation of distributed model for a variety of hydrologic applications can be found in Jorgeson and Julien (2005), Sharif, Yates, Roberts, and Mueller (2006), Vischel, Pegram, Sinclair, Wagner, and Bartsch (2008), Dutta and Nakayama (2009), Sharif, Hassan, Bin-Shafique, Xie, and Zeitler (2010), Chu, Lin, Huang, Hsu, and Chen (2010), Looper, Vieux, and Moreno (2012), and others.

Among all required inputs for runoff modeling, rainfall data undoubtedly have the most critical influence on prediction results. In order to fulfill the requirement of high resolution input data for distributed simulations, dense gauge networks must be built to observe the actual spatial distribution of rainfall. However, establishing dense gauge networks, especially in mountainous regions, is impractical due to the high cost of instrumentation and required routine maintenance services (Andrieu, Creutin, Delrieu, & Faure, 1997; Krajewski, 1987). In addition, geographical constraints such as highly sloped terrain also limit

the number and placement of gauges within a network. Rainfall values over the ungauged regions are generally estimated through spatial interpolation. As indicated by Duncan et al. (1993), the interpolated results were heavily dependent on rain gauge network density. Regardless which interpolation technique is chosen, the technique can easily miss the representation of the occurred overall rainfall distribution due to under-sampling if the number of stations is insufficient. Sampling errors produced from rain gauge networks with various densities were investigated by Huff (1970), Silverman, Rogers, and Dahl (1981), Duncan et al. (1993), and Russo, Napolitano, and Gorgucci (2005).

With the recent advancement in observation technology, remote sensing has become an invaluable alternative to field sample collection because of its ability to economically acquire the detailed spatial distribution of target variables over large areas in a timely fashion. Weather radar is one of such systems that provides multiple types of meteorological products (e.g., precipitation, hail index, wind profile) (Dolciné, Andrieu, & French, 1997). These products are typically derived from the reflectivity measurements and stored in gridded formats and short intervals in time, which are particularly useful for real time disaster warning operations. Radar precipitation has had a long history of being used in flood forecasting and other types of hydrologic predictions (Andrieu et al., 1997; Borga, 2002; Creutin, Andrieu, & Faure, 1997; Fulton, Breidenbach, Seo, Miller, & O'Bannon, 1998; Hossain, Anagnostou, Dinku, & Borga, 2004; Stelman, Fuelberg, Garza, & Mullusky, 2001). While the precipitation estimates provide the spatial and temporal details of a rainfall event, it is well known that the data are subject to uncertainties and systematic errors (Andrieu et al., 1997; Austin, 1987; Berne & Krajewski, 2013; Creutin et al., 1997; Doviak, 1983; Mandapaka, Villarini, Seo, & Krajewski, 2010; Wilson & Brandes, 1979). Hence, proper adjustments are required prior to their use as inputs for any simulation tasks. As pointed out by Wilson and Brandes (1979) and others, the main source of error of radar rainfall occurred during the conversion process. The precipitation estimates are converted from the reflectivity measurements using the  $Z - R$  relationship (i.e., Equation (4.1)) under the assumptions that the rain drop distribution is exponential, and the vertical air flow is relatively small comparing to the terminal velocities of rain drops. In reality, the drop size distribution and air motion will most likely not be as assumed and vary continuously

throughout an event. It would not be feasible to adjust the coefficients of the  $Z - R$  relationship for every event.

As rainfall recorded by rain gauges is commonly considered as ground truth, a great number of methodologies that combine both gauge observations and radar estimates to generate rain fields have been proposed. By utilizing data from both sources, the accuracy of point measurement and high resolution spatial information can be integrated to accurately reflect the actual rainfall distribution over targeted areas. Many researchers and governmental agencies have adopted the mean field bias correction method as a quick and simple way to calibrate radar rainfall in real time operations (Borga, 2002; Fulton et al., 1998; Steiner, Smith, Burges, Alonso, & Darden, 1999; Vieux et al., 2009; Wilson & Brandes, 1979; Zhang & Srinivasan, 2010). The ratios of gauge to radar values at the locations of all gauges in a network are averaged, and the averaged correction factor is then multiplied uniformly to the entire radar field. Cole and Moore (2009) tested an integrated multi-quadratic estimation technique for the dynamic generation of gridded gauge-adjusted rain fields. Geostatistically based approaches in recent years have become increasingly preferred for the interpolation of rainfall. Kriging is one of such approaches that has been considered the best linear unbiased estimator (Christensen, 1990). Some commonly seen forms of kriging that have shown excellent rainfall prediction results using both gauge precipitation and radar estimates or other secondary variables include simple kriging with varying local means (SKlm) (Goovaerts, 1997), kriging with external drift (KED), regression-kriging (RK) (Odeh, McBratney, & Chittleborough, 1994, 1995), universal kriging (UK) (Matheron, 1969), and co-kriging (CK). SKlm, KED, RK, and UK are very similar in terms of their mathematical formulations. The primary differences between these multivariate techniques are the steps that are taken to solve for the kriging weights (Hengl, Heuvelink, & Stein, 2003). Apart from the others, CK is a more complex and computationally demanding extension of kriging. Not only the correlation of each of the primary and secondary variables has to be analyzed, the cross correlation between the residuals of the variables must also be examined. The various forms of multivariate kriging for rainfall interpolation in distributed hydrologic modeling have been assessed. Goovaerts (2000) explored the use of digital elevation model (DEM) as an external predictor for spatial rainfall prediction. The results

showed that SKlm, KED, and CK outperformed the conventional Thiessen polygon, IDW, OK, and linear regression. Haberlandt (2007) included both radar estimates and elevation values as external predictors for rain field interpolation. The results also confirmed that multivariate methods clearly outperformed univariate techniques. Schuurmans, Bierkens, Pebesma, and Uijlenhoet (2007) studied the effect of the extent of interpolation domain on spatial rainfall prediction accuracy. The performances of KED and CK using radar precipitation as a secondary predictor were compared against OK. Zhang and Srinivasan (2010) developed a radar rainfall correction toolbox for ArcGIS. The selected adjustment algorithms were SKlm, RK, and mean field bias correction. Both RK and SKlm outperformed mean field bias correction. Other tested case studies can also be found in Severino and Alpuim (2005), Orasi et al. (2009), and Biggs and Atkinson (2011).

Based on the conclusions from the above mentioned literature, multivariate kriging techniques will yield more accurate rain fields than the gauge only methods. This study decided to adopt RK as the primary rainfall interpolation technique due to its robustness, flexibility, and computational efficiency.

## Chapter 3

### Study Area

The Chenyulan River watershed is located in central Taiwan. It is elongated in the north-south direction and encompasses approximately 450 km<sup>2</sup> of land. The area rises to over 3700 meters near Mount Yu and descends northward to an elevation of 400 meters at its outlet. With the central ridge of the island of Taiwan to the east, the averaged elevation in the eastern and southeastern regions of the watershed is above 2500 meters. The location and elevation distribution of the watershed are shown in Figure 3.1 and Table 3.1.

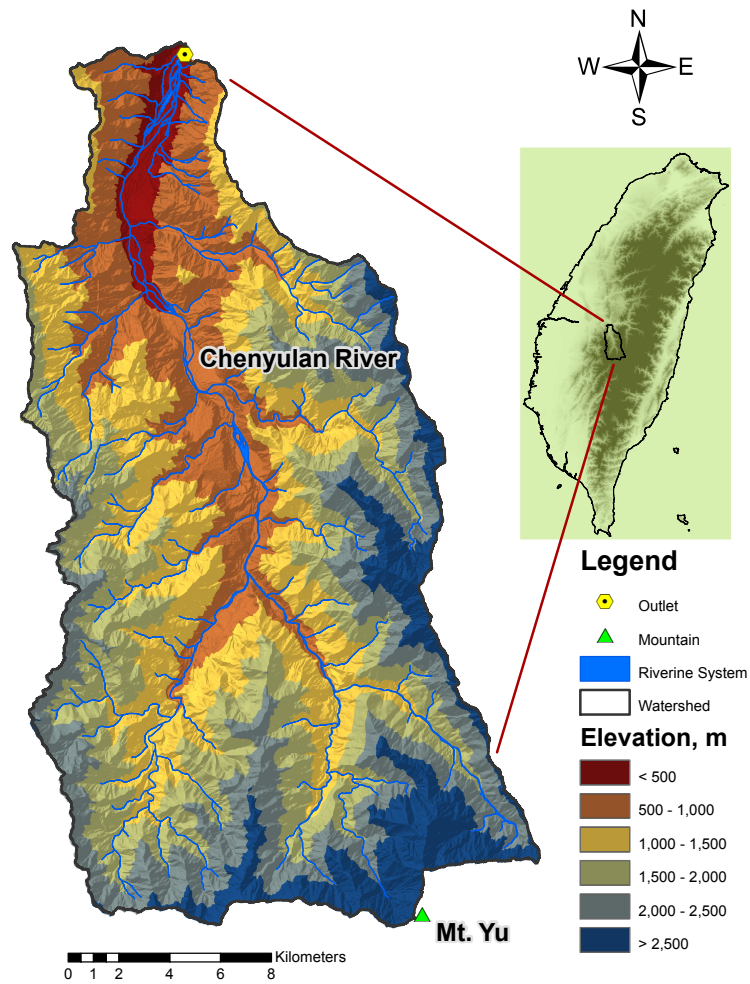


**Figure 3.1:** Location and elevation distribution of study area.

**Table 3.1:** Elevation distribution of study area.

Elevation, m	Area, km <sup>2</sup>	Percentage, %
< 500	14.6	3.3
500 - 1,000	89.0	19.9
1,000 - 1,500	111.4	24.8
1,500 - 2,000	105.6	23.6
2,000 - 2,500	80.8	18.0
> 2,500	46.4	10.4
Total	447.8	100

The watershed consists mostly of mountainous terrain. The slope of the majority of the land surface ranges from 20 to 60 degrees. The slope distribution is shown in Table 3.2 and Figure 3.2. The main river, the Chenyulan River, originates from the north ridge of Mount Yu and flows an estimated distance of 42.4 kilometers through a deeply cut valley. Due to a significant elevation drop of more than 2000 meters between the north and south ends of the watershed, the averaged channel bottom slope of the Chenyulan River is nearly 6.75 percent. The overall riverine system is depicted in Figure 3.1. The combination of highly sloped river channels and steep terrain accelerates the rainfall-runoff transformation, which makes the watershed highly susceptible to flash flooding. It should be noticed from Table 3.2 that approximately 15% of the watershed has a slope less than 20 degrees. These flatter areas are generally near the bottom of the river valley and are where most of the human activities take place (e.g., residential, agricultural, and other types). However, more often than not these areas are also located in the floodplains such that time for emergency response during severe weather events is greatly limited.

**Table 3.2:** Slope distribution of study area.

Slope, deg.	Area, km <sup>2</sup>	Percentage, %
0 - 20	65.8	14.7
20 - 40	211.9	47.3
40 - 60	162.5	36.3
60 - 90	7.6	1.7
Total	447.8	100

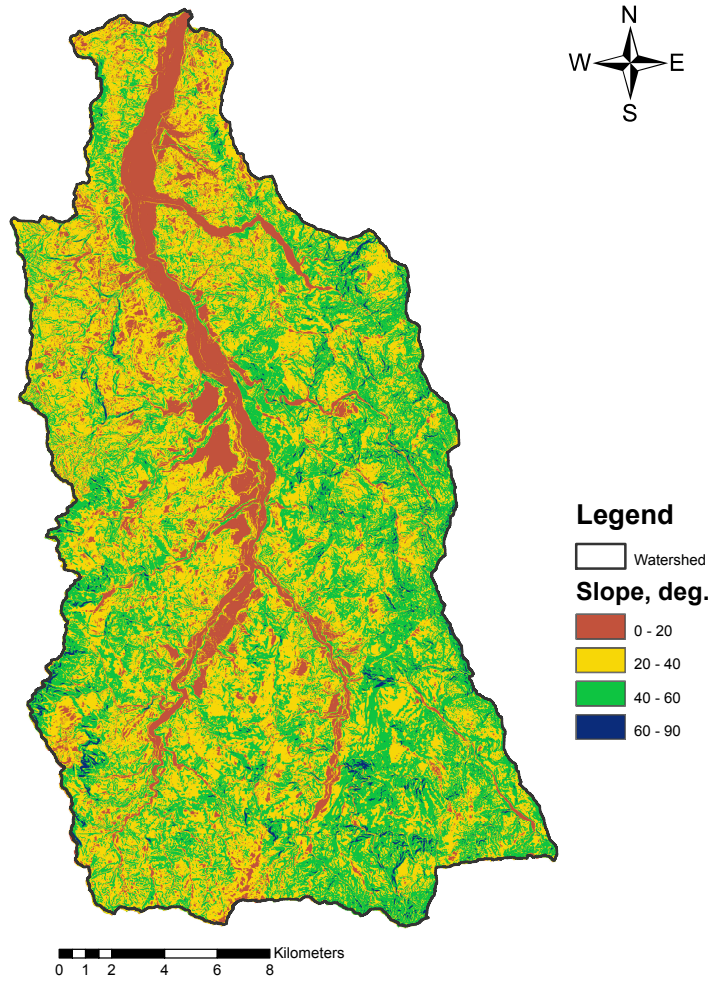


**Figure 3.2:** Slope distribution of study area.

## Chapter 4

### Rainfall Data

This study incorporated gauge observations and radar estimates to perform rain field interpolation. The details about the two types of rainfall data will be presented in the following sections. In addition, the five historical typhoon events that were selected to test the interpolation algorithm will also be introduced.

#### 4.1 RAIN GAUGE OBSERVATIONS

The importance of adequate rainfall sampling for rain field interpolation during storm events can never be overemphasized. As aforementioned, accurate rainfall data can enhance modeling results. In order to achieve adequate sample collection, sufficient and evenly distributed sampling locations are generally required. However, various geographical constraints often dictate the number and location of sampling sites when designing a rain gauge network.

The rain gauge network used for this study consists of 27 strategically selected stations, among which 23 are managed by the Central Weather Bureau (CWB) of Taiwan. The remaining four stations are operated by the Water Resources Agency (WRA). The gauge network is shown in Figure 4.1, and the corresponding elevation of each gauge is summarized in Table 4.1. Restricting by the rough terrain, most of the rain gauges in the study area were placed along river channels where easier access to the sites could be gained. In high elevation regions such as the east part of the watershed, establishing gauging stations was almost impossible. Therefore, under-sampling in certain areas could be expected.

In regard to rainfall recorded at each gauge station, the CWB preprocesses and cumulates the measured rain amount over regular time intervals (10 minute and 1 hour). The regular time series of rainfall could be used directly by the rain field interpolation algorithm developed in this study. The gauge observations of the WRA, however, are irregular and

could contain missing values. Extra efforts were required to fill in the missing data and convert the records into regular time series before entering the interpolation process.

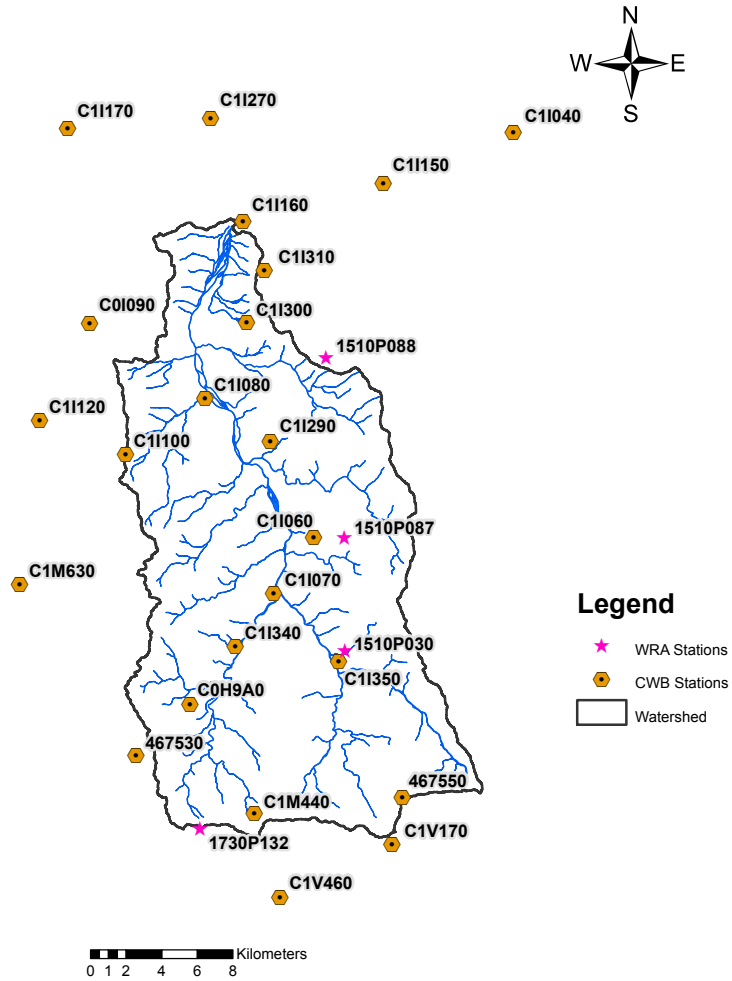


Figure 4.1: Rain gauge network covering study area.

Table 4.1: Rain gauge station attributes.

Station ID	Elevation, m	Station ID	Elevation, m	Station ID	Elevation, m
C1I270	593	C0H9A0	1,595	C1I080	536
C1I150	393	C1V460	1,949	C1I060	2,403
C1I160	399	C1M440	2,540	C1I070	825
C1I310	1,001	C1V170	3,690	467550	3,845
C1I300	781	C1M630	1,052	467530	2,413
C0I090	878	C1I170	235	1730P132	2,540
C1I100	1,771	C1I040	1,693	1510P088	1,666
C1I120	1,528	C1I350	887	1510P087	2,200
C1I290	1,151	C1I340	897	1510P030	1,135

## 4.2 RADAR RAINFALL ESTIMATES

The CWB, WRA, Soil and Water Conservation Bureau (SWCB) of Taiwan, and NOAA's National Severe Storms Laboratory (NSSL) had collaborated in the development of the Quantitative Precipitation Estimation and Segregation Using Multiple Sensors (QPESUMS) system. Since its deployment in 2002, the system has been used to produce a variety of weather products by integrating radar data with other meteorological observations such as wind speed, lightning strike, and rain gauge measurement. Among all products, past (1, 3, 6, 12, 24, and 72 hour) rainfall accumulation, 1 ~ 3 hour precipitation forecast, and future 24 hour typhoon center position and traveling path are particularly informative to the emergency response agencies and general public during typhoons as well as other storm events.

This study utilized the radar rainfall estimates extracted from the QPESUMS system as one of the auxiliary predictors for rain field interpolation. The rainfall values were derived from the radar base reflectivity measurements using the  $Z - R$  relationship,

$$Z = aR^b, \tag{4.1}$$

where  $Z$  is radar reflectivity in dBZ, and  $R$  is rainfall rate in mm/hr. The coefficient  $a$  and exponent  $b$  are dependent on factors such as geographical location, season, climate condition, and rainfall type and should be adjusted accordingly. For the purpose of convenience,  $a$  and  $b$  are generally held constant. The CWB had performed an extensive calibration and determined that 32.5 and 1.65 are the most suitable values of  $a$  and  $b$ , respectively, for Taiwan. Equation (4.1) becomes

$$Z = 32.5R^{1.65}. \tag{4.2}$$

The radar rainfall data, which cover the entire country of Taiwan, are recorded in ten minute intervals and stored in a gridded format with a bin dimension of 0.0125 degree  $\times$  0.0125 degree (latitude/longitude), i.e., approximately 1.25 km  $\times$  1.25 km. In order to reduce the file size and be computationally efficient during the preprocessing and interpolation stages, the coverage must be cropped to proper dimensions. Figure 4.2 shows a cropped

time slice of the radar rainfall of Typhoon Morakot. The detailed spatial distribution of rainfall at a selected instant is displayed.

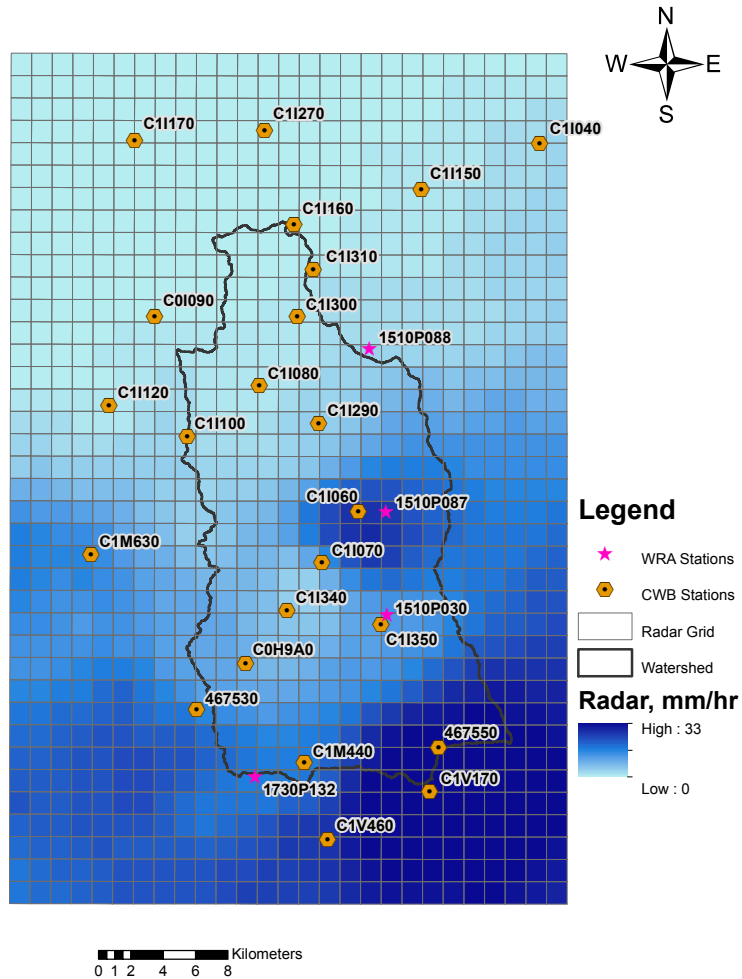


Figure 4.2: Sample time slice of radar rainfall, Typhoon Morakot in August 2009.

### 4.3 HISTORICAL TYPHOON EVENTS

Five historical typhoon events (Kalmaegi, Fungwong, Sinlaku, Morakot, and Fanapi) were selected to evaluate the performance of the rain field interpolation algorithm. The goal was to validate the applicability and reliability of the algorithm by testing it with events of different magnitudes. Table 4.2 summaries the properties of the selected typhoons. Even though the majority of them were classified as moderate, because of the different traveling paths and speed the amount of rainfall observed in the study area could vary

**Table 4.2:** Properties of typhoon events.

Name	Magnitude	Duration	Depth, mm
Kalmaegi	moderate	07/16/2008 - 07/18/2008	700
Fungwong	moderate	07/26/2008 - 07/29/2008	650
Sinlaku	high	09/11/2008 - 09/16/2008	1470
Morakot	moderate	08/05/2009 - 08/10/2009	3150
Fanapi	moderate	09/17/2010 - 09/20/2010	335

drastically. For instance, Typhoon Fanapi produced as little as 335 mm of rain at station 467530 (Figure 4.1). On the other hand, nearly 3150 mm of rain was recorded at the same station during Typhoon Morakot which caused one of the most devastating floods in recorded history. It was intended to demonstrate that the algorithm was capable of yielding reliable rain fields over a wide range of rainfall intensities. Figures 4.3 ~ 4.7, which were extracted from the CWB’s historical typhoon database ([http://rdc28.cwb.gov.tw/TDB/ntdb/pageControl/ty\\_warning](http://rdc28.cwb.gov.tw/TDB/ntdb/pageControl/ty_warning)), illustrate the traveling paths of the aforementioned typhoons. It can be seen that Typhoons Kalmaegi, Sinlaku, and Morakot moved through the northern part of Taiwan, while Typhoons Fungwong and Fanapi passed through respectively the middle and southern parts of Taiwan.

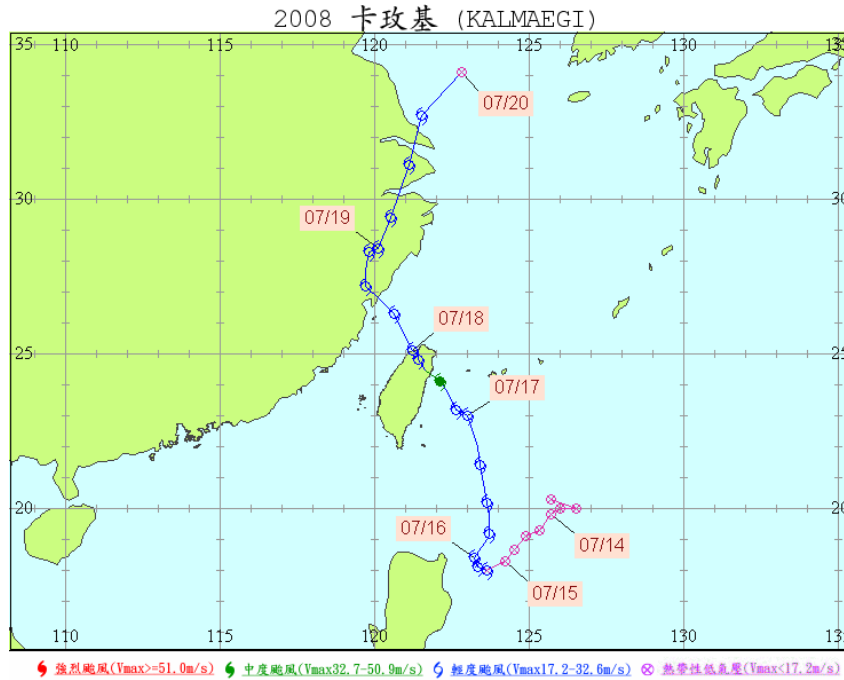


**Figure 4.3:** Track of Typhoon Kalmaegi, July 2008, photo courtesy of CWB.

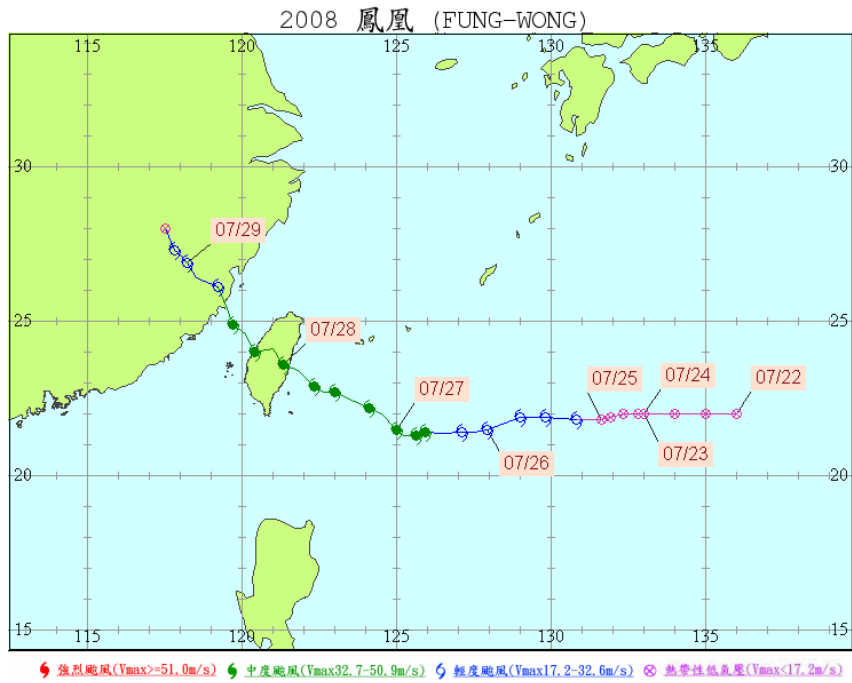


Figure 4.4: Track of Typhoon Fungwong, July 2008, photo courtesy of CWB.

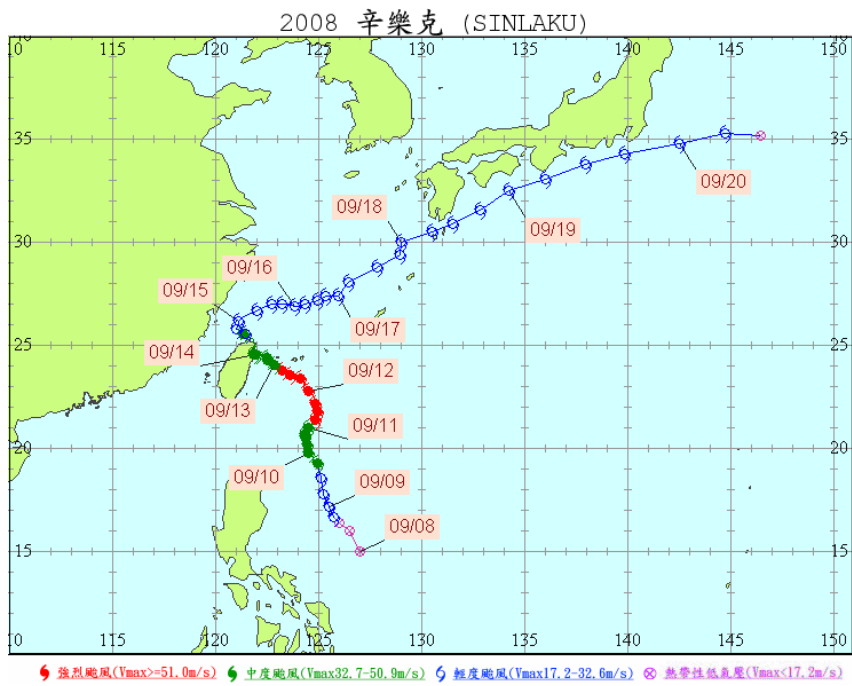


Figure 4.5: Track of Typhoon Sinlaku, September 2008, photo courtesy of CWB.

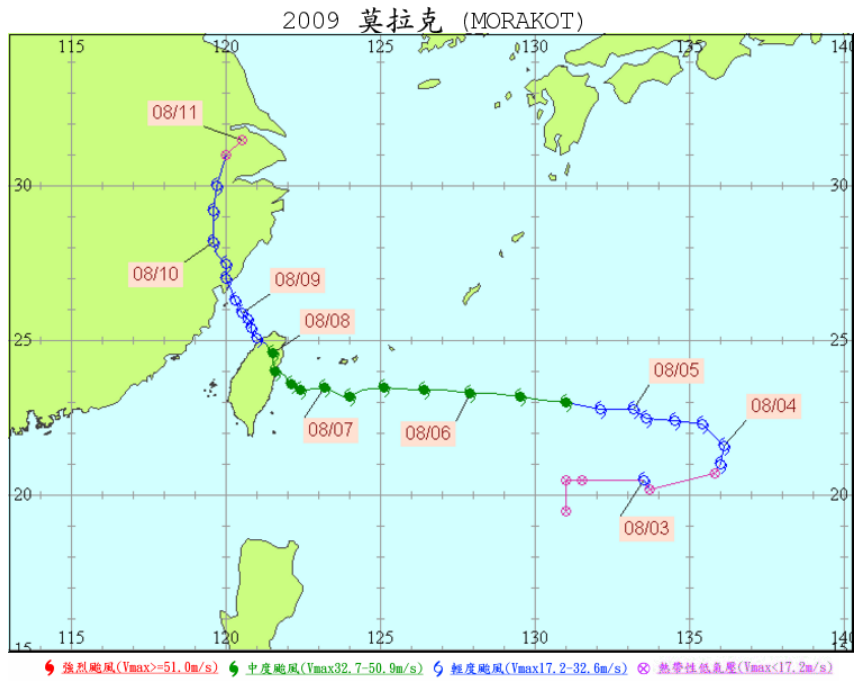


Figure 4.6: Track of Typhoon Morakot, August 2009, photo courtesy of CWB.

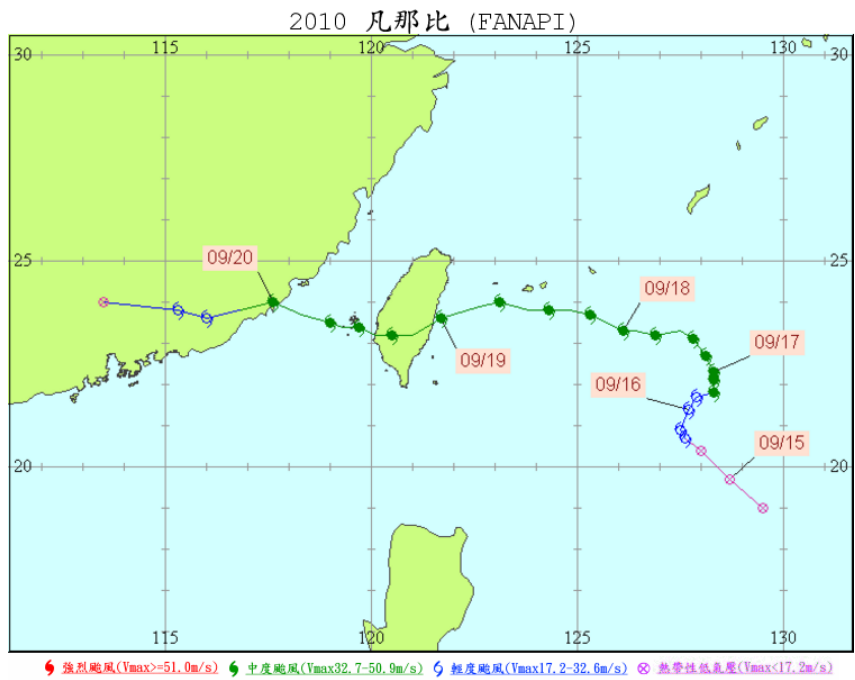


Figure 4.7: Track of Typhoon Fanapi, September 2010, photo courtesy of CWB.

## Chapter 5

### Rain Field Interpolation

It has been shown in numerous studies that geostatistically based multivariate interpolation techniques can produce rain fields with higher accuracy than univariate and other conventional methods under inadequate sampling conditions. Among the various interpolation approaches, two multivariate kriging techniques, RK and merging, were selected for performance evaluation in this study. The theoretical background of the selected methods will be introduced in the subsequent sections.

#### 5.1 REGRESSION-KRIGING

The geostatistically based regression-kriging (RK) spatial interpolation technique, which has been recognized by its robustness and flexibility, was selected as the primary method to generate rain fields covering the Chenyulan River watershed. According to Matheron (1969), the spatial variation of a target variable can be presented as the summation of its deterministic (trend) and stochastic (disturbance or residual) components. In RK, the deterministic part of variation of a target variable is modelled by linear regression such that a linear relationship based on the correlation between the target and auxiliary variables is developed. The stochastic part of variation is estimated by kriging of the regression residuals. For this study, the target variable was rainfall rate from the gauge stations, and the auxiliary variables were the radar rainfall estimates from the QPESUMS system and elevation values pertaining to the watershed and its surrounding areas. As demonstrated by Goovaerts (2000) and Lloyd (2005), elevation can be successfully incorporated into spatial rainfall interpolation.

A multiple linear regression model can be expressed as

$$R_g(\mathbf{x}_i) = \beta_0 + \sum_{k=1}^m \beta_k g_k(\mathbf{x}_i) + \varepsilon(\mathbf{x}_i) \quad i = 1, 2, 3, \dots, n, \quad (5.1)$$

where  $\mathbf{x}_i = (x_i, y_i)$  represents the position vector of the  $i$ th gauge station,  $R_g(\mathbf{x}_i)$  are the gauge rainfall observations at  $\mathbf{x}_i$ ,  $\beta_k$  are the regression coefficients to be determined ( $\beta_0$  is the intercept),  $g_k(\mathbf{x}_i)$  are the values of auxiliary variables at  $\mathbf{x}_i$ ,  $\varepsilon(\mathbf{x}_i)$  are the residuals at  $\mathbf{x}_i$ ,  $n$  is the total number of gauge stations, and  $m$  is the total number of auxiliary variables. Assigning the radar data and elevation at  $\mathbf{x}_i$  as  $R(\mathbf{x}_i)$  and  $E(\mathbf{x}_i)$ , respectively, Equation (5.1) is expanded as

$$R_g(\mathbf{x}_i) = \beta_0 + \beta_1 R(\mathbf{x}_i) + \beta_2 E(\mathbf{x}_i) + \varepsilon(\mathbf{x}_i). \quad (5.2)$$

The regression coefficients  $\beta_0$ ,  $\beta_1$ , and  $\beta_2$  are determined by the method of ordinary least squares (OLS) or generalized least squares (GLS). The residuals  $\varepsilon(\mathbf{x}_i)$  can also be calculated. With the known regression coefficients, the trend of rainfall variation for a given instant at any ungauged location  $\mathbf{x}_p$  is obtained by  $\beta_0 + \beta_1 R(\mathbf{x}_p) + \beta_2 E(\mathbf{x}_p)$  using the corresponding radar and elevation data at  $\mathbf{x}_p$ , where  $\mathbf{x}_p = (x_p, y_p)$  represents the position vector of the ungauged location. Furthermore, a continuous trend surface can be generated with the trend values being interpolated at the centroid of each cell of the radar grid. Figure 5.1 shows an interpolated trend surface.

In addition to a trend surface, a residual surface is to be produced. The residual at any ungauged location  $\hat{\varepsilon}(\mathbf{x}_p)$  is estimated by the kriging technique. The estimated value is a linear combination of the residuals at neighboring gauge stations multiplied by the appropriate kriging weights and described as  $\hat{\varepsilon}(\mathbf{x}_p) = \sum_{i=1}^n \omega_{ip} \varepsilon(\mathbf{x}_i)$  where  $\omega_{ip}$  are the kriging weights determined at  $\mathbf{x}_i$  with respect to  $\mathbf{x}_p$ . Figure 5.2 shows an interpolated residual surface. The calculation of kriging weights involves several steps. First, a semivariance analysis must be performed. The semivariance between a pair of gauge stations separated by a distance of  $h$  is defined as

$$\gamma(h) = \frac{1}{2n(h)} \sum_{i=1}^{n(h)} (\varepsilon(\mathbf{x}_i) - \varepsilon(\mathbf{x}_i + h))^2, \quad (5.3)$$

where  $n(h)$  is the total number of paired data separated by  $h$ ,  $\varepsilon(\mathbf{x}_i)$  and  $\varepsilon(\mathbf{x}_i + h)$  are the residuals at  $\mathbf{x}_i$  and the neighboring stations at a distance of  $h$ , respectively. A semivariogram

can then be generated by plotting the calculated semivariances against distances (Hengl, 2009). By fitting a semivariogram model (spherical model in this study), semivariances for the entire spectrum of separation distance are obtainable. Figure 5.3 shows an example of a semivariogram. It should be noted that strong similarities exist between residuals at shorter distances as semivariance decreases as the distance between gauge stations decreases.

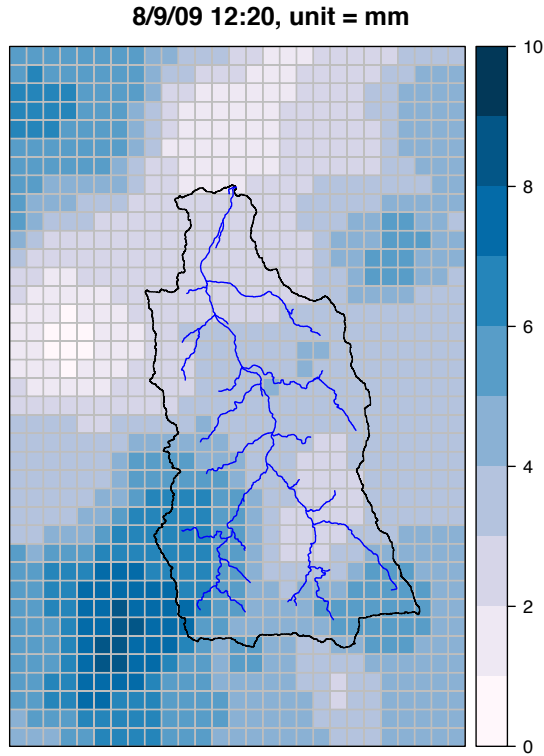


**Figure 5.1:** Sample trend surface of rainfall variation, Typhoon Morakot in August 2009.

With an established semivariogram, the kriging weights are determined by solving the following system of equations

$$\begin{bmatrix} \omega_{1p} \\ \omega_{2p} \\ \omega_{3p} \\ \vdots \\ \omega_{np} \\ \mu \end{bmatrix} = \begin{bmatrix} \gamma_{11} & \gamma_{12} & \dots & \gamma_{1n} & 1 \\ \gamma_{21} & \gamma_{22} & \dots & \gamma_{2n} & 1 \\ \gamma_{31} & \gamma_{32} & \dots & \gamma_{3n} & 1 \\ \vdots & \vdots & & \vdots & \vdots \\ \gamma_{n1} & \gamma_{n2} & \dots & \gamma_{nn} & 1 \\ 1 & 1 & 1 & 1 & 1 \end{bmatrix}^{-1} \begin{bmatrix} \gamma_{1p} \\ \gamma_{2p} \\ \gamma_{3p} \\ \vdots \\ \gamma_{np} \\ 1 \end{bmatrix}, \quad (5.4)$$

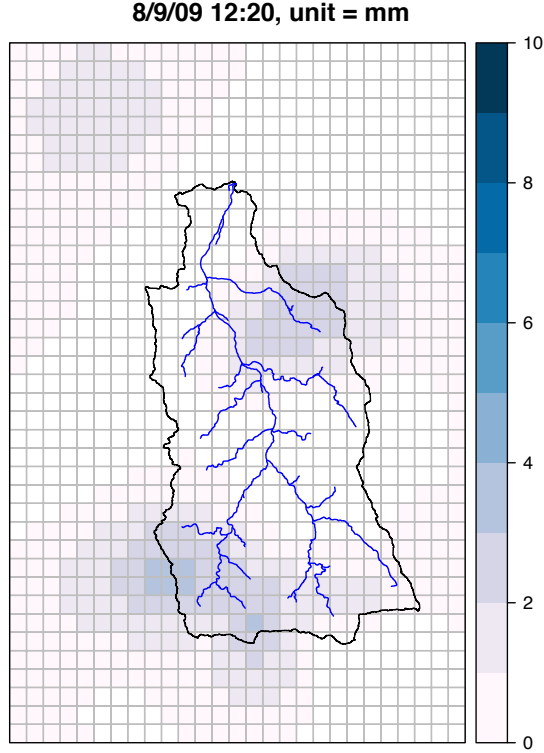


**Figure 5.2:** Sample residual surface of rainfall variation, Typhoon Morakot in August 2009.

where  $\gamma_{ij}$  are the semivariances of the corresponding paired gauge stations,  $\gamma_{ip}$  are the semivariances corresponded to the distances between  $\mathbf{x}_i$  and  $\mathbf{x}_p$ , and  $\mu$  is the Lagrange multiplier. Once the residual surface is produced, the summation of the trend and residual surfaces yields the final rain field. The complete spatial variation of rainfall rate at any ungauged location,  $\mathbf{x}_p$ , can be determined from

$$\hat{R}(\mathbf{x}_p) = \beta_0 + \beta_1 R(\mathbf{x}_p) + \beta_2 E(\mathbf{x}_p) + \sum_{i=1}^n \omega_{ip} \varepsilon(\mathbf{x}_i). \quad (5.5)$$

## 5.2 MERGING

The second technique considered for this study was the merging method (Ehret, 2003). The merging method also jointly uses radar estimates and gauge observations for rain field interpolation. However, the way the two types of data are utilized during the interpolation process is different from RK. The idea is to first estimate the rainfall values at ungauged

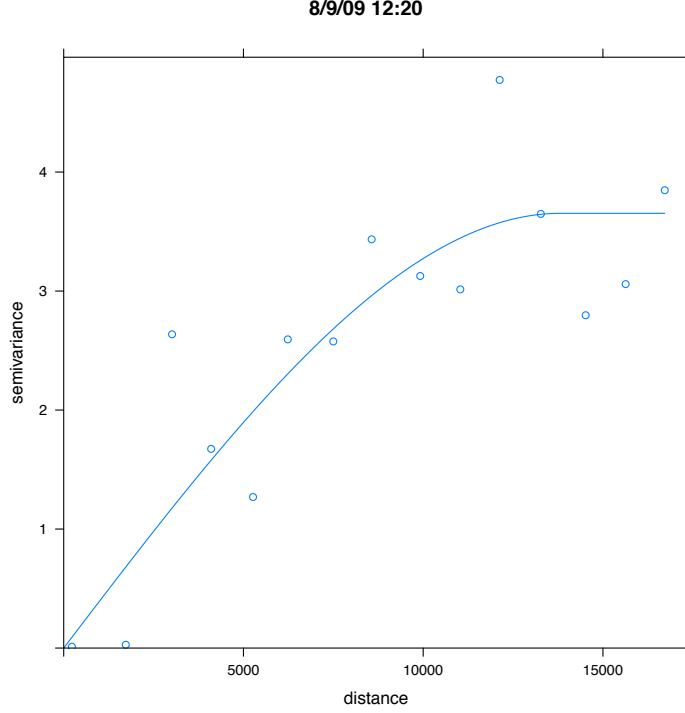


**Figure 5.3:** Sample semivariogram fitted with spherical model, Typhoon Morakot in August 2009.

locations based solely on gauge measurements. The adjustment values, which are derived from radar data that contain the trend of spatial variation of rainfall, then are merged to the initially estimated rainfall values to produce the final rain field.

Assuming that  $\hat{R}_{ini}(\mathbf{x}_p)$  represents the initial rainfall rate at any ungauged location  $\mathbf{x}_p$ , its value can be estimated by the ordinary kriging method and expressed as

$$\hat{R}_{ini}(\mathbf{x}_p) = \sum_{i=1}^n \omega_{ip} R_g(\mathbf{x}_i), \quad (5.6)$$

where  $\mathbf{x}_i$  represents the position vector of the  $i$ th gauge station,  $R_g(\mathbf{x}_i)$  are the gauge measurements at  $\mathbf{x}_i$ ,  $\omega_{ip}$  are the kriging weights determined at  $\mathbf{x}_i$  with respect to  $\mathbf{x}_p$ , and  $n$  is the total number of gauge stations. Equation (5.6) can be interpreted as that the initial rainfall rate at an ungauged location is a linear combination of the observed rainfall rates at neighboring stations multiplied by the assigned kriging weights. Similar to Equation (5.4), the kriging weights are determined by solving a system of equations. The elements of the matrix are obtained through semivariogram modeling. Semivariance is defined as in

Equation (5.3), except in this case gauge rainfall  $R_g(\mathbf{x}_i)$  is used instead of residuals  $\varepsilon(\mathbf{x}_i)$  as the variable being analyzed. With the initial rainfall values being interpolated at the centroids of the cells of the radar grid, a continuous rainfall distribution surface can be generated. Figure 5.4 shows an example of an initial rain field.

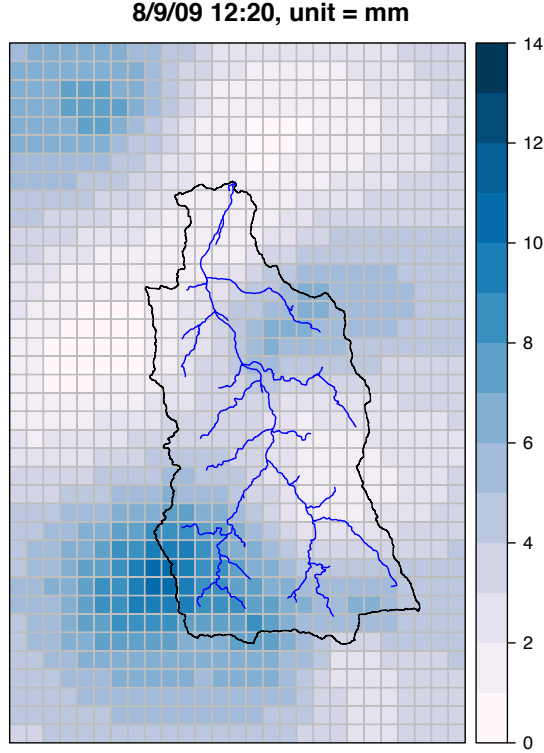


**Figure 5.4:** Sample gauge-based interpolated rainfall surface, Typhoon Morakot in August 2009.

The next step of the merging method is to determine the adjustment values to be added to the initially estimated rain field, given in Equation (5.6). The radar rainfall estimates from the grid cells that are coinciding with the rain gauge stations are extracted and used to produce a radar field by the ordinary kriging method. The adjustment values can then be calculated by subtracting the interpolated radar values from the original radar estimates and expressed as

$$\Delta R_r(\mathbf{x}_p) = R(\mathbf{x}_p) - \sum_{i=1}^n \omega_{ip} R(\mathbf{x}_i), \quad (5.7)$$

where  $\Delta R_r(\mathbf{x}_p)$  represents the adjustment value at any ungauged location  $\mathbf{x}_p$ ,  $R(\mathbf{x}_p)$  denotes the radar rainfall rate at location  $\mathbf{x}_p$ , and  $R(\mathbf{x}_i)$  are the extracted radar rainfall rates at gauge stations  $\mathbf{x}_i$ . Figure 5.5 shows a continuous surface of adjustment values. The final

rain field can be produced by incorporating the initial rainfall estimates and adjustment values as

$$\hat{R}(\mathbf{x}_p) = \hat{R}_{ini}(\mathbf{x}_p) + \Delta R_r(\mathbf{x}_p). \quad (5.8)$$

It should be noted that if the influence of radar adjustment is neglected, Equation (5.8) is reduced to the form of ordinary kriging (i.e., Equation (5.6)).

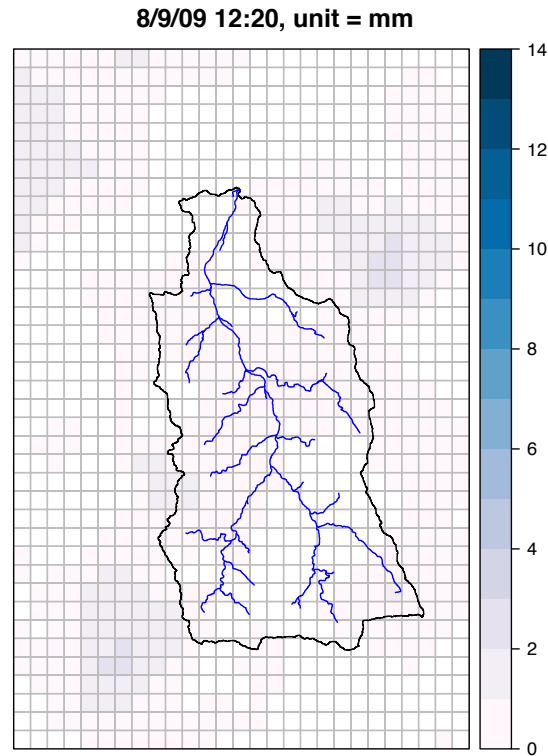


**Figure 5.5:** Sample interpolated surface of adjustment values, Typhoon Morakot in August 2009.

## Chapter 6

### Automation

In real-time flood forecasting operations, the entire processing sequence of a warning system from field data acquisition to final warning issue must be automated. One crucial task of this study was to implement the developed and fully tested rain field interpolation module in the existing disaster warning system that monitors the study area. Figure 6.1 illustrates the core component and associated parts of the module as well as its processing sequence.

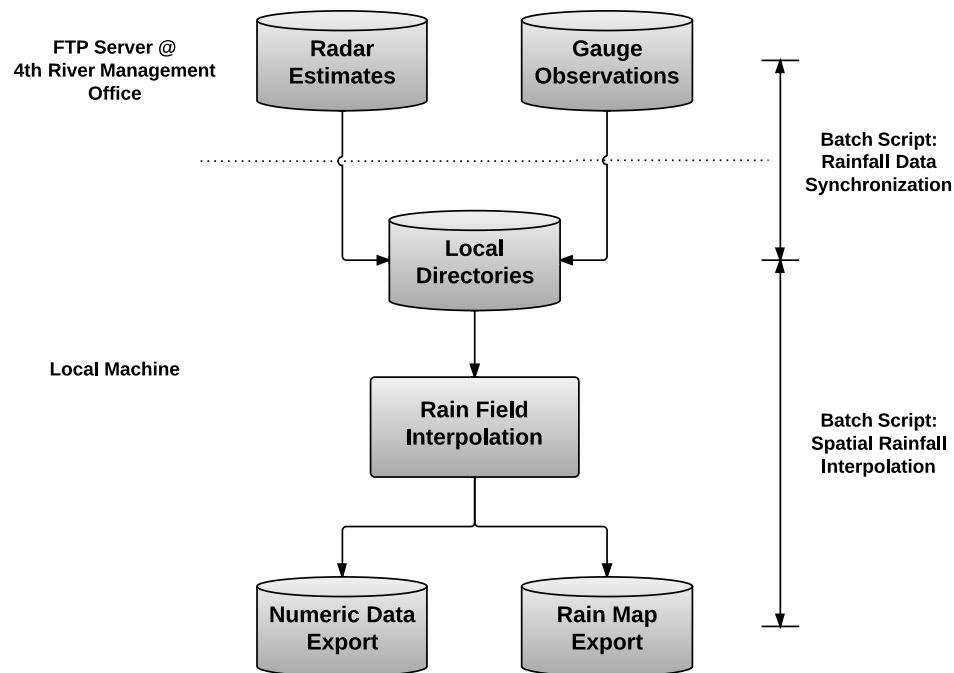


**Figure 6.1:** Automated processing sequence of rain field interpolation.

As indicated in Chapter 4, rainfall data in Taiwan are maintained and managed by the CWB and WRA. The data can be requested by local governmental agencies and universities and delivered in near real-time via the internet for emergency response planning and research purposes. Since the study area is within the jurisdiction of the 4th River

Management Office (4th RMO) of the WRA, a FTP client-server relationship was established with the 4th RMO for this study so the near real-time rainfall data (both radar and gauge) could be downloaded to the local computer for configuring and testing of the rain field interpolation module (see Figure 6.1). In order to ensure the most current data were available on the local computer, a batch script was written and scheduled to be run every five minutes through the Windows Task Scheduler utility. Any new files that were added on the server end would be automatically detected and synchronized on the local end. The main task of the module, rain field interpolation, was to be carried out on an hourly basis by executing another batch script. Both radar estimates and gauge observations for the intended time would be extracted from the synchronized database for processing by the developed interpolation algorithm, and various kinds of end products would be produced. Rain maps were generated as visual references to aid the emergency responding officials in preliminary action planning. Model generated results were also exported into databases for use by the subsequent hydrologic and hydraulic simulations.

The following example code lines are snippets of the batch scripts written to automate the rainfall interpolation process.

```

=====
# The following code line is to initiate the ftp connection.
    winscp.exe /console /script=qpfqpe_060min_sync.txt

# The following code lines are to synchronize the local directory
# that stores radar data to the ftp server.
    option batch abort
    open 4th_River
    synchronize local D:\R_4th_River\Radar_Future_01hr_Binary\
    /qpfqpe_060min/
    exit

# The following code lines are to trigger the rainfall
# prediction algorithm written in R.
    @echo off
    pushd % C:\Program Files\R\R-2.15.2\bin\ %
    Rscript "D:\R_4th_River\Radar_Future_4th_River.R"
=====

```

## Chapter 7

### Results

The RK and merging methods were applied to interpolate rain fields for the Chenyulan River watershed. The interpolated results, along with the results obtained by using the ordinary kriging (OK) method, for the five typhoon events were cross validated with the gauge observations. Cross validation is a validation technique to evaluate the performance of a prediction model by comparing the predicted values of a target variable against the observed data at some known locations, such as gauging stations. In this study, the leave-one-out cross validation, which is widely recognized by statisticians as one of the most efficient ways to validate a prediction model, was performed to assess the accuracy of the rain fields interpolated from the RK, merging and OK methods. The observed rainfall data from one of the gauge stations were first excluded from the interpolation process to be used as the validation dataset, while the observed data from the remaining stations were utilized to interpolate rainfall at the location of that gauge station. The procedure was repeated until each individual gauge station had been rotated through as a validation location. Finally, the interpolated rainfall values were compared to the validation datasets to complete the validation process. In this chapter, the comparisons between the interpolated and observed rainfall data at three selected gauge locations, station C1M440 (upstream), station C1I060 (central region), and station C1I080 (downstream), along the Chenyulan River are presented from three perspectives, which are error analysis, time series, and data scattering along the 45-degree reference line.

Error analysis shows the overall performance of the interpolation techniques. In this study, two indices, the root-mean-square error (RMSE) and coefficient of efficiency (CE), were computed to quantitatively evaluate the errors produced by the interpolation methods. The indices were calculated at the locations of all stations within the gauge network for selected analysis periods from the testing typhoon events. The RMSE at a gauge location

during an analysis period was calculated as

$$RMSE(\mathbf{x}_i) = \sqrt{\frac{\sum_{t=1}^n (\hat{R}_t(\mathbf{x}_i) - R_{gt}(\mathbf{x}_i))^2}{n}}, \quad (7.1)$$

where  $\mathbf{x}_i$  represents the position vector of the  $i$ th gauge station,  $\hat{R}_t(\mathbf{x}_i)$  is the interpolated rainfall value at  $\mathbf{x}_i$  and time  $t$ ,  $R_{gt}(\mathbf{x}_i)$  is the gauge measurement at  $\mathbf{x}_i$  and time  $t$ , and  $n$  is the total number of samples, which is equal to the number of recorded rainfall measurements during the selected analysis period. The CE is defined as

$$CE(\mathbf{x}_i) = 1 - \frac{\sum_{t=1}^n (R_{gt}(\mathbf{x}_i) - \hat{R}_t(\mathbf{x}_i))^2}{\sum_{t=1}^n (R_{gt}(\mathbf{x}_i) - \overline{R_g}(\mathbf{x}_i))^2}, \quad (7.2)$$

where  $\mathbf{x}_i$  represents the position vector of the  $i$ th gauge station,  $\hat{R}_t(\mathbf{x}_i)$  is the interpolated rainfall value at  $\mathbf{x}_i$  and time  $t$ ,  $R_{gt}(\mathbf{x}_i)$  is the gauge measurement at  $\mathbf{x}_i$  and time  $t$ ,  $\overline{R_g}(\mathbf{x}_i)$  is the average of rainfall measurements at  $\mathbf{x}_i$ , and  $n$  is the total number of samples. It should be noted that if the interpolation techniques presented in this study predicted rainfall accurately, the resulting CE would be close to unity as the second term on the right hand side of Equation (7.2) would be relatively small.

In addition to error analysis, which quantitatively evaluates the overall performance of the interpolation techniques, time series plots were generated to compare the interpolated rainfall time series obtained from the RK, merging, and OK methods to the observed rainfall records for selected analysis periods within the testing typhoon events. Time series plots are especially useful for showing time sensitive features such as rainfall peaks during a weather event.

The interpolated rainfall values were also plotted against the gauge observations with the 45-degree reference line overlaid. By looking at the bandwidth of the scattered data points as well as the trend, the performance of the interpolation technique could be evaluated. A narrow bandwidth close to the 45-degree reference line would indicate that the interpolation was done accurately. The interpolated values could be under or over predicted depending on whether the trend line of the data falls within the upper or lower region with respect to the 45-degree reference line.

The results of cross validation for the five historical typhoon events are presented in the following sections.

## 7.1 TYPHOON KALMAEGI

Typhoon Kalmaegi swept through Taiwan in July 2008. A total depth of 700 mm of rain was recorded within a two day period. The results of error analysis based on the RMSE of the interpolated rainfall by the RK, merging, and OK methods as well as the QPESUMS radar estimates are summarized in Table 7.1. The RMSE reduction percentage with respect to the RMSE of the QPESUMS data for each method are also included for comparison purposes. A positive reduction in RMSE indicates that the interpolation techniques could produce more accurate rainfall values than the QPESUMS, whereas a negative reduction would mean that the interpolation methods had produced greater errors as compared to the QPESUMS estimates.

It should be emphasized that the success of spatial interpolation of a target variable, rainfall in this case, relies heavily on the quality of sampling. As discussed previously, inadequate sampling can significantly impact the results of the interpolation. In Table 7.1, the results of error analysis are divided into two groups. The first group includes the gauge stations that are located inside of the Chenyulan River watershed where the stations are closer and denser. The stations that are outside of the watershed and are generally distant from each other belong in the second group. The impact of sampling quality on error reduction is shown as the averaged RMSE reduction percentage for the first group is much higher than that of the second group. For the first group, the RK method yields an averaged RMSE reduction percentage of 26.98% followed closely by a 26.39% reduction from the merging method. The reduction from OK is slightly lower at 22.26%. The averaged error reduction for the second group are 11.12%, 9.35%, and -9.60% for the RK, merging, and OK methods, respectively.

The advantage of using multivariate interpolation techniques, such as RK and merging, as opposed to univariate methods, such as OK, is also demonstrated. Both the RK and merging methods performed more consistently than did the OK method, especially at

locations outside of the watershed boundary where sampling may be insufficient. With the detailed rainfall distribution information provided by the radar estimates of the QPESUMS, the RK and merging methods could still interpolate rainfall reasonably well (averaged RMSE reduction of 11.12% and 9.35%, respectively) while the OK method only used the limited gauge observations for interpolation, hence, leading to poor rainfall predictions (much more negative values of error reduction percentage). It should be noted that an unusually large negative RMSE reduction percentage has been identified at station C1I100 (denoted in red). Such an inaccurate prediction of rainfall may be attributed to inadequate sampling.

The results of error analysis based on the CE of the interpolated rainfall by the RK, merging, and OK methods as well as the QPESUMS radar estimates are summarized in Table 7.2. As introduced earlier, a CE value approaching unity would indicate that the interpolated values are close to the observed values. The averaged CE of the QPESUMS data from the gauge stations located within the watershed boundary is 0.72. The averaged CE values of the interpolated rainfall obtained from the RK, merging, and OK methods are 0.84, 0.84, and 0.82, respectively. It can be seen that more accurate rainfall prediction can be made by all three methods. The CE improvement percentage with respect to the CE of the QPESUMS data for each method are included in Table 7.2 for comparison purposes. A positive improvement in CE indicates that the interpolation techniques could produce more accurate rainfall values than the QPESUMS, whereas a negative improvement would mean that the interpolation methods had produced greater errors as compared to the QPESUMS estimates. The averaged CE improvement percentage for RK, merging, and OK are 16.60%, 15.95%, and 13.30%, respectively. The analysis has shown again that RK outperforms the merging method slightly, and both the RK and merging methods (multivariate) are superior to OK (univariate). Similar to the above RMSE based analysis, the averaged CE improvement percentage for the gauge stations outside of the watershed are lower at 6.92%, 6.06%, and -12.91% (RK, merging, and OK) reflecting the effect of sampling quality. However, the performance of RK and merging are still substantially better than OK.

The time variations of rainfall depth (hyetographs) during the six-hour peak period at stations C1M440, C1I060, and C1I080 for Typhoon Kalmaegi are presented in Figures 7.1(a), 7.1(b), and 7.1(c), respectively. The results include the interpolated rainfall

**Table 7.1:** RMSE comparisons between RK, merging, and OK techniques for Typhoon Kalmaegi.

Inside Watershed Boundary							
Station ID	QPESUMS	RK	Red., %	Merging	Red., %	OK	Red., %
1510P030	2.79	2.56	8.17	2.66	4.56	2.72	2.56
1510P087	1.95	0.98	49.97	0.97	50.11	0.95	51.46
C0H9A0	2.00	1.55	22.50	1.62	18.86	1.61	19.76
C1I060	2.23	1.20	46.25	1.21	45.89	1.46	34.44
C1I070	1.93	1.36	29.66	1.39	27.94	1.48	23.47
C1I080	2.26	1.59	29.62	1.51	32.99	1.80	20.14
C1I160	2.02	1.53	24.32	1.49	26.15	1.52	24.65
C1I290	2.20	1.59	27.87	1.63	25.99	1.79	18.86
C1I300	1.89	1.33	29.74	1.35	28.26	1.47	22.15
C1I340	2.05	1.58	22.83	1.61	21.62	1.61	21.29
C1I350	1.94	1.72	11.40	1.72	11.57	1.71	11.90
C1M440	2.01	1.58	21.38	1.56	22.79	1.68	16.49
Average	2.11	1.55	26.98	1.56	26.39	1.65	22.26
Outside Watershed Boundary							
Station ID	QPESUMS	RK	Red., %	Merging	Red., %	OK	Red., %
C1M630	2.15	2.17	-0.73	2.14	0.35	3.67	-70.71
C1V170	1.47	1.27	13.27	1.30	11.21	1.64	-11.54
C1V460	2.06	1.93	6.35	1.81	12.16	1.92	6.58
1510P088	2.16	1.78	17.68	1.78	17.59	1.79	17.02
1730P132	2.74	2.25	18.08	2.21	19.64	2.14	21.95
467530	2.47	2.18	11.83	2.35	4.94	2.38	3.75
467550	1.90	1.83	3.89	1.83	4.11	1.89	0.57
C0I090	2.18	1.86	14.78	1.96	10.15	2.56	-17.21
C1I040	2.01	1.99	0.70	2.04	-1.35	2.38	-18.45
<b>C1I100</b>	<b>1.09</b>	<b>1.40</b>	<b>-28.75</b>	<b>1.35</b>	<b>-23.58</b>	<b>3.72</b>	<b>-241.91</b>
C1I120	2.28	2.09	8.38	2.13	6.47	2.66	-16.96
C1I150	1.92	1.66	13.69	1.72	10.31	1.92	-0.08
C1I170	1.60	1.70	-6.44	1.70	-6.51	2.59	-61.94
C1I270	1.61	1.30	19.34	1.49	7.76	1.90	-17.92
C1I310	2.00	1.30	34.81	1.32	34.12	1.39	30.58
Average	2.04	1.81	11.12	1.84	9.35	2.20	-9.60

values from the RK, merging, and OK methods, the original radar data from the QPESUMS, and the gauge measurements. It can be seen in Figures 7.1(a)-7.1(c) that the QPESUMS data are shown as smooth curves without abrupt rises and falls, thus, underestimating peaks and overestimating troughs of the event. In contrast, the interpolated rainfall values by the

**Table 7.2:** CE comparisons between RK, merging, and OK techniques for Typhoon Kalmaegi.

Inside Watershed Boundary							
Station ID	QPESUMS	RK	Imprv., %	Merging	Imprv., %	OK	Imprv., %
1510P030	0.48	0.56	16.90	0.53	9.61	0.51	5.46
1510P087	0.78	0.95	20.65	0.95	20.69	0.95	21.06
C0H9A0	0.81	0.88	9.66	0.87	8.27	0.87	8.61
C1I060	0.80	0.94	17.85	0.94	17.75	0.91	14.31
C1I070	0.81	0.91	11.60	0.90	11.03	0.89	9.51
C1I080	0.67	0.84	24.50	0.85	26.75	0.79	17.59
C1I160	0.69	0.82	18.87	0.83	20.08	0.83	19.09
C1I290	0.68	0.83	22.36	0.83	21.09	0.79	15.93
C1I300	0.66	0.83	25.65	0.83	24.58	0.80	19.95
C1I340	0.78	0.87	11.17	0.87	10.64	0.87	10.50
C1I350	0.76	0.81	6.80	0.81	6.90	0.81	7.08
C1M440	0.74	0.84	13.22	0.85	13.98	0.82	10.47
Average	0.72	0.84	16.60	0.84	15.95	0.82	13.30
Outside Watershed Boundary							
Station ID	QPESUMS	RK	Imprv., %	Merging	Imprv., %	OK	Imprv., %
C1M630	0.85	0.84	-0.27	0.85	0.13	0.55	-35.02
C1V170	0.64	0.73	13.77	0.72	11.76	0.56	-13.56
C1V460	0.75	0.78	4.19	0.80	7.78	0.78	4.33
1510P088	0.71	0.81	12.91	0.81	12.85	0.80	12.47
1730P132	0.65	0.77	17.35	0.78	18.69	0.79	20.62
467530	0.75	0.81	7.44	0.77	3.22	0.77	2.46
467550	0.70	0.72	3.27	0.72	3.45	0.70	0.49
C0I090	0.72	0.79	10.85	0.77	7.64	0.61	-14.82
C1I040	0.83	0.83	0.29	0.82	-0.56	0.76	-8.28
<b>C1I100</b>	<b>0.25</b>	<b>-0.24</b>	<b>-197.72</b>	<b>-0.15</b>	<b>-158.53</b>	<b>-7.77</b>	<b>-3214.32</b>
C1I120	0.69	0.74	7.31	0.73	5.70	0.57	-16.75
C1I150	0.81	0.86	5.92	0.85	4.54	0.81	-0.04
C1I170	0.53	0.47	-11.65	0.47	-11.80	-0.23	-142.35
C1I270	0.84	0.90	6.57	0.87	2.81	0.78	-7.34
C1I310	0.75	0.89	18.98	0.89	18.68	0.88	17.10
Average	0.73	0.78	6.92	0.77	6.06	0.65	-12.91

three methods follow the gauge measurements more closely (capturing peaks and troughs). Because the RK and merging methods use the QPESUMS estimates as an auxiliary variable to interpolate rainfall, the interpolation can be perceived as a process to adjust the QPESUMS data to match the observed rainfall. It is shown in the figures that both methods

produce similar results and slightly outperform OK during the six-hour period. In addition, the interpolated rainfall values at station C1I060 appear to have a better agreement with the gauge data than at stations C1M440 and C1I080. The hyetographs at station C1I060 showing the complete rainfall data of the event from RK, merging, QPESUMS, and gauges for Typhoon Kalmaegi are presented in Figure 7.2 as a reference. Again, RK and merging have demonstrated to be able to effectively improve the QPESUMS data.

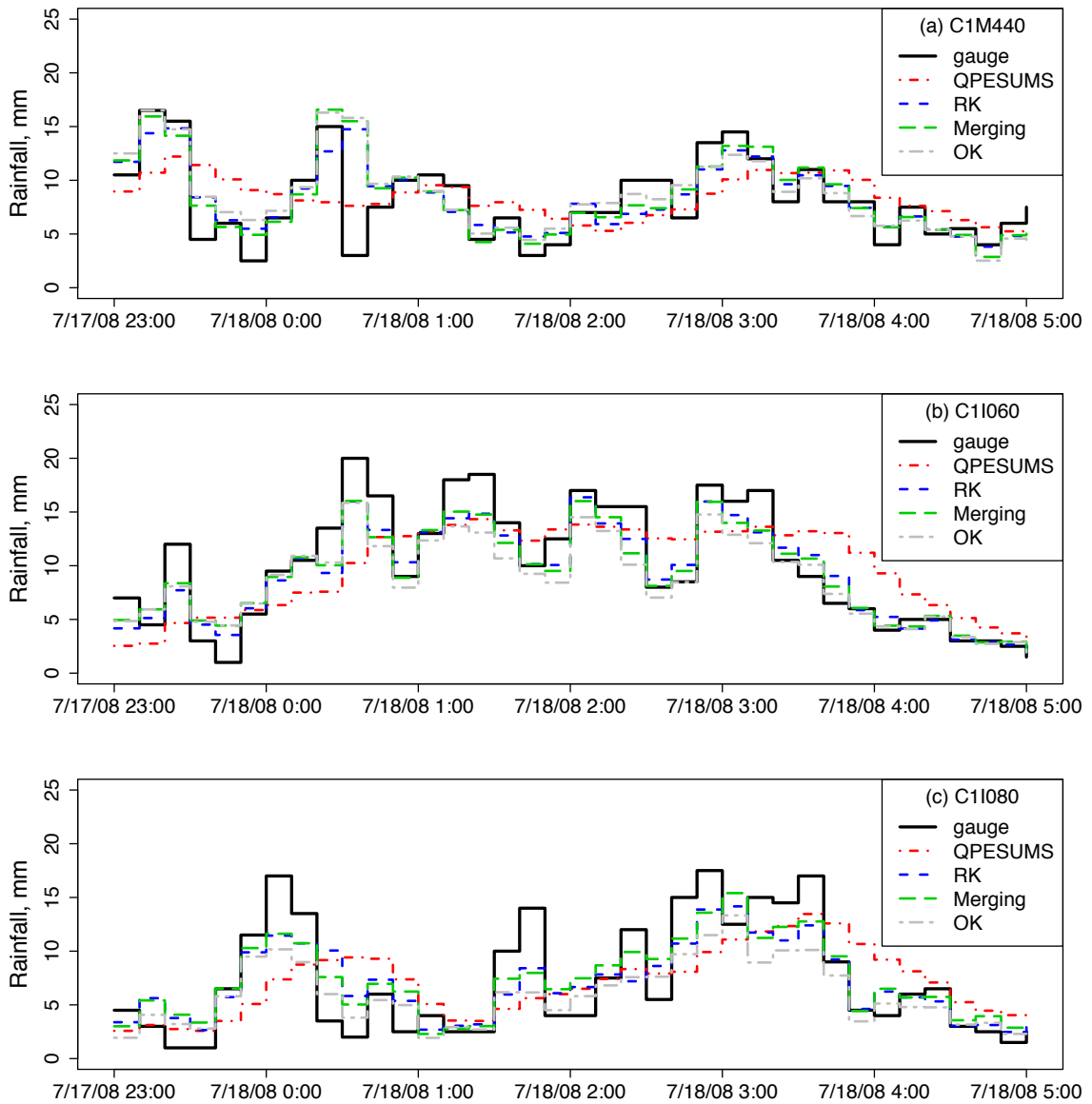
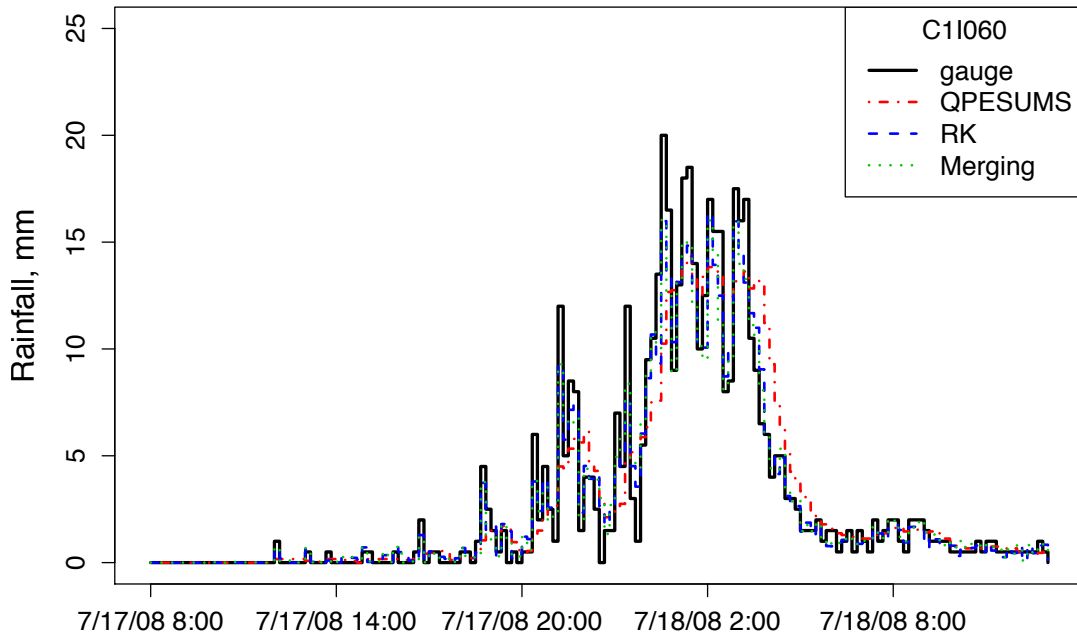
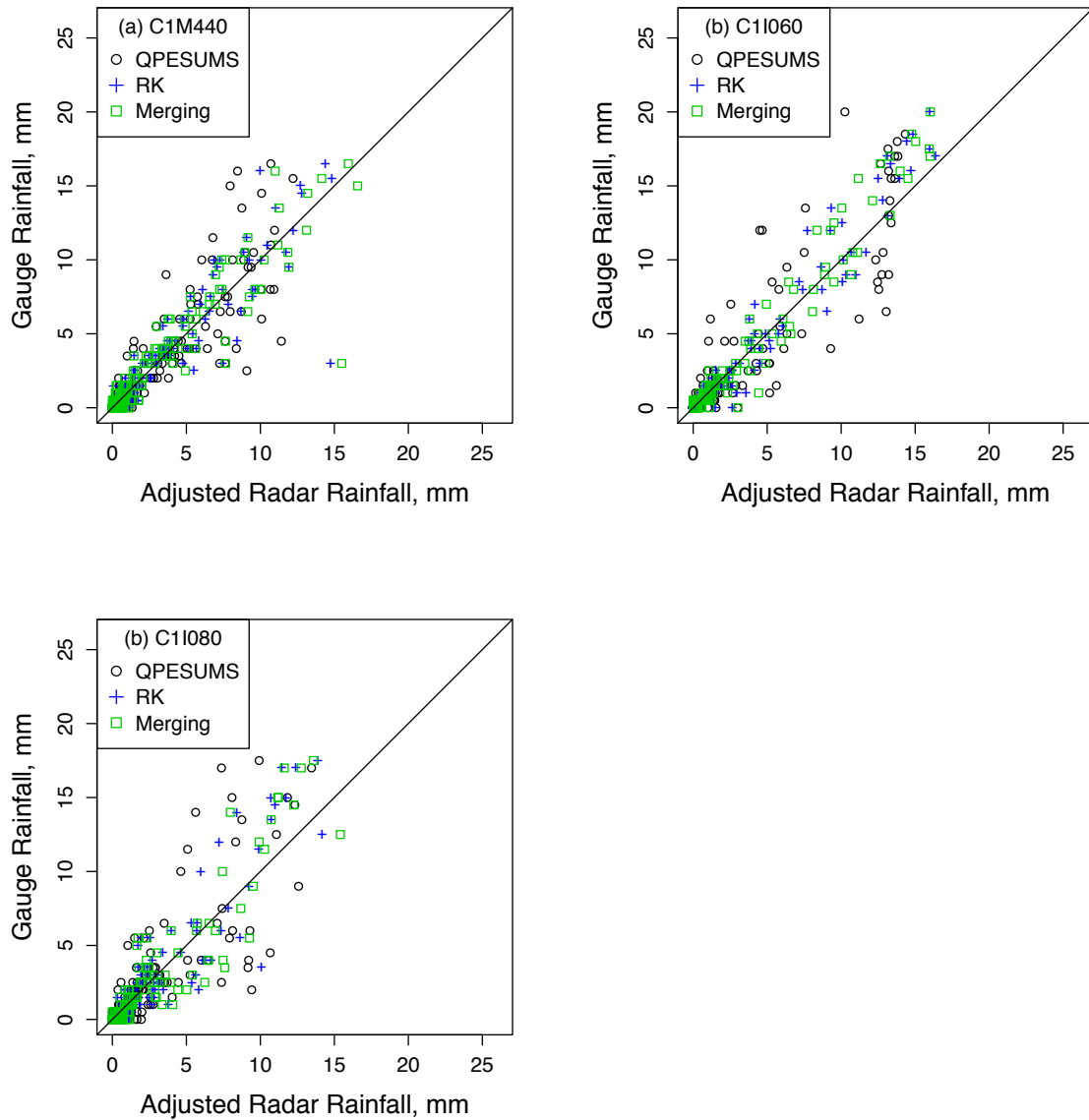


Figure 7.1: Peak hour hyetograph comparisons, Typhoon Kalmaegi.



**Figure 7.2:** Full event hyetograph comparisons at station C1I060, Typhoon Kalmaegi.

The gauge data recorded during the entire typhoon event and the corresponding adjusted radar values as pairs of data points were plotted with the 45-degree reference line overlaid for comparisons. The plots are shown in Figures 7.3(a), 7.3(b), and 7.3(c), respectively, for stations C1M440, C1I060, and C1I080. The unadjusted QPESUMS data were also included. It can be concluded that, at each station, the adjusted radar data agree reasonably well with the gauge data as indicated by the narrower bandwidth of data points close to the 45-degree reference line. The unadjusted QPESUMS data, however, are shown to scatter to a wider extent (wider bandwidth). The RK and merging methods are again demonstrated to be able to reliably perform the correction procedures on the raw radar data. As a result, more realistic radar rainfall data can be generated for potential modeling uses. Based on the results shown in Figures 7.3(a)-7.3(c), a better agreement between the gauge data and adjusted radar values can be noticed for stations C1I060 and C1M440. For station C1I080, both the RK and merging methods tend to slightly underadjust the raw radar data for rainfall depths greater than 10 mm (interpolated data points from RK and merging fall within the upper region).



**Figure 7.3:** Adjusted radar rainfall v.s. gauge observations, Typhoon Kalmaegi.

## 7.2 TYPHOON MORAKOT

Typhoon Morakot was the next event tested to further the verification of the proposed RK and merging algorithms. The results of error analysis based on the calculated RMSE and CE indices are summarized in Tables 7.3 and 7.4. The averaged RMSE reduction percentage of 39.79%, 37.79%, and 32.71% (RK, merging, and OK) and the averaged CE improvement percentage of 36.05%, 34.72%, and 31.08% (RK, merging, and OK) for the gauge stations located in the Chenyulan River watershed were determined. Based on the

results of the analysis, RK is shown to be most accurate in interpolating rainfall followed by merging and, lastly, OK. Similar to the case of Typhoon Kalmaegi, the performance of the OK method for locations outside of the watershed is not as consistent as the RK and merging methods due to inadequate sampling and limitations of the methodology (see Tables 7.3 and 7.4 for results).

The hyetographs covering six hours of peak rainfall data are shown respectively in Figures 7.4(a), 7.4(b), and 7.4(c) for stations C1M440, C1I060, and C1I080. The plots include the interpolated results from the RK, merging, and OK methods. Observations from the gauges and unadjusted QPESUMS radar estimates are also plotted for comparisons. It can be clearly seen that the unadjusted QPESUMS data show poor representation of the real time-varying rainfall values. The adjustment procedures from RK and merging are shown to be able to substantially improve the radar data to fit closely to the gauge measurements, especially within the period from midnight to 1:00 a.m. on August 9, 2009 during which possible systematic errors might have been introduced. Similar to the results shown in Figures 7.1(a)-7.1(c), the performance on rainfall interpolation by the RK, merging, and OK methods at station C1I060 is better than at stations C1M440 and C1I080. At station C1M440, the three methods underpredicted the rainfall peaks. Again, the results from RK and merging are similar. When comparing to the interpolated values by OK, the RK and merging methods are shown to outperform OK. As a reference, the time series of rainfall interpolated by RK and merging for the entire event of Typhoon Morakot at station C1I060 can be seen in Figure 7.5.

To better the comparisons on the performance of the RK, merging, and OK methods, all interpolated rainfall values for the event were plotted against the gauge measurements in Figures 7.6(a)-7.6(c) for stations C1M440, C1I060, and C1I080, respectively. The 45-degree reference line represents the perfect agreement. As shown in Figures 7.6(a)-7.6(c), the data points of the rainfall values predicted by the spatial interpolation algorithms of RK and merging scatter around the reference line more closely than those of the QPESUMS data. The plots also support the statement made above that the adjusted radar rainfall values at station C1I060 among the three test stations are shown to have the best agreement with the gauge data. At station C1M440, both the RK and merging tend to slightly underpredict

**Table 7.3:** RMSE comparisons between RK, merging, and OK techniques for Typhoon Morakot.

Inside Watershed Boundary							
Station ID	QPESUMS	RK	Red., %	Merging	Red., %	OK	Red., %
1510P030	1.41	0.86	39.21	0.87	38.19	0.86	39.23
1510P087	1.36	0.67	50.72	0.68	49.84	0.71	47.71
C0H9A0	1.78	1.13	36.48	1.23	30.73	1.32	26.04
C1I060	1.33	0.61	54.31	0.61	53.91	0.77	41.81
C1I070	1.41	0.97	31.28	1.01	28.14	0.96	31.91
C1I080	1.15	0.68	41.15	0.68	40.74	0.78	32.00
C1I160	1.09	0.60	44.71	0.63	41.81	0.69	37.04
C1I290	1.36	0.89	34.86	0.90	33.99	0.97	28.63
C1I300	0.94	0.64	31.46	0.67	28.55	0.82	13.02
C1I340	1.79	1.14	36.28	1.11	37.85	1.17	34.51
C1I350	1.32	0.71	46.57	0.74	44.09	0.76	42.56
C1M440	1.83	1.27	30.42	1.36	25.65	1.50	18.04
Average	1.40	0.85	39.79	0.88	37.79	0.94	32.71

Outside Watershed Boundary							
Station ID	QPESUMS	RK	Red., %	Merging	Red., %	OK	Red., %
C1M630	1.91	1.77	7.64	1.83	4.52	2.56	-33.91
C1V170	1.76	1.58	9.78	1.60	8.95	2.08	-18.67
C1V460	2.12	1.72	18.83	1.94	8.67	2.04	3.77
1510P088	1.39	1.13	19.00	1.12	19.66	1.00	28.42
1730P132	2.10	1.74	17.36	1.86	11.59	1.88	10.28
467530	2.51	2.09	16.70	2.25	10.36	2.76	-9.81
467550	1.65	1.41	14.25	1.61	2.18	2.05	-24.31
C0I090	1.41	1.12	20.34	1.19	15.74	1.81	-28.07
C1I040	1.34	0.99	26.02	1.08	19.83	1.53	-13.96
C1I100	0.86	0.88	-2.47	0.88	-2.34	1.34	-56.44
C1I120	0.81	0.83	-2.03	0.88	-8.95	1.65	-103.53
C1I150	1.07	0.75	29.84	0.84	21.44	1.13	-5.29
C1I170	0.94	0.83	11.80	1.00	-6.15	1.33	-41.16
C1I270	0.94	0.61	34.87	0.77	18.16	0.99	-6.23
C1I310	1.07	0.57	47.14	0.54	49.89	0.59	45.08
Average	1.46	1.20	17.94	1.29	11.57	1.65	-16.92

the high rainfall values (data points fall within the upper region).

The 2-D rain fields showing the overall spatial distribution of the interpolated rainfall data from the RK, merging, and OK methods as well as the QPESUMS estimates are presented respectively in Figures 7.7, 7.8, and 7.9 for the instants of 23:00 p.m. on August 8,

**Table 7.4:** CE comparisons between RK, merging, and OK techniques for Typhoon Morakot.

Inside Watershed Boundary							
Station ID	QPESUMS	RK	Imprv., %	Merging	Imprv., %	OK	Imprv., %
1510P030	0.59	0.85	43.04	0.85	42.19	0.85	43.05
1510P087	0.59	0.90	52.22	0.90	51.61	0.89	50.11
C0H9A0	0.74	0.90	20.83	0.88	18.17	0.86	15.82
C1I060	0.63	0.92	46.64	0.92	46.42	0.87	38.99
C1I070	0.62	0.82	32.57	0.80	29.84	0.82	33.10
C1I080	0.65	0.88	35.51	0.88	35.25	0.84	29.21
C1I160	0.65	0.89	37.09	0.88	35.33	0.86	32.24
C1I290	0.57	0.82	44.15	0.81	43.27	0.78	37.63
C1I300	0.64	0.83	29.74	0.82	27.45	0.73	13.66
C1I340	0.70	0.88	25.64	0.88	26.49	0.87	24.65
C1I350	0.62	0.89	43.49	0.88	41.84	0.88	40.79
C1M440	0.70	0.86	21.64	0.84	18.76	0.80	13.77
Average	0.64	0.87	36.05	0.86	34.72	0.84	31.08
Outside Watershed Boundary							
Station ID	QPESUMS	RK	Imprv., %	Merging	Imprv., %	OK	Imprv., %
C1M630	0.71	0.75	6.00	0.74	3.61	0.48	-32.38
C1V170	0.25	0.39	57.10	0.37	52.51	-0.06	-125.32
C1V460	0.56	0.71	26.36	0.64	12.82	0.60	5.71
1510P088	0.44	0.63	43.74	0.64	45.10	0.71	62.01
1730P132	0.46	0.63	36.98	0.58	25.45	0.57	22.74
467530	0.69	0.78	14.02	0.75	8.99	0.62	-9.43
467550	0.63	0.73	15.48	0.65	2.52	0.43	-31.90
C0I090	0.70	0.81	15.31	0.79	12.15	0.52	-26.83
C1I040	0.68	0.82	21.45	0.79	16.93	0.58	-14.15
C1I100	0.49	0.46	-5.21	0.47	-4.92	-0.25	-150.67
C1I120	0.48	0.45	-4.51	0.38	-20.63	-1.17	-346.61
C1I150	0.51	0.76	47.99	0.70	36.17	0.46	-10.26
C1I170	0.61	0.70	14.14	0.56	-8.08	0.22	-63.21
C1I270	0.57	0.82	43.41	0.71	24.90	0.51	-9.69
C1I310	0.65	0.90	38.90	0.91	40.43	0.89	37.70
Average	0.56	0.69	24.74	0.64	16.53	0.34	-46.15

and 0:00 a.m. and 1:00 a.m. on August 9, 2009. As previously discussed, the QPESUMS radar estimates generally underpredict peaks and overpredict troughs of an event. With the adjustments made by the RK and merging methods, the spatial features contained in the QPESUMS data are intensified as displayed in Figures 7.7-7.9. In addition, as both

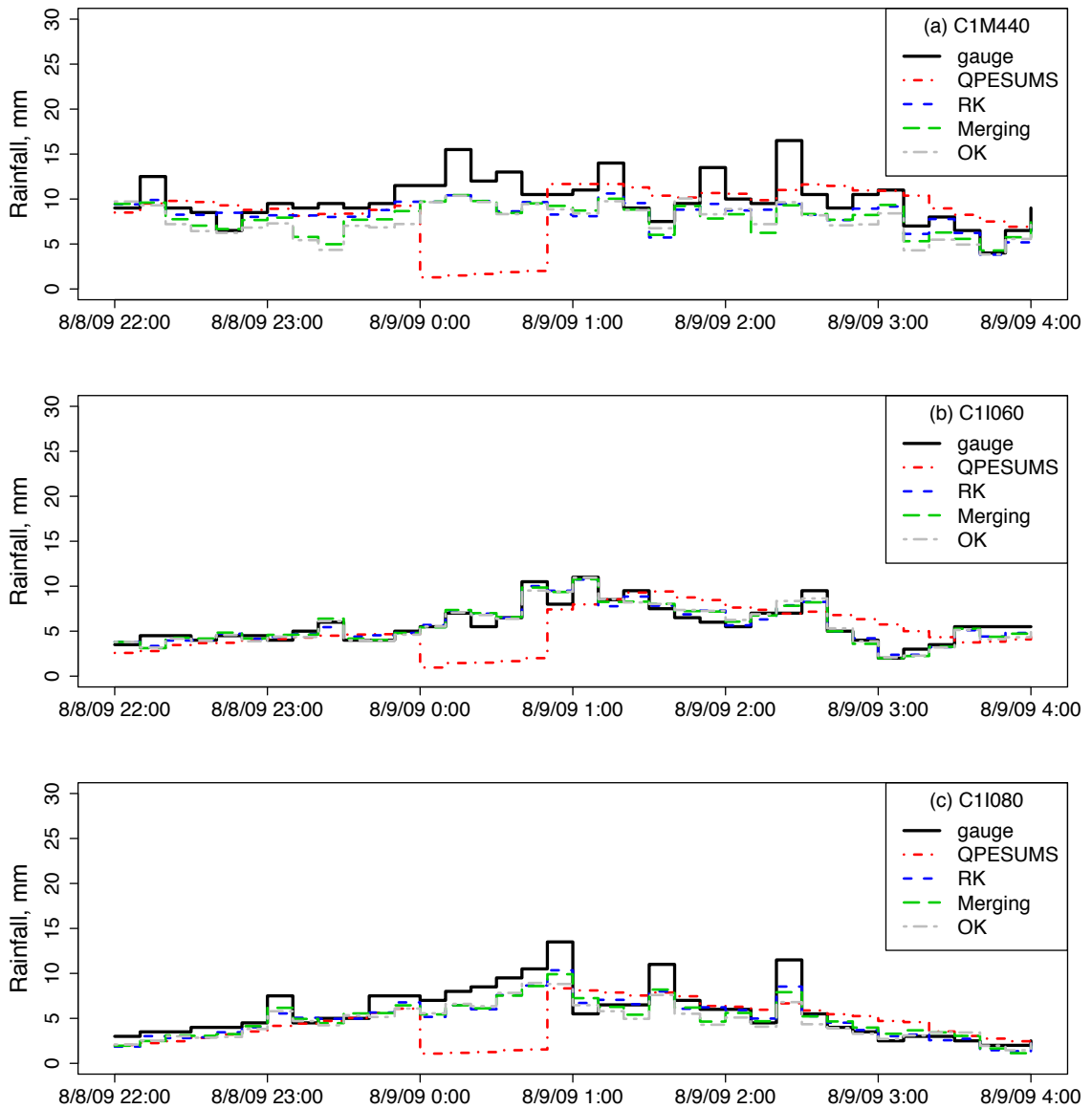


**Figure 7.4:** Peak hour hyetograph comparisons, Typhoon Morakot.

the RK and merging methods incorporate the QPESUMS data as an auxiliary variable in the interpolation processes, the spatial rainfall details are preserved, whereas the rain maps produced by the OK method (using only gauge observations) in general do not contain as many details.

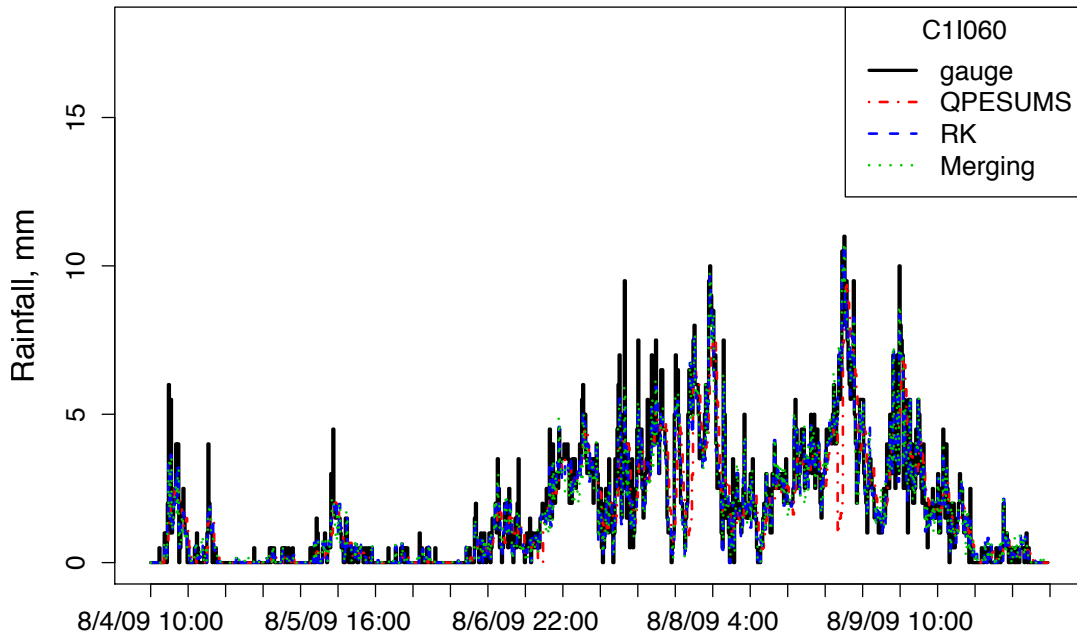
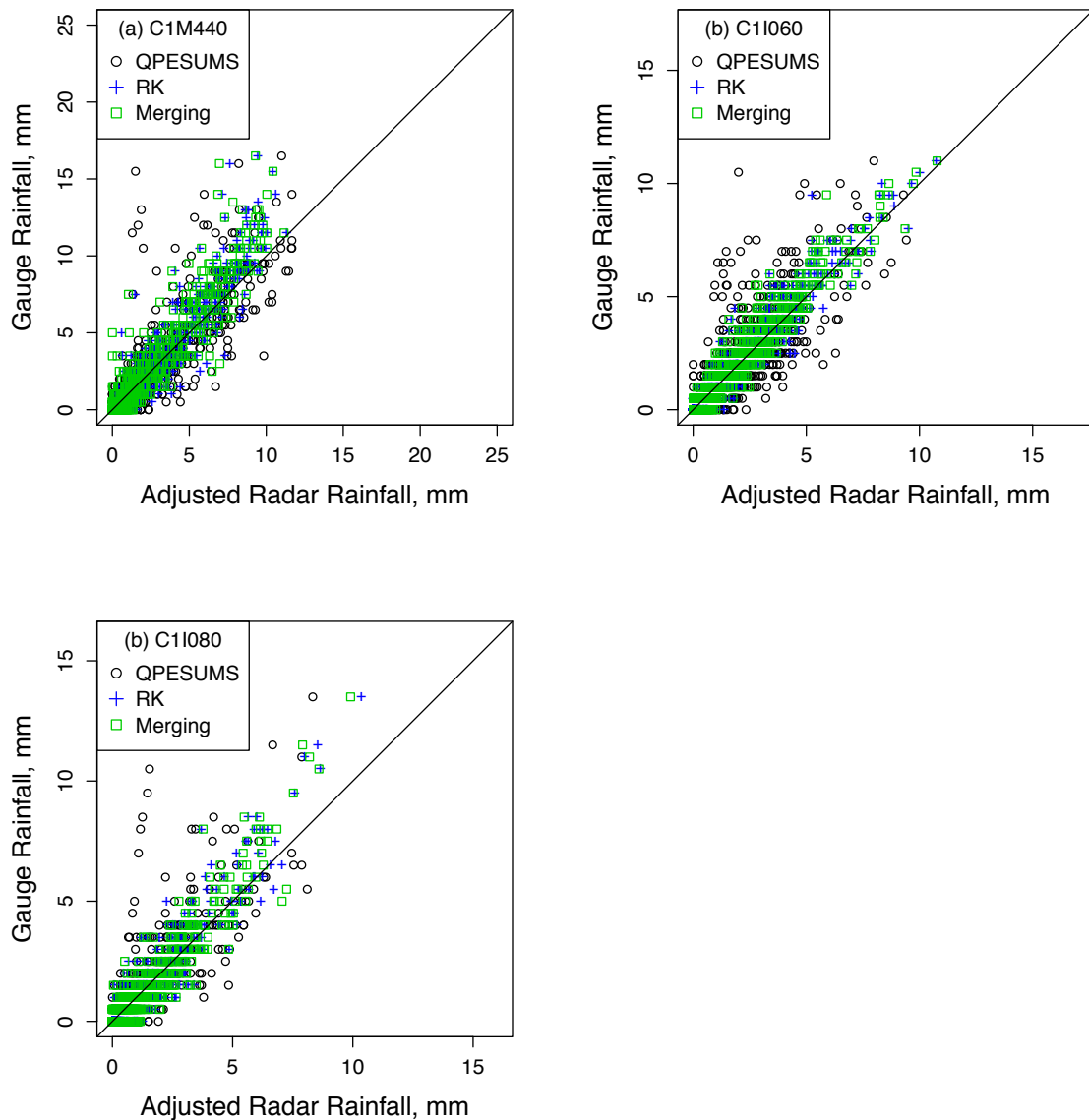


Figure 7.5: Full event hyetograph comparisons at station C1I060, Typhoon Morakot.

### 7.3 TYPHOONS FUNGWONG, SINLAKU, AND FANAPI

The results of cross validation of the interpolated rainfall by the RK, merging, and OK methods and their corresponding predicting performance for the five typhoons in general are very similar. For Typhoons Kalmaegi and Morakot, the results were presented in a much detailed fashion to discuss some of the common features that are shared by the typhoons. For Typhoons Fungwong, Sinlaku, and Fanapi, the comparisons of the error analysis are summarized in the tabular format. The comparisons of the rainfall time series as well as data points scattering patterns at stations C1M440, C1I060, and C1I080 are included in Figure 7.12 to Figure 7.20. The results in general have indicated that the RK and merging methods have performed reasonably well in interpolating rainfall. However, the emphasis of discussion will be placed on the special findings, such as situations during the events where unusually large interpolation errors had occurred.

The summaries of the averaged RMSE reduction percentage and the averaged CE improvement percentage of the RK, merging, and OK methods for the gauge stations located in the Chenyulan River watershed for Typhoons Fungwong, Sinlaku, and Fanapi are provided in Table 7.5. The performance of the three interpolation techniques can be ranked



**Figure 7.6:** Adjusted radar rainfall v.s. gauge observations, Typhoon Morakot.

from best to worst, respectively, as RK, merging, and OK, as the results indicated in the table. It is also noticed that the three interpolation methods were not as effective in predicting rainfall for Typhoon Fanapi as with Typhoons Fungwong and Sinlaku as the averaged percentage of the RMSE reduction and CE improvement are shown to be lower for Typhoon Fanapi comparing to the other two events. Despite the overall degraded performance of the methods, RK appears to have produced more accurate rainfall while both merging and OK become inconsistent (negative numbers of percentage). This is an interesting finding that

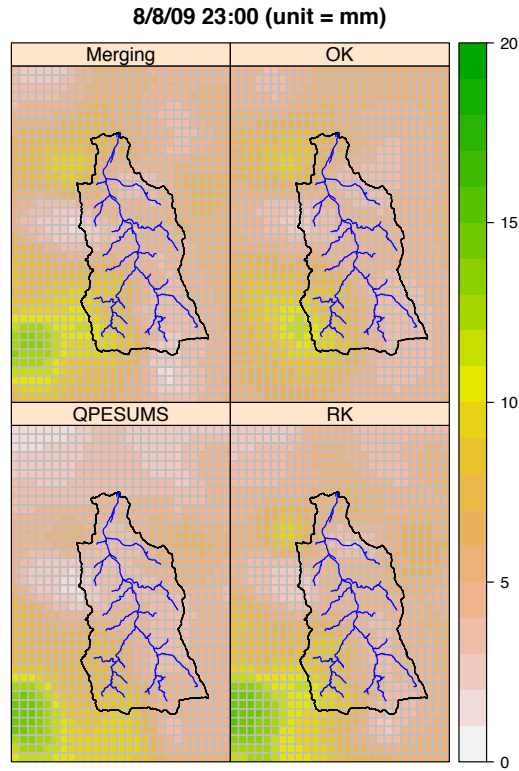


**Figure 7.7:** 2-D rain fields, 23:00 08/08/2009, Typhoon Morakot.

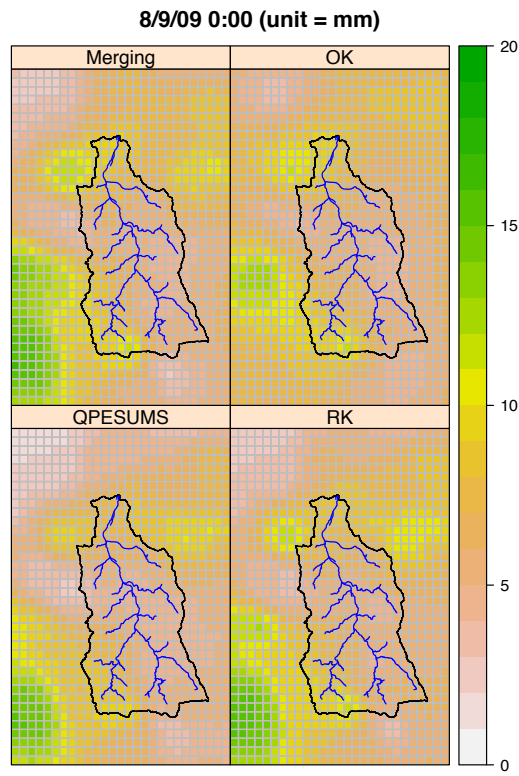


**Figure 7.8:** 2-D rain fields, 00:00 08/09/2009, Typhoon Morakot.

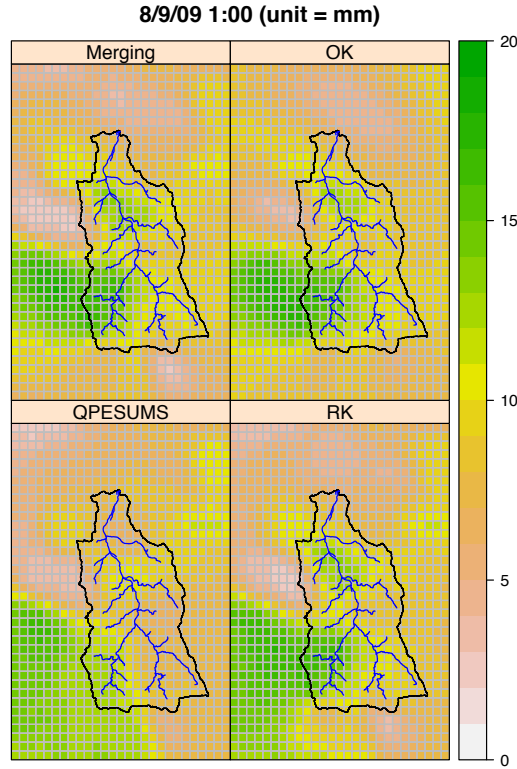


**Figure 7.9:** 2-D rain fields, 01:00 08/09/2009, Typhoon Morakot.

the merging method had failed to yield comparable rainfall predictions to the RK method for the first time among the five typhoon events analyzed.

The complete results of the error analysis can be found in Tables 7.7-7.12. Unusually large rainfall interpolation errors can be identified at gauge station C1M440 for Typhoon Fungwong as denoted in red in Tables 7.7 and 7.8 and station C1I070 during Typhoon Fanapi as shown in Tables 7.11 and 7.12. In order to investigate the cause of the errors, the interpolated rainfall as well as gauge observations during a selected six-hour period from the two closest gauge stations (C1V460 and 1730P132 for C1M440; C1I060 and C1I340 for C1I070) are included and compared in Figure 7.10 and Figure 7.11, respectively, for the two events. From both figures, inconsistency between the gauge records and radar estimates from the QPESUMS can be clearly seen. The recorded rainfall and radar data agree with each other fairly well in Figure 7.10(a) and Figure 7.10(b), whereas the two types of data deviate from each other in Figure 7.10(c). Similarly, the gauge and radar rainfall follow each other well in Figure 7.11(b) and Figure 7.11(c), however, it is not the case in Figure 7.11(a).

**Table 7.5:** Summaries of error analysis between RK, merging, and OK techniques for Typhoons Fungwong, Sinlaku, and Fanapi.

Typhoon Fungwong			
	RK, %	Merging, %	OK, %
Averaged RMSE Reduction	26.13	22.60	19.41
Averaged CE Improvement	28.64	25.70	24.05
Typhoon Sinlaku			
	RK, %	Merging, %	OK, %
Averaged RMSE Reduction	24.57	22.22	15.49
Averaged CE Improvement	29.43	24.08	18.46
Typhoon Fanapi			
	RK, %	Merging, %	OK, %
Averaged RMSE Reduction	18.12	6.19	-11.58
Averaged CE Improvement	11.29	-11.20	-50.81

As introduced previously, both the RK and merging methods involve the kriging process to determine the residual value (amount of rainfall adjustment) at every location on the rain field. Most importantly, the kriging technique is based on the similarity theory such that physical properties at locations close to each other in a geospatial space should be similar. The inconsistency between the gauge measurements and radar estimates from the three close by gauges has clearly contradicted the fundamental assumptions of the kriging technique. As a result, the accuracy of residuals (or rainfall adjustments) generated by the RK and merging methods could be affected as the two cases discussed.

#### 7.4 SIGNIFICANCE OF AUXILIARY PREDICTORS

The RK method uses radar estimates and elevation values as auxiliary predictors to interpolate rain fields covering the study watershed. In order to evaluate the correlation of each predictor with the gauge observations, statistical analyses were performed on the regression models developed for the five typhoon events. The results of the analyses are summarized in Table 7.6. It can be observed that radar estimates are the dominant predictor

for the five events as indicated by the much greater t-values as compared to elevation values. Therefore, the rainfall prediction in the regression part of the interpolation process would be mostly influenced by the radar estimates.

**Table 7.6:** Significance of auxiliary predictors.

	Kalmaegi	Morakot	Fungwong	Sinlaku	Fanapi
	t-value	t-value	t-value	t-value	t-value
radar estimates	234.7	258.2	114.3	217.1	132.8
elevation	4.1	11.5	14.8	9.0	7.6

**Table 7.7:** RMSE comparisons between RK, merging, and OK techniques for Typhoon Fungwong.

Inside Watershed Boundary							
Station ID	QPESUMS	RK	Red., %	Merging	Red., %	OK	Red., %
1510P030	1.09	1.02	6.14	1.02	6.40	1.00	8.00
1510P087	0.79	0.49	37.17	0.49	38.03	0.50	35.99
C0H9A0	0.89	0.72	19.08	0.71	20.85	0.73	18.16
C1I060	0.76	0.43	44.08	0.44	42.64	0.51	32.97
C1I070	0.65	0.54	16.80	0.54	16.47	0.55	16.00
C1I080	0.67	0.47	29.18	0.52	21.86	0.55	17.58
C1I160	0.72	0.42	41.57	0.46	36.60	0.49	32.40
C1I290	0.58	0.42	27.52	0.46	20.03	0.51	11.48
C1I300	0.66	0.49	26.27	0.53	19.69	0.56	15.25
C1I340	0.69	0.50	27.57	0.52	23.68	0.53	22.85
C1I350	0.65	0.57	12.09	0.64	2.40	0.63	2.88
<b>C1M440</b>	<b>0.21</b>	<b>0.81</b>	<b>-284.96</b>	<b>0.89</b>	<b>-322.14</b>	<b>1.55</b>	<b>-633.11</b>
Average	0.74	0.55	26.13	0.58	22.60	0.60	19.41
Outside Watershed Boundary							
Station ID	QPESUMS	RK	Red., %	Merging	Red., %	OK	Red., %
C1M630	0.97	0.89	8.87	0.84	13.59	1.02	-5.46
C1V170	1.06	0.93	12.73	0.96	9.90	1.08	-1.26
C1V460	1.25	1.18	5.61	1.32	-5.68	1.61	-28.56
1510P088	1.26	1.03	18.04	1.11	12.31	1.06	15.99
1730P132	2.05	1.71	16.67	1.65	19.52	1.37	33.12
467530	2.25	1.85	17.62	1.91	14.95	2.14	4.71
467550	0.80	0.73	8.77	0.73	7.66	0.88	-11.04
C0I090	0.68	0.58	15.06	0.62	8.23	0.75	-10.26
C1I040	0.53	0.48	8.28	0.50	5.68	0.59	-12.02
C1I100	0.83	0.68	17.97	0.71	14.29	0.81	2.10
C1I120	0.45	0.51	-12.50	0.53	-17.19	0.95	-107.98
C1I150	0.63	0.54	15.03	0.54	15.33	0.68	-6.95
C1I170	0.54	0.54	-0.72	0.60	-11.52	0.85	-56.96
C1I270	0.60	0.49	18.05	0.54	9.25	0.58	2.11
C1I310	0.83	0.52	37.83	0.54	34.38	0.57	30.87
Average	0.98	0.84	12.49	0.87	8.71	1.00	-10.11

**Table 7.8:** CE comparisons between RK, merging, and OK techniques for Typhoon Fungwong.

Inside Watershed Boundary							
Station ID	QPESUMS	RK	Imprv., %	Merging	Imprv., %	OK	Imprv., %
1510P030	0.20	0.30	47.63	0.30	49.63	0.32	61.45
1510P087	0.65	0.86	32.04	0.87	32.61	0.86	31.25
C0H9A0	0.73	0.82	12.73	0.83	13.78	0.82	12.18
C1I060	0.68	0.90	32.94	0.89	32.15	0.85	26.39
C1I070	0.56	0.70	24.14	0.69	23.71	0.69	23.08
C1I080	0.63	0.81	29.90	0.77	23.36	0.75	19.24
C1I160	0.57	0.85	48.76	0.83	44.27	0.81	40.20
C1I290	0.66	0.82	24.56	0.78	18.66	0.73	11.20
C1I300	0.61	0.79	29.52	0.75	22.96	0.72	18.22
C1I340	0.68	0.83	21.92	0.82	19.26	0.81	18.67
C1I350	0.68	0.75	10.91	0.69	2.27	0.69	2.73
<b>C1M440</b>	<b>-0.10</b>	<b>-15.26</b>	<b>-15566.61</b>	<b>-18.56</b>	<b>-18946.73</b>	<b>-57.98</b>	<b>-59414.34</b>
Average	0.60	0.77	28.64	0.75	25.70	0.73	24.05
Outside Watershed Boundary							
Station ID	QPESUMS	RK	Imprv., %	Merging	Imprv., %	OK	Imprv., %
C1M630	0.69	0.74	7.56	0.77	11.31	0.66	-5.00
C1V170	0.44	0.57	30.48	0.54	24.06	0.42	-3.25
C1V460	0.59	0.63	7.62	0.54	-8.17	0.32	-45.66
1510P088	0.40	0.60	48.44	0.54	34.10	0.58	43.44
<b>1730P132</b>	<b>-0.25</b>	<b>0.13</b>	<b>153.63</b>	<b>0.19</b>	<b>177.06</b>	<b>0.44</b>	<b>277.77</b>
467530	0.24	0.48	102.85	0.45	88.53	0.31	29.47
467550	0.71	0.76	6.96	0.75	6.11	0.64	-9.67
C0I090	0.68	0.77	12.84	0.73	7.27	0.62	-9.94
C1I040	0.68	0.73	7.32	0.72	5.09	0.60	-11.76
C1I100	0.57	0.71	24.82	0.68	20.14	0.59	3.15
C1I120	0.55	0.43	-21.66	0.38	-30.44	-0.94	-271.17
C1I150	0.68	0.77	12.83	0.77	13.06	0.64	-6.63
C1I170	0.80	0.80	-0.35	0.75	-6.00	0.51	-36.08
C1I270	0.66	0.77	16.61	0.72	8.92	0.68	2.12
C1I310	0.52	0.81	56.59	0.79	52.52	0.77	48.15
Average	0.59	0.69	22.35	0.65	16.18	0.46	-19.49

**Table 7.9:** RMSE comparisons between RK, merging, and OK techniques for Typhoon Sinlaku.

Inside Watershed Boundary							
Station ID	QPESUMS	RK	Red., %	Merging	Red., %	OK	Red., %
1510P030	1.33	1.27	4.69	1.24	6.83	1.24	6.40
1510P087	1.31	0.73	44.32	0.75	42.32	0.84	35.91
C0H9A0	1.28	0.97	24.51	1.02	20.51	1.10	14.23
C1I060	1.29	0.72	43.99	0.78	39.44	0.93	27.75
C1I070	1.13	0.99	12.84	1.01	10.51	1.02	10.40
C1I080	1.08	0.82	23.65	0.81	24.72	1.01	5.73
C1I160	1.09	0.73	33.61	0.73	33.45	0.87	20.39
C1I290	1.02	0.75	26.76	0.74	27.15	0.82	19.83
C1I300	0.99	0.69	30.31	0.71	27.98	0.77	21.48
C1I340	1.16	0.99	14.60	1.02	12.54	1.04	10.61
C1I350	0.93	0.77	16.70	0.88	5.14	0.90	2.60
C1M440	1.15	0.93	18.84	0.96	16.10	1.03	10.56
Average	1.15	0.86	24.57	0.89	22.22	0.96	15.49
Outside Watershed Boundary							
Station ID	QPESUMS	RK	Red., %	Merging	Red., %	OK	Red., %
C1M630	1.54	1.47	4.48	1.49	3.18	2.39	-54.80
C1V170	1.01	0.94	6.88	1.01	0.28	1.18	-16.19
C1V460	1.43	1.38	3.49	1.42	0.99	1.55	-8.11
1510P088	1.15	0.92	20.32	0.92	20.39	0.94	18.71
1730P132	1.40	1.06	23.88	1.11	20.67	1.08	22.72
467530	1.91	1.58	17.64	1.60	16.56	1.79	6.41
467550	1.32	1.12	15.12	1.13	14.64	1.30	1.75
C0I090	1.19	1.00	16.31	1.01	15.33	1.21	-1.36
C1I040	1.32	1.34	-1.61	1.44	-9.25	2.13	-60.87
<b>C1I100</b>	<b>0.65</b>	<b>0.84</b>	<b>-29.10</b>	<b>0.85</b>	<b>-30.66</b>	<b>1.69</b>	<b>-160.68</b>
C1I120	0.93	0.88	5.86	0.93	-0.42	1.18	-26.62
C1I150	1.24	1.06	14.30	1.06	14.86	1.28	-3.57
C1I170	1.29	1.18	8.34	1.20	7.25	1.35	-4.40
C1I270	1.42	1.11	21.76	1.10	22.64	1.25	12.15
C1I310	1.13	0.70	38.16	0.68	39.78	0.75	33.61
Average	1.31	1.13	13.92	1.15	11.92	1.38	-5.75

**Table 7.10:** CE comparisons between RK, merging, and OK techniques for Typhoon Sinlaku.

Inside Watershed Boundary							
Station ID	QPESUMS	RK	Imprv., %	Merging	Imprv., %	OK	Imprv., %
1510P030	0.50	0.65	30.00	0.53	6.00	0.55	10.00
1510P087	0.60	0.87	46.61	0.87	45.08	0.83	39.81
C0H9A0	0.68	0.82	20.34	0.80	17.40	0.76	12.50
C1I060	0.63	0.88	40.01	0.86	36.91	0.81	27.87
C1I070	0.40	0.54	35.94	0.52	29.77	0.52	29.49
C1I080	0.68	0.82	19.19	0.82	19.94	0.72	5.12
C1I160	0.66	0.85	29.42	0.85	29.31	0.78	19.27
C1I290	0.61	0.79	29.75	0.79	30.12	0.75	22.93
C1I300	0.65	0.83	27.79	0.82	26.01	0.78	20.72
C1I340	0.61	0.72	17.23	0.70	14.97	0.69	12.80
C1I350	0.51	0.66	29.47	0.56	9.64	0.53	4.94
C1M440	0.55	0.71	27.47	0.69	23.83	0.64	16.11
Average	0.59	0.76	29.43	0.73	24.08	0.70	18.46
Outside Watershed Boundary							
Station ID	QPESUMS	RK	Imprv., %	Merging	Imprv., %	OK	Imprv., %
C1M630	0.72	0.74	3.45	0.74	2.46	0.32	-55.02
C1V170	0.52	0.59	12.06	0.53	0.50	0.36	-31.75
C1V460	0.48	0.52	7.42	0.49	2.14	0.39	-18.26
1510P088	0.63	0.76	21.48	0.77	21.55	0.76	19.96
1730P132	0.53	0.73	36.71	0.71	32.37	0.72	35.17
467530	0.48	0.65	35.30	0.64	33.34	0.54	13.61
467550	0.51	0.65	26.69	0.64	25.92	0.53	3.32
C0I090	0.69	0.78	13.43	0.78	12.68	0.68	-1.23
C1I040	0.74	0.73	-1.13	0.69	-6.78	0.33	-55.60
<b>C1I100</b>	<b>0.42</b>	<b>0.04</b>	<b>-90.91</b>	<b>0.02</b>	<b>-96.43</b>	<b>-2.92</b>	<b>-790.34</b>
C1I120	0.74	0.77	4.05	0.74	-0.30	0.58	-21.49
C1I150	0.63	0.73	15.64	0.73	16.21	0.60	-4.28
C1I170	0.53	0.60	14.34	0.59	12.54	0.48	-8.06
C1I270	0.65	0.79	20.86	0.79	21.60	0.73	12.28
C1I310	0.69	0.88	27.76	0.89	28.64	0.86	25.13
Average	0.61	0.71	17.00	0.69	14.49	0.56	-6.16

**Table 7.11:** RMSE comparisons between RK, merging, and OK techniques for Typhoon Fanapi.

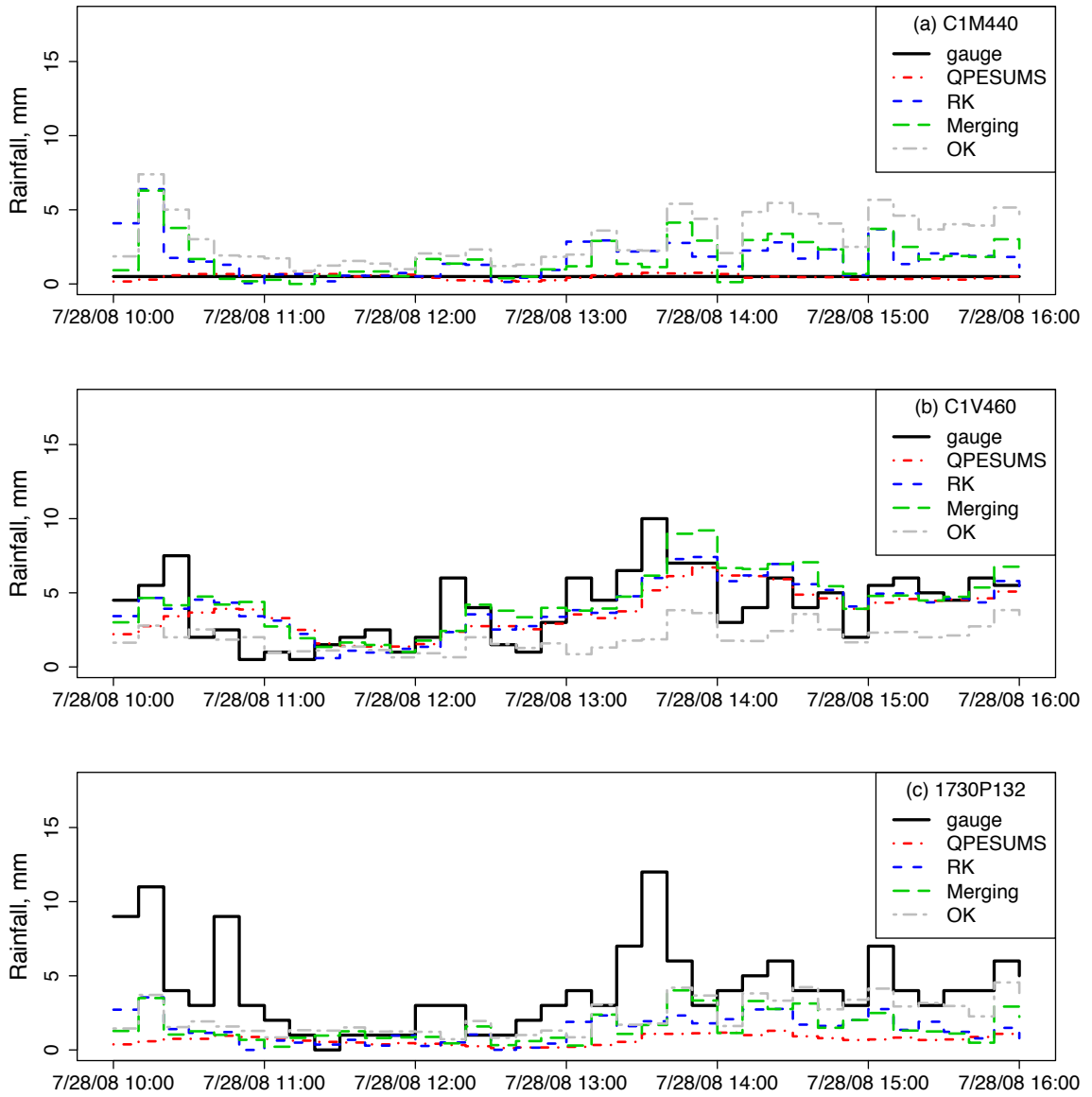
Inside Watershed Boundary							
Station ID	QPESUMS	RK	Red., %	Merging	Red., %	OK	Red., %
1510P030	0.98	0.81	17.29	0.75	24.25	0.72	26.41
1510P087	1.10	0.56	48.64	0.52	52.55	0.67	38.81
C0H9A0	0.57	0.47	18.48	0.56	2.07	0.62	-7.69
C1I060	1.24	0.76	38.77	0.89	28.61	1.26	-1.16
<b>C1I070</b>	<b>1.29</b>	<b>1.34</b>	<b>-4.12</b>	<b>1.24</b>	<b>4.04</b>	<b>1.06</b>	<b>17.85</b>
C1I080	0.69	0.65	5.91	0.64	8.34	0.73	-5.43
C1I160	0.34	0.35	-4.20	0.49	-42.78	0.72	-111.72
C1I290	0.62	0.47	23.30	0.61	0.94	0.58	5.65
C1I300	0.39	0.42	-9.53	0.57	-46.43	0.70	-79.97
C1I340	0.51	0.45	11.36	0.48	5.68	0.43	15.23
C1I350	0.67	0.42	37.32	0.44	34.00	0.48	28.29
C1M440	0.69	0.61	11.92	0.69	0.82	0.94	-35.77
Average	0.76	0.61	18.12	0.65	6.19	0.74	-11.58

Outside Watershed Boundary							
Station ID	QPESUMS	RK	Red., %	Merging	Red., %	OK	Red., %
C1M630	0.74	0.71	3.19	0.76	-2.81	0.85	-15.56
C1V170	1.10	0.95	13.31	1.05	4.20	1.18	-7.08
C1V460	0.89	0.78	12.83	0.77	13.69	0.89	-0.18
1510P088	1.43	1.30	9.22	1.19	16.98	1.12	21.80
1730P132	NA	NA	NA	NA	NA	NA	NA
467530	1.16	0.98	16.19	1.02	12.78	1.47	-26.06
467550	0.93	0.78	16.05	0.87	6.32	1.08	-16.12
C0I090	0.51	0.47	8.39	0.53	-4.52	0.66	-29.60
C1I040	0.64	0.63	0.62	0.65	-1.58	0.73	-15.26
C1I100	0.47	0.44	6.93	0.46	2.45	0.48	-0.78
C1I120	0.44	0.44	0.81	0.47	-6.09	0.77	-72.16
C1I150	0.52	0.52	1.28	0.50	3.58	0.76	-45.76
C1I170	0.24	0.30	-20.95	0.35	-43.23	0.84	-244.30
C1I270	0.40	0.41	-3.93	0.49	-24.02	0.62	-56.15
C1I310	0.53	0.39	25.79	0.38	28.55	0.40	23.55
Average	0.72	0.65	6.41	0.68	0.45	0.85	-34.55

**Table 7.12:** CE comparisons between RK, merging, and OK techniques for Typhoon Fanapi.

Inside Watershed Boundary							
Station ID	QPESUMS	RK	Imprv., %	Merging	Imprv., %	OK	Imprv., %
1510P030	0.59	0.72	21.85	0.77	29.47	0.78	31.70
1510P087	0.80	0.95	18.45	0.95	19.42	0.92	15.67
C0H9A0	0.70	0.80	14.48	0.71	1.77	0.65	-6.89
C1I060	0.79	0.92	16.40	0.89	12.86	0.79	-0.61
<b>C1I070</b>	<b>-2.99</b>	<b>-3.33</b>	<b>-11.22</b>	<b>-2.67</b>	<b>10.57</b>	<b>-1.69</b>	<b>43.39</b>
C1I080	0.57	0.62	8.72	0.64	12.15	0.52	-8.48
C1I160	0.49	0.44	-9.05	-0.05	-109.68	-1.30	-367.70
C1I290	0.68	0.81	19.82	0.68	0.90	0.71	5.29
C1I300	0.47	0.36	-22.81	-0.14	-130.75	-0.73	-255.85
C1I340	0.56	0.66	16.56	0.61	8.54	0.69	21.75
C1I350	0.64	0.86	34.17	0.84	31.76	0.81	27.34
C1M440	0.80	0.84	5.63	0.80	0.41	0.63	-21.19
Average	0.64	0.73	11.29	0.61	-11.20	0.41	-50.81
Outside Watershed Boundary							
Station ID	QPESUMS	RK	Imprv., %	Merging	Imprv., %	OK	Imprv., %
C1M630	0.66	0.68	3.23	0.64	-2.94	0.55	-17.28
C1V170	0.72	0.79	9.74	0.74	3.23	0.68	-5.74
C1V460	0.75	0.81	8.08	0.81	8.58	0.75	-0.12
1510P088	0.29	0.42	42.29	0.51	74.74	0.57	93.43
1730P132	NA	NA	NA	NA	NA	NA	NA
467530	0.68	0.78	13.97	0.76	11.23	0.49	-27.66
467550	0.80	0.86	7.51	0.82	3.11	0.73	-8.86
C0I090	0.48	0.57	17.16	0.44	-9.86	0.13	-72.49
C1I040	0.71	0.71	0.51	0.70	-1.32	0.61	-13.57
C1I100	0.69	0.73	6.04	0.70	2.19	0.68	-0.71
C1I120	0.44	0.45	2.05	0.37	-15.87	-0.66	-248.50
C1I150	0.55	0.56	2.11	0.58	5.87	0.03	-93.85
<b>C1I170</b>	<b>0.36</b>	<b>0.07</b>	<b>-80.73</b>	<b>-0.30</b>	<b>-183.37</b>	<b>-6.53</b>	<b>-1892.64</b>
C1I270	0.53	0.50	-6.99	0.28	-46.94	-0.14	-125.47
C1I310	0.52	0.74	40.90	0.76	44.55	0.72	37.82
Average	0.60	0.66	11.28	0.62	5.89	0.40	-37.15



**Figure 7.10:** Peak hour hyetograph comparisons for interpolation error investigation, Typhoon Fungwong.

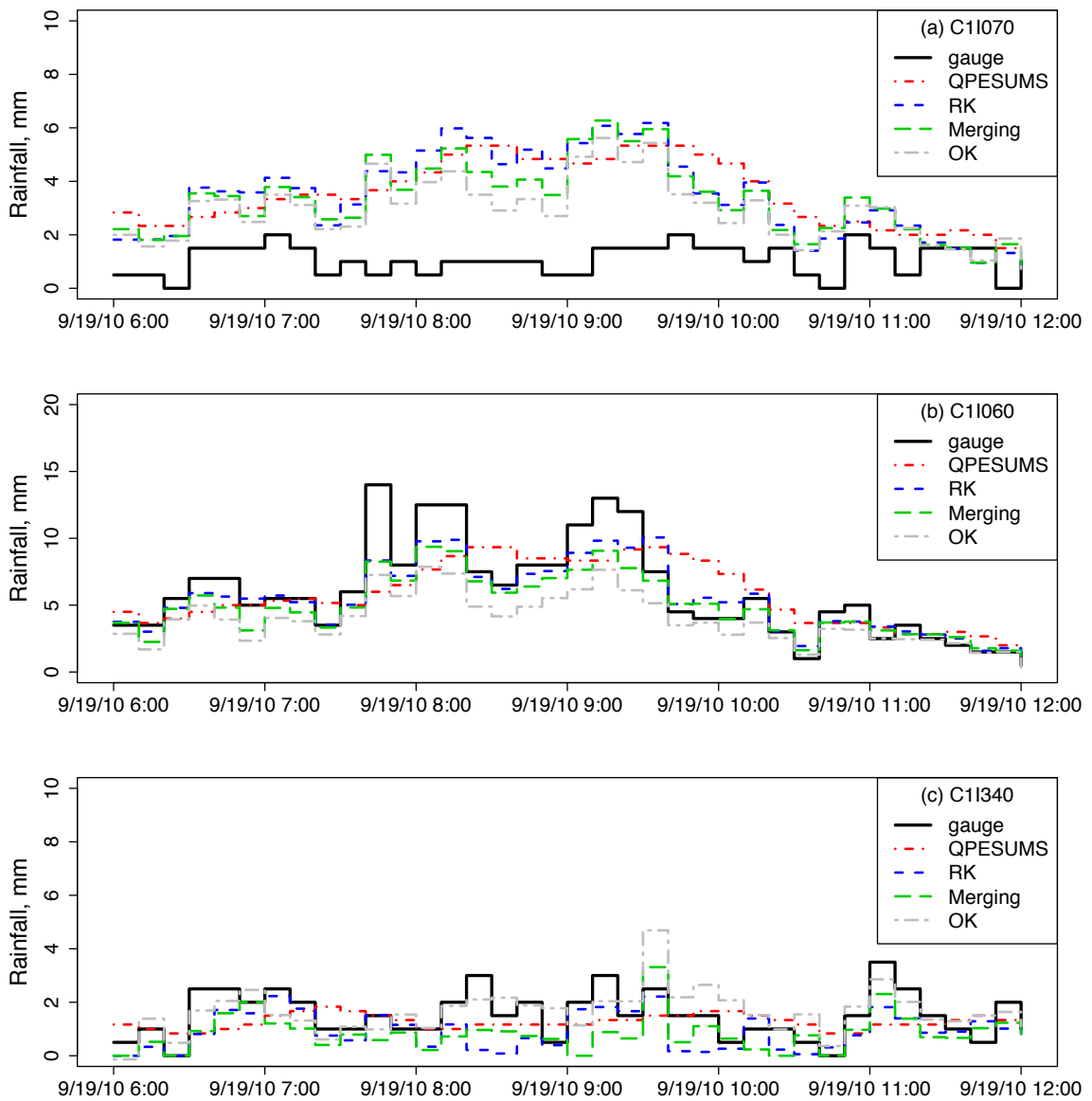


**Figure 7.11:** Peak hour hyetograph comparisons for interpolation error investigation, Typhoon Fanapi.

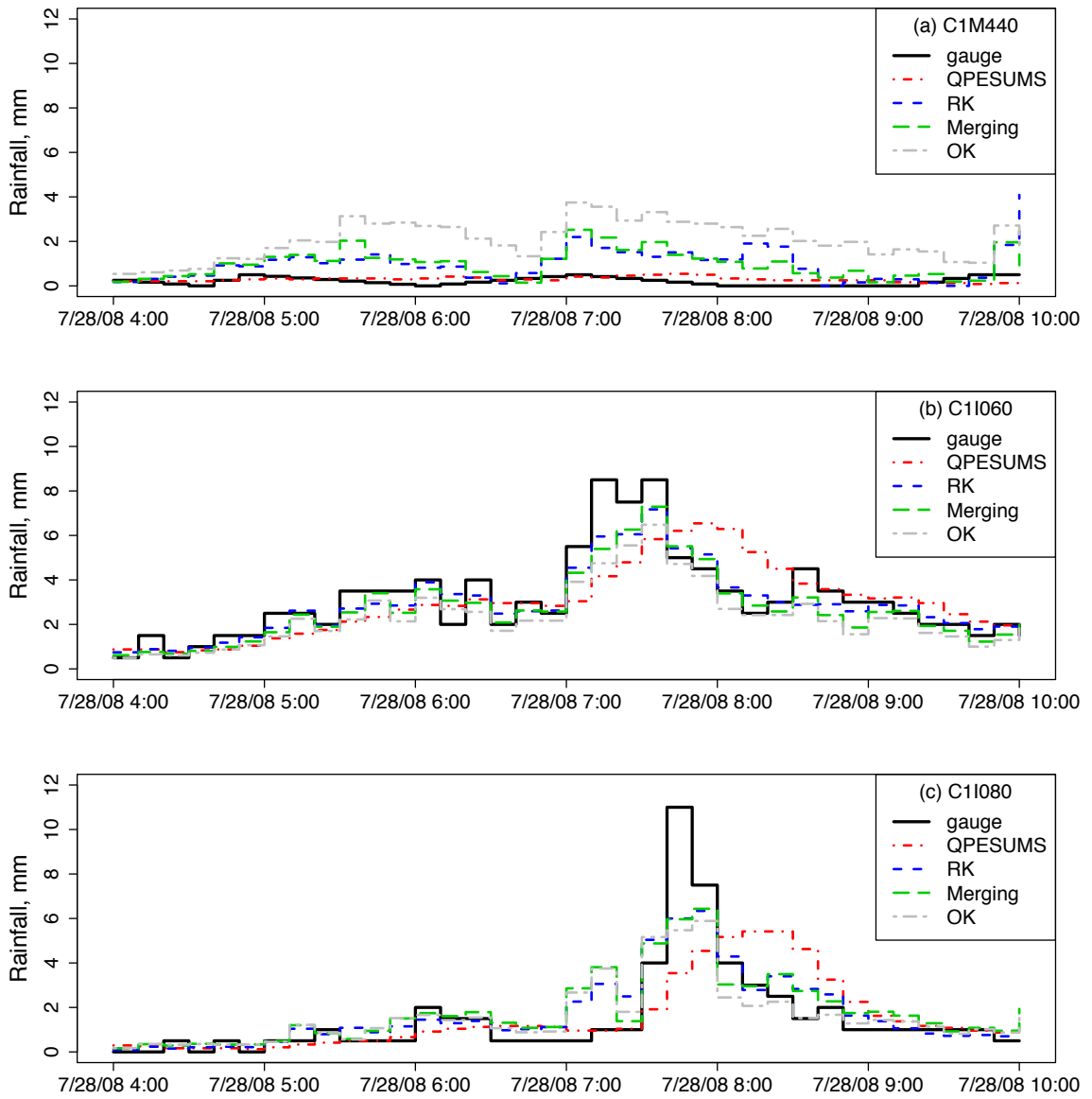


**Figure 7.12:** Peak hour hyetograph comparisons, Typhoon Fungwong.

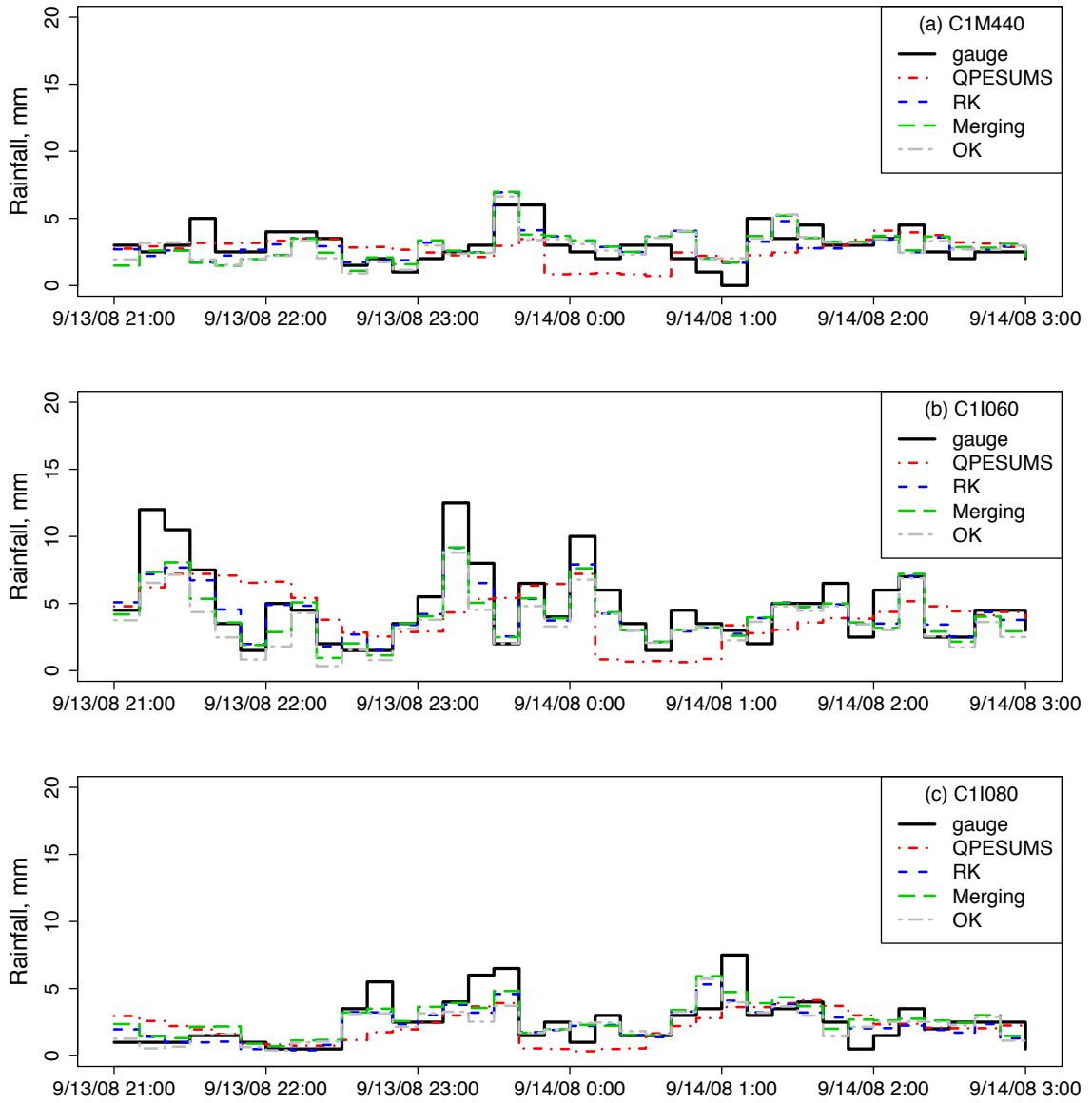


**Figure 7.13:** Peak hour hyetograph comparisons, Typhoon Sinlaku.

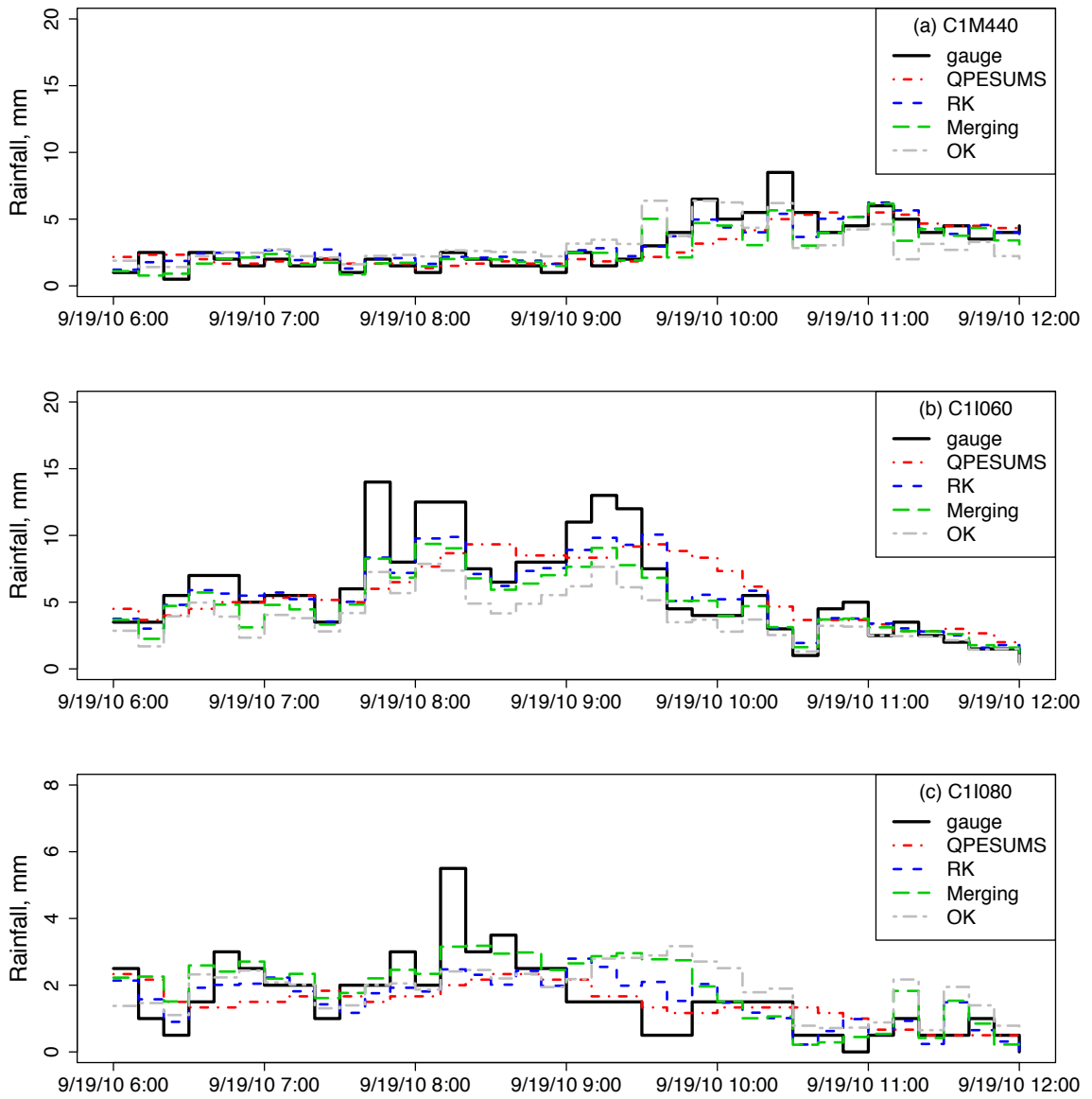


Figure 7.14: Peak hour hyetograph comparisons, Typhoon Fanapi.

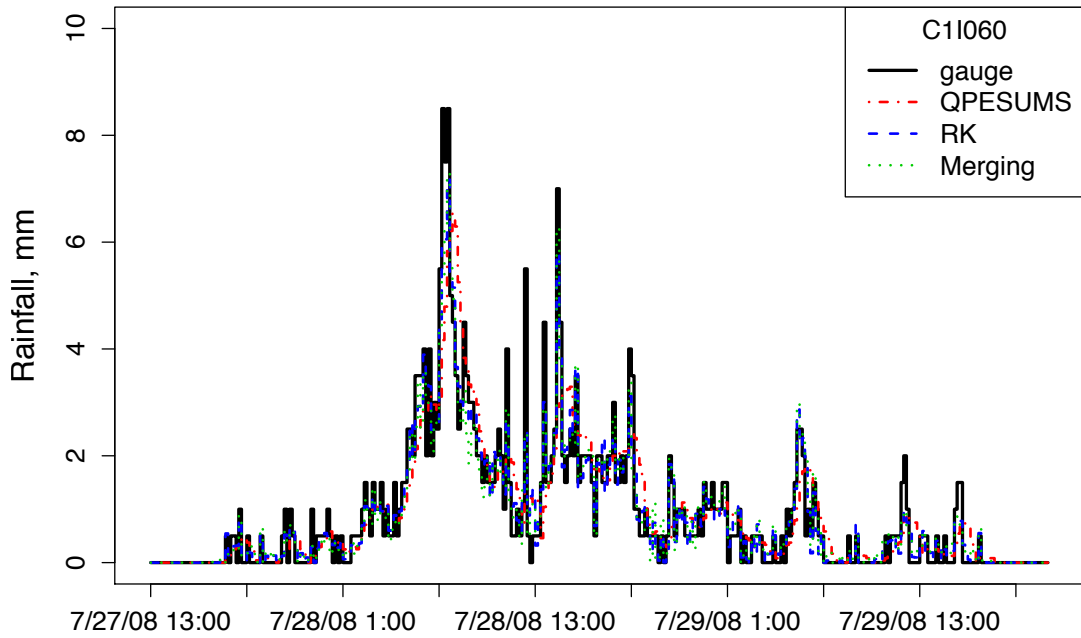


Figure 7.15: Full event hyetograph comparisons at station C1I060, Typhoon Fungwong.

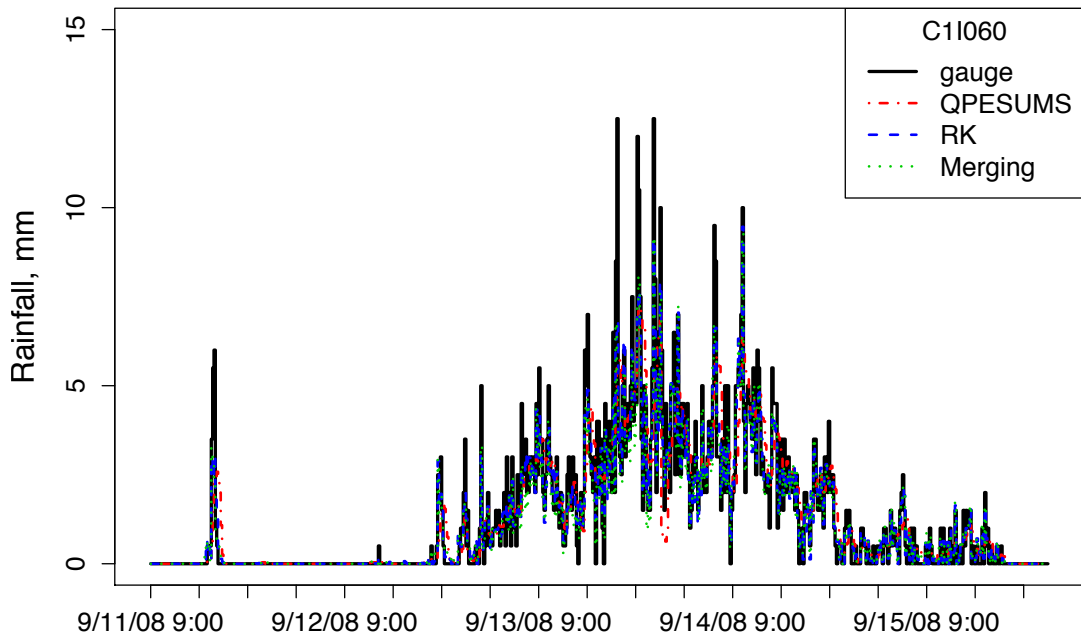


Figure 7.16: Full event hyetograph comparisons at station C1I060, Typhoon Sinlaku.

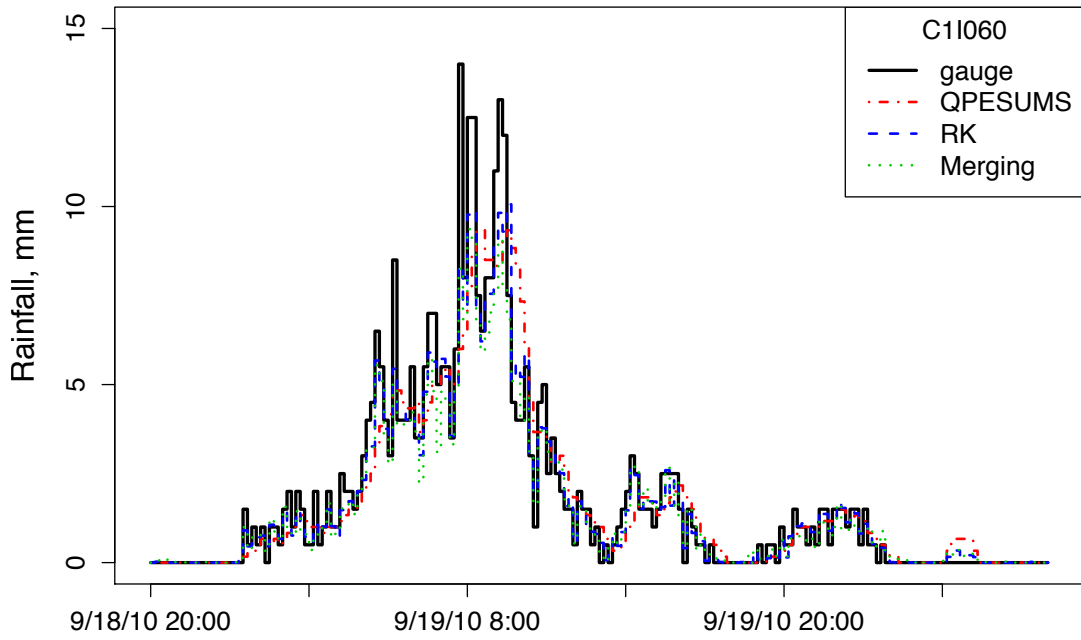


Figure 7.17: Full event hyetograph comparisons at station C1I060, Typhoon Fanapi.

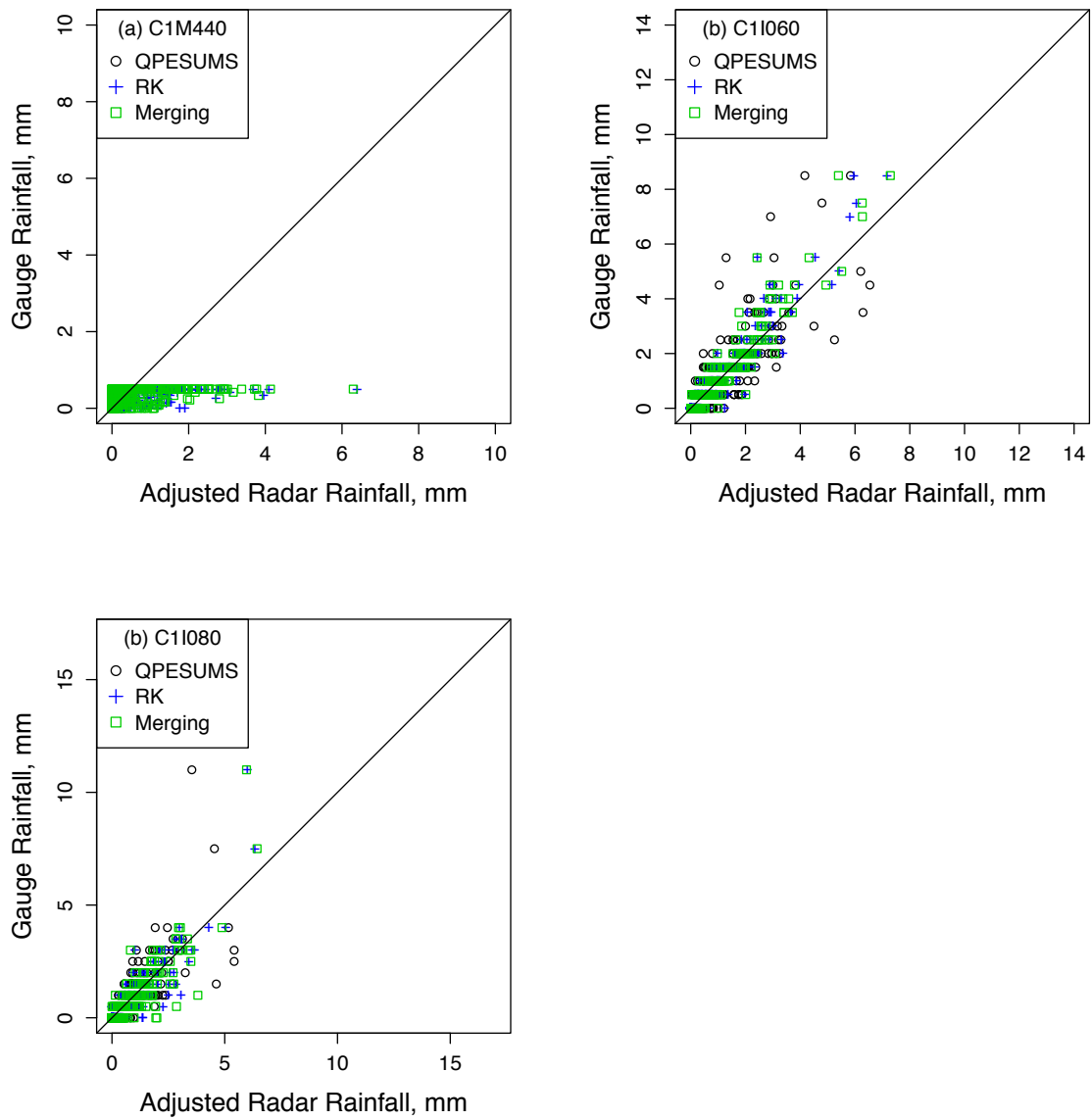


Figure 7.18: Adjusted radar rainfall v.s. gauge observations, Typhoon Fungwong.

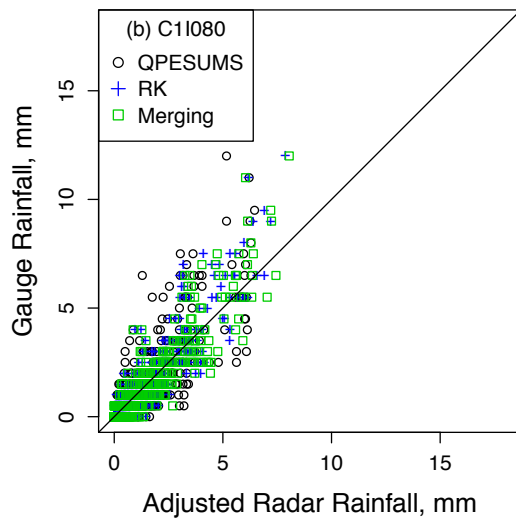
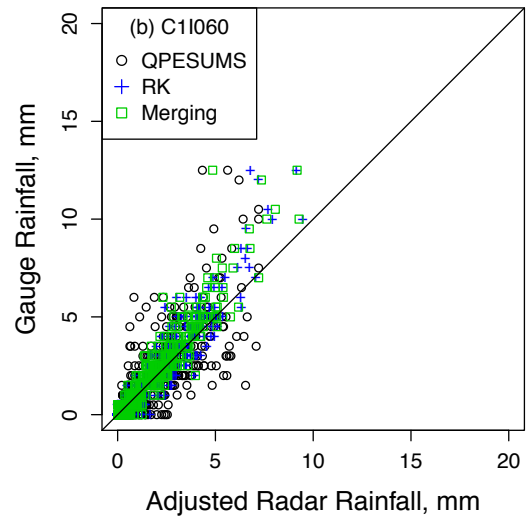
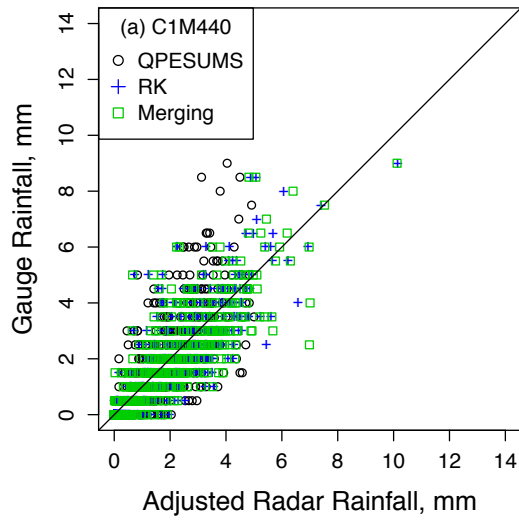


Figure 7.19: Adjusted radar rainfall v.s. gauge observations, Typhoon Sinlaku.

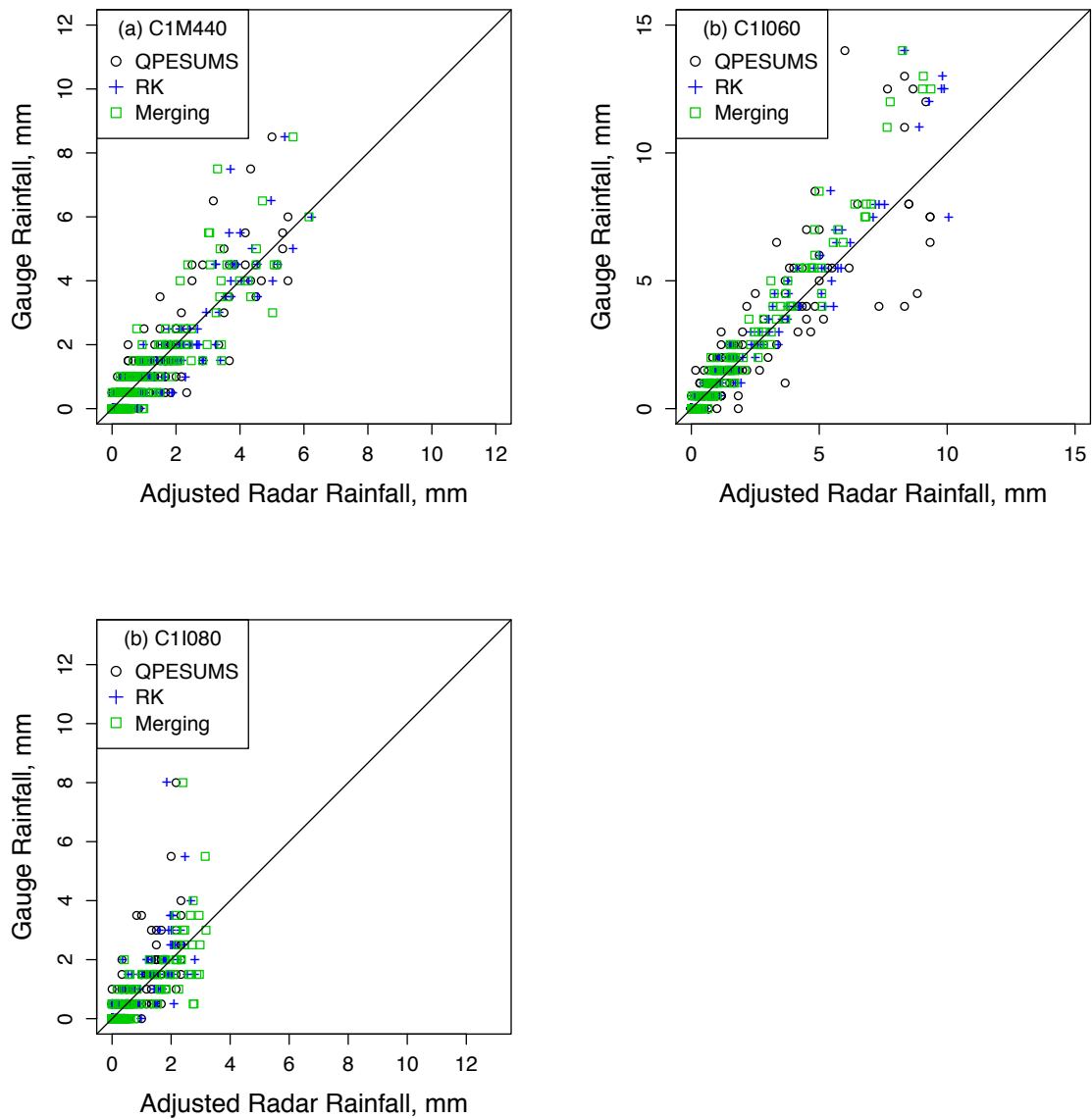


Figure 7.20: Adjusted radar rainfall v.s. gauge observations, Typhoon Fanapi.

## Chapter 8

### Conclusions and Future Studies

In this part of the research, two algorithms based on the regression-kriging (RK) and merging spatial interpolation techniques were developed to interpolate rain fields using radar estimates and gauge observations for the Chenyulan River watershed in Taiwan. Both of the techniques are multivariate through which the prediction of rainfall is made by using the gauge observations together with the correlated auxiliary variables, radar estimates in this case, as secondary predictors such that the accuracy of the prediction could be improved, especially when the sampling conditions are inadequate. The geostatistically based algorithms developed in this study were written in R, a statistical programming language, and the interpolation process could be automated with the execution of the batch scripts that were written for various tasks, such as synchronizing rainfall data between the ftp server and local database. Five historical typhoons, Typhoons Kalmaegi, Morakot, Fungwong, Sinlaku, and Fanapi, were selected as test events. The interpolated rainfall values by the two techniques were cross validated with the gauge measurements and compared to the interpolated results from the ordinary kriging (OK) method, a univariate technique. The comparisons were analyzed from three different aspects (error analysis, time series, and data scattering along the 45-degree reference line). Based on the results, it was clearly shown that both of the RK and merging methods could effectively produce reliable rainfall data covering the study watershed. In addition, the RK and merging methods were demonstrated to outperform the univariate OK method. For future studies, it is suggested to perform the semivariogram modeling based on the true distances (3-D) between the gauge stations as opposed to the commonly used projected (2-D) distances so that the effect of elevation change may be realistically reflected. In this study, inadequate sampling conditions might have impacted the results of the interpolation. The developed algorithms can be of use to optimize the existing gauge network covering the study watershed and improve the sampling

quality by proposing additional gauges and the ideal locations.

## Part II

### ENERGY DISSIPATION IN FLUID FLOWS AND WAVE TRANSFORMATION BY POROUS BARRIERS AND SUBMERGED CAVITIES

## Chapter 9

### Introduction

Porous media have had a long history of being included in general hydraulics as well as coastal engineering designs. The main functions of these porous devices include preventing foreign objects from entering restricted fluid domains and attenuating unwanted wave motion in protected water bodies. Figure 9.1 shows a mechanical bar screen system at the inlet of a wastewater treatment plant. Solid waste was being removed from the incoming waste stream. The porous breakwater in Figure 9.2 is composed of numerous tetrapods. It is used to reflect and dissipate the impinging wave energy such that the sheltered region maintains its calmness.



**Figure 9.1:** Inlet bar screen system of a wastewater treatment plant, photo courtesy of <http://kusterszima.com>.

As a fluid passes through a porous medium, such as the mechanical bar screen system at the inlet of a wastewater treatment plant, energy loss or commonly termed as head loss will be unpreventable. In many hydraulic designs that are gravity driven, engineers are often required to perform detailed computation on head loss to ensure that sufficient head is



**Figure 9.2:** Porous breakwater, photo courtesy of <http://cdn.physorg.com>.

provided for the gravity flow to occur. For instance, when designing a wastewater treatment plant, adequate head must be present for the waste stream to flow through the entire treatment process. Pump systems will be needed where head is insufficient. In addition, predictable head loss induced by the inlet bar screen system can help in determining the water surface level (flow backup) in the upstream channel such that the risk of the incoming waste stream overtopping the channel banks can be closely monitored. This part of the research focused on the experimental investigation of head loss associated with fluids flowing through porous screens under various flow rate conditions. The effects of screen material properties such as pore size, porosity, and angle of inclination on head loss were studied. Empirical formulas, which can be of use to predict head loss based on given flow conditions, were also developed. The findings of this experimental study could potentially be applied to the determination of head loss generated by the inlet bar screen system of a wastewater treatment plant or other hydraulic systems.

Porous breakwaters and seawalls have been traditionally built as wave energy absorbers to provide protection to ports and harbors as well as coastal infrastructures. Although a variety of designs of porous breakwaters has been proposed and field tested, the transformation of water waves including reflection and transmission by porous structures remains an active research topic. This study is intended to extend the work of Chwang (1983) and

Chwang and Chan (1998). In their work, small-amplitude gravity waves generated by a horizontally oscillating porous plate on water of a constant finite depth were analyzed. It was shown that the total load exerted on the porous plate and the amplitude of the generated waves were reduced as the porous effect, represented as the porous effect parameter  $G_0$ , of the plate increased. Their porous wave maker study later on evolved to the investigation of water waves moving past a porous structure, and Darcy's law was adopted as a boundary condition to interlink the wave motions on both sides of the structure. Analytical solutions based on the potential flow theory for the reflection and transmission of the waves were derived. A porous effect parameter was introduced as part of the mathematical formulation. The main goal of this study was to conduct experimental tests to validate the use of Darcy's law and the derived solutions. A lab scale piston-type wave maker, which could generate waves of different types, was designed and built on a flume. Small-amplitude waves were propagated through porous screens of varying pore sizes and porosities. The coefficients of transmission were determined by analyzing the recorded test results.

In addition to the aforementioned tests focusing on the fluid-porous screen interaction that were carried out for this research work, an experimental investigation of solitary wave induced fluid motions within the domain of a submerged trench was conducted. As waves propagating past a trench or a region of uneven water depth, the interaction process and induced fluid motions are known to cause transformation of the incident waves as well as the entrainment of fluid contents from a region of deeper water depth to shallower water depth. These hydrodynamic and environmental impacts on the natural or engineered systems are important to the management of coastal projects. For example, the plankton, natural nutrients, sediments, or contaminated materials that are settled in a submerged trench are frequently disturbed by wave motions. The transport of the trapped materials from the trench may alter the surrounding ecological system. For the cases related to sediment transport, the induced vortex can also intensify the drift of sand to affect the navigational conditions of waterways. In order to conduct the tests, a trench was built in the flume by placing two up-leveled acrylic panels with a gap of changeable opening size in between. Solitary waves with different wave heights were generated by the wave maker and propagated over the trench zone. Three resistance-typed wave gauges were placed along the flume to

record the wave profiles. The Planar Laser Induced Fluorescence (PLIF) technique, which excites and illuminates the molecules of a fluorescent dyed moving fluid, was utilized to visualize the evolution of the induced vortices and to study the flow patterns as a solitary wave moved past the trench zone. Each test was recorded with a video camera, and all the image frames were further processed such that the transformation of the wave, induced vortices, trajectories of fluid particles, and entrained distance could be compared with the simulated results obtained from a two-dimensional (2-D) viscous flow model at selected instants of interest.

## Chapter 10

### Literature Review

Porous screens are commonly used as devices for preventing foreign objects from entering restricted fluid domains. For instance, bar screen systems can be seen at the inlets of wastewater treatment plants. The systems capture and remove coarse solid waste from the incoming waste stream. Removing debris from the intakes of power plant cooling systems and diverting fish from entering the turbines of power generating facilities are just two more applications (Ho, Coonrod, Hanna, & Mefford, 2011; Yeh & Shrestha, 1989). When a flow passes through a porous screen, the partial blockage of the approaching flow results in back-up at the upstream side of the screen. Energy loss, commonly termed as head loss, which is caused by fluid contraction, friction, induced turbulence, and other factors associated with the flow being forced through the pores of the screen, is another important phenomenon (Florie & Hoek, 1981). It has become a very common practice for engineers to take back-up and head loss into consideration when designing screen systems for the applications stated above. Known head loss information can also be used to develop reliable boundary conditions on the surfaces of a porous screen, which will be included in the development of analytical or numerical models for simulating flows passing through porous screens (Ho et al., 2011).

In the past decade or two, only limited studies have been carried out, either experimentally or analytically, to incorporate flow characteristics and the physical parameters of screens to estimate head loss. The head loss for a fluid flow passing through a wedge wire screen was studied experimentally by Yeh and Shrestha (1989). It was found that the head loss could be minimized if the screen was positioned at the optimal angle of inclination. A summary study for air flowing through screens was presented by Laws and Livesey (1978). The effects of porous screens on the flow velocity distribution was investigated. Wang (2004) conducted a series of extensive tests to measure head loss associated with the inlet screening

systems used in wastewater treatment plants. The screens which were tested included bar screens with various bar spacing, perforated screens of different pore sizes, stepped screens and more. From the previous work of Santiago, Chu, and Wang (2007), it was suggested that head loss was affected greatly by the screen's porosity as compared to the pore size. A three-dimensional numerical model solving the Reynolds-averaged Navier-Stokes equations was used by Ho et al. (2011) to simulate the flow pattern changes due to fish screen systems. The head loss coefficients were simulated and compared with experimental measurements.

For coastal engineering applications, porous structures such as breakwaters or seawalls have been traditionally constructed to reduce wave height and dissipate wave energy. One of the earliest studies about wave attenuation by porous media in modern history of coastal hydrodynamics was conducted by Chwang (1983). Small-amplitude gravity waves generated by a horizontally oscillating porous plate near the end of a semi-infinitely long open channel of constant water depth were analyzed. The phenomenon of wave trapping, termed by Chwang, was observed if specific ratios of the space between the porous plate and end plate of the channel to the wavelength of the propagating waves were reached. Later on, the use of Darcy's law, which suggests that the flow velocity of a fluid passing through a porous medium is linearly proportional to the pressure drop between the entering and exiting surfaces, for modeling waves propagating past porous plates was assessed by Evans (1990), Chwang and Chan (1998), and Cho and Kim (2008). In addition to the analytical derivation of solutions, Cho and Kim (2008) conducted experiments to test the effects of material properties such as porosity and angle of inclination on wave absorbing efficiency in a wave tank as well as a large scale 2-D wave basin.

Various designs of porous breakwaters as wave dampers for port and harbor protection have been evaluated extensively (Chwang & Chan, 1998; Yip & Chwang, 2000). A great amount of attention was placed on the wave transformation including both reflection and transmission caused by breakwaters. Madsen (1983) and Huang and Chao (1992) proposed theoretical solutions for the reflection and transmission of linear waves from vertical porous walls. A theoretical study of the wave transformation caused by a thin flexible porous breakwater was conducted by Wang and Ren (1993). The effects of physical variables such as the rigidity and porosity of the breakwater on the efficiency of wave damping were

evaluated. Dalrymple, Losada, and Martin (1991) derived analytical solutions for the wave reflection and transmission from porous structures when impinging by oblique waves. More recently, the application of porous structures as wave absorbers was extended to the offshore engineering designs. It has become increasingly popular to surround coastal or offshore main support structures with cylindrical concentric porous walls, such that the large wave force can be prevented from encountering on the interior solid structure (Darwiche, Williams, & Wang, 1994; Wang & Ren, 1994; Zhong & Wang, 2006).

As previously introduced, the hydrodynamic and environmental impacts on natural or engineered systems caused by water waves propagating over a region of uneven water depth are crucial to the management of coastal projects. When a long-wavelength solitary wave propagates over a rectangular trench, the top fluid layer of the trench (functioned as trench lid) is driven by a time varying, but nearly uniform, velocity distribution across the trench. Similar to the moving lid problem (Chen, Naseri-Neshat, & Ho, 1981; Goda, 1979; Hu & Wang, 2004; Iwatsu, Ishii, Kawamura, Kuwahara, & Hyun, 1989), vortical flows can be generated within the trench to potentially remove the fluid contents to the surrounding area. The kinematics of wave motions are variables of interest for estimating the degree of horizontal mixing in the surf zone (Longuet-Higgins, 1981). Pritchard and Hogg (2003) employed the shallow-water equations for the velocity calculation to model the suspended sediment transport, erosion, and deposition under reflected long waves on a plane beach. In the environment of wave action, understanding the trajectories of fluid particles moving in the water column, especially near the bottom of the fluid domain, can assist the analyses of the flow-field, transport phenomenon, and sediment drift behavior. Based on the classical linear water wave theory, the orbital trajectories of particles are in closed loops with a circular motion in deep water and an elliptic path in a shallow water depth. However, Constantin and Villari (2008) showed that no exactly closed particle trajectory was found in a linear water wave. In 1847, Stokes, who initiated the higher order Stokes waves, found the particle trajectories were apparently not closed due to the effect of nonlinearity. The movement of fluid particles on the channel bottom due to the passage of a solitary wave was investigated by Price (1971). Fenton (1972) extended Grimshaw's theory (Grimshaw, 1971) to give the ninth-order solution of the drift velocities of fluid particles for a solitary wave. A

review article on solitary-wave theory reported by Sander and Hutter (1991) presented the results of path lines of a solitary wave. Longuet-Higgins (1981) examined the total surface drift of solitary waves of maximum amplitude by both theoretical and experimental analyses. The above described studies on wave induced trajectories of fluid particles, however, are limited to the regions with a constant water depth or the cases with a horizontal bottom. When the fluid domain includes the conditions of uneven water depth (e.g., the cases with a trench), the fluid particle motions under wave action are expected to become more complex. Additional appearances of vortices around a trench after the passing over of a solitary wave were reported by Chang et al. (2011) using their two-dimensional (2-D) viscous flow model. Other issues related to the damping effect on approaching waves and the induced dynamic response with fluid mud in trench were presented by Ting (1994).

## Chapter 11

### Theoretical Background

#### 11.1 HEAD LOSS

In order to study the relationships between head loss, porosity, pore size, and angle of inclination, screens with two different pore sizes (diameters of 1/4 and 1/8 inches) and four porosities (16.08%, 22.67%, 29.61%, and 40.31%) were selected for testing. Before introducing the experimental setup and how the measurements were taken, it is a good idea to go over some key equations that were used in the study. Figure 11.1 shows a schematic diagram of a fluid flowing through a porous screen. The fluid is bounded horizontally by the flume floor and the free surface. The upstream uniform depth is represented by  $Y_1$ .  $Y_2$  represents the downstream uniform depth. The screen obstructing the flow is positioned at an angle of inclination,  $\theta$ .

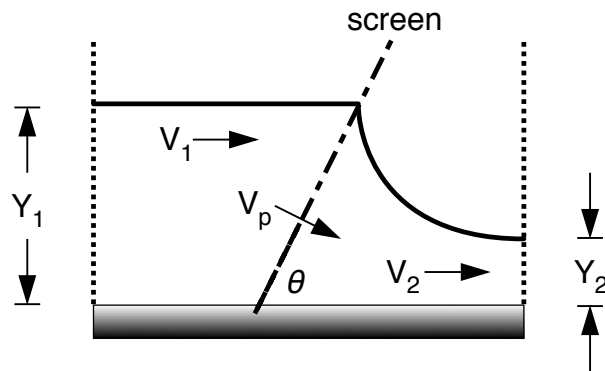


**Figure 11.1:** Profile view of fluid domain.

The energy equation across the porous screen is given as

$$Y_1 + \frac{V_1^2}{2g} + Z_1 = Y_2 + \frac{V_2^2}{2g} + Z_2 + \Delta h, \quad (11.1)$$

where  $V_1$  and  $V_2$  are the averaged flow velocities for the upstream and downstream cross sections, respectively. Assuming the flume floor is perfectly horizontal ( $Z_1 = Z_2$ ), the head

loss through the screen can then be determined as

$$\Delta h = (Y_1 - Y_2) + \left( \frac{V_1^2}{2g} - \frac{V_2^2}{2g} \right). \quad (11.2)$$

The continuity equation for a constant flow rate condition is expressed as

$$Q = V_1 A_1 = V_p A_p = V_2 A_2, \quad (11.3)$$

where  $Q$  is flow rate,  $A_1$  and  $A_2$  are the flow areas for the upstream and downstream cross sections, respectively, and  $A_p$  is the total opening area of the screen. In addition to  $V_1$  and  $V_2$ , the averaged pore velocity,  $V_p$ , is another important variable that may be correlated to head loss. The ratio of the opening area provided by the pores to the total area of a given screen is known as porosity which is defined as

$$\Phi = \frac{A_p \sin \theta}{A_1}. \quad (11.4)$$

With known porosity,  $\Phi$ , upstream averaged flow velocity,  $V_1$ , and angle of inclination,  $\theta$ , the averaged pore velocity can be determined as

$$V_p = \frac{V_1 \sin \theta}{\Phi}. \quad (11.5)$$

## 11.2 WAVE TRANSFORMATION CAUSED BY A VERTICALLY PLACED POROUS BARRIER

The derivation of the solutions for the propagation and transmission of a monochromatic wave by a porous barrier (porous screen) starts with the definition of the fluid domain as shown in Figure 11.2. The porous barrier is fixed vertically at the  $x = 0$  plane on a horizontal bottom surface. The undisturbed mean free surface with a finite depth,  $h$ , is positioned at the  $z = 0$  plane. Regions 1 and 2 refer to the domains  $x \leq 0$  and  $x \geq 0$ , respectively.

Assuming that the fluid is inviscid, incompressible, and motion irrotational, the velocity field of the fluid in the  $x$ - $z$  2-D domain can be represented by the gradient of the velocity potential,  $\phi(x, z, t)$  where  $t$  denotes time, which is a continuous scalar function in Cartesian

coordinates. The velocity at any location within the fluid domain is expressed as  $\mathbf{u} = (u, w) = (\frac{\partial\phi}{\partial x}, \frac{\partial\phi}{\partial z})$  where  $u$  and  $w$  are the velocity components in the  $x$  and  $z$  directions, respectively. The velocity potentials in region 1 and region 2 (Figure 11.2) satisfy Laplace equation by mass conservation as

$$\nabla^2 \phi_j = 0, \quad j = 1, 2, \quad (11.6)$$

where the subscripts 1 and 2 refer to regions 1 and 2, and  $\nabla^2$  is the 2-D Laplace operator. The velocity potentials for the incident, reflected, and transmitted wave motions are represented by  $\phi_I$ ,  $\phi_R$ , and  $\phi_T$  where  $\phi_I$  and  $\phi_T$  are right-going and  $\phi_R$  is left-going. The evanescent waves in region 1 and region 2, or sometimes referred as local disturbances, which are formed near both front and back surfaces of the porous barrier and show a decaying behavior as the distance from the barrier increases are represented by  $\phi_{E1}$  and  $\phi_{E2}$ , respectively.

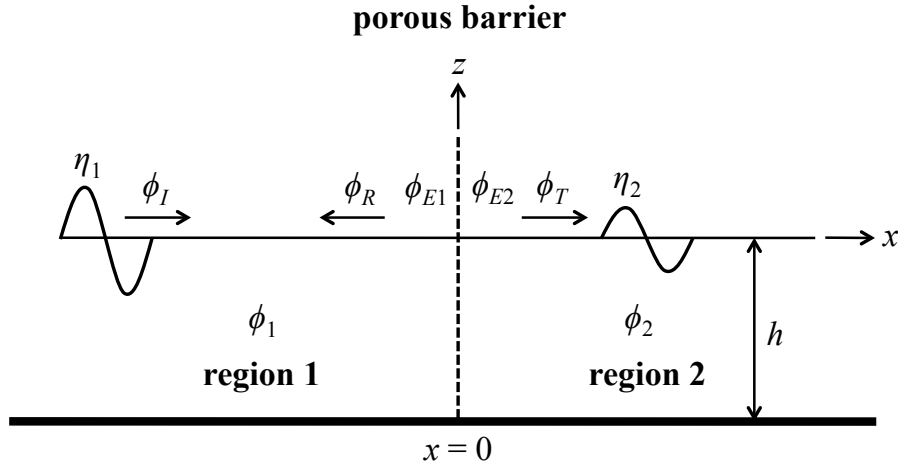


**Figure 11.2:** Profile view of fluid domain.

The boundaries of the fluid domains are constituted of the free surface (top), horizontal bottom surface, porous barrier, and lateral limits (left and right). Let the free surface elevation be  $\eta(x, t)$ , which is the displacement of the free surface with respect to the  $z = 0$  plane. The free surface,  $F(x, z, t)$ , is defined as

$$F(x, z, t) = z - \eta(x, t). \quad (11.7)$$

If we move with the free surface, the total derivative of Equation (11.7) with respect to time would be zero, which gives us the kinematic free surface boundary condition as

$$\frac{dF}{dt} = \frac{\partial F}{\partial t} + u \frac{\partial F}{\partial x} + w \frac{\partial F}{\partial z} = 0. \quad (11.8)$$

By substituting Equation (11.7) into Equation (11.8), we get

$$\frac{\partial \eta}{\partial t} + \frac{\partial \phi}{\partial x} \frac{\partial \eta}{\partial x} = \frac{\partial \phi}{\partial z} \Big|_{z=\eta}. \quad (11.9)$$

The second boundary condition which must be satisfied is the dynamic free surface boundary condition which suggests that the pressure along the wave form should remain constant.

By using the Bernoulli equation, we obtain

$$\frac{\partial \phi}{\partial t} + \frac{1}{2} \nabla \phi \cdot \nabla \phi + g\eta = 0 \Big|_{z=\eta}, \quad (11.10)$$

where  $g$  is the gravitational constant. Based on the linear wave theory, the kinematic and dynamic free surface boundary conditions in regions 1 and 2 can be linearized as

$$\frac{\partial \eta_j}{\partial t} = \frac{\partial \phi_j}{\partial z} \Big|_{z=0}, \quad j = 1, 2 \quad (11.11)$$

and

$$\frac{\partial \phi_j}{\partial t} + g\eta_j = 0 \Big|_{z=0}, \quad j = 1, 2. \quad (11.12)$$

At the horizontal bottom surface, the velocity normal to the surface is zero, hence

$$w = \frac{\partial \phi_j}{\partial z} = 0 \Big|_{z=-h}, \quad j = 1, 2. \quad (11.13)$$

After the linearization of the boundary conditions, the general 2-D solutions for regions 1 and 2 can be derived as

$$\begin{aligned}
\phi_1 &= \phi_I + \phi_R + \phi_{E1} \\
&= I_0 \cosh k_0(z+h)e^{-ik_0x}e^{i\omega t} + R_0 \cosh k_0(z+h)e^{ik_0x}e^{i\omega t} \\
&\quad + \sum_{n=1}^{\infty} R_n \cos k_n(z+h)e^{k_nx}e^{i\omega t}
\end{aligned} \tag{11.14}$$

and

$$\begin{aligned}
\phi_2 &= \phi_T + \phi_{E2} \\
&= T_0 \cosh k_0(z+h)e^{-ik_0x}e^{i\omega t} + \sum_{n=1}^{\infty} T_n \cos k_n(z+h)e^{-k_nx}e^{i\omega t},
\end{aligned} \tag{11.15}$$

where  $k_0$  and  $k_n$  are the wave numbers,  $\omega$  is the angular frequency, and  $R_0$ ,  $R_n$ ,  $T_0$ , and  $T_n$  are the unknown coefficients to be determined. The subscripts 0 and  $n$  denote the progressive and evanescent wave modes, respectively. The coefficient  $I_0$  is related to the incident wave condition, which is given as

$$I_0 = \frac{Hgi}{2\omega \cosh k_0h}, \tag{11.16}$$

where  $H$  is the incident wave height. The angular frequency satisfying the combined free surface boundary conditions (Equations (11.11) and (11.12)) can be related to the wave number by the dispersion relation for the progressive wave mode as

$$\omega^2 = gk_0 \tanh k_0h. \tag{11.17}$$

For the evanescent wave mode, the angular frequency is related to the wave numbers as

$$\omega^2 = -gk_n \tan k_nh, \quad n = 1, 2, 3. \tag{11.18}$$

There is an infinite number of solutions of  $k_n$  to satisfy Equation (11.18).

To interconnect the fluid motions from the two regions, a boundary condition assuming the same normal velocity as the fluid passes through the porous barrier is applied at  $x = 0$

as

$$\frac{\partial \phi_1}{\partial x} = \frac{\partial \phi_2}{\partial x}. \quad (11.19)$$

Substituting  $\phi_1$  and  $\phi_2$  in Equation (11.19) with Equations (11.14) and (11.15) yields

$$\begin{aligned} & -ik_0 I_0 \cosh k_0(z+h) + ik_0 R_0 \cosh k_0(z+h) + \sum_{n=1}^{\infty} k_n R_n \cos k_n(z+h) \\ & = -ik_0 T_0 \cosh k_0(z+h) - \sum_{n=1}^{\infty} k_n T_n \cos k_n(z+h). \end{aligned} \quad (11.20)$$

Using Equations (11.17) and (11.18) within the domain  $-h \leq z \leq 0$ , we have the following orthogonality properties as

$$\begin{aligned} & \int_{-h}^0 \cosh k_0(z+h) \cos k_n(z+h) dz = 0 \\ & \int_{-h}^0 \cos k_n(z+h) \cos k_m(z+h) dz = 0, \quad n \neq m \\ & \int_{-h}^0 \cosh^2 k_0(z+h) dz = \frac{2k_0 h + \sinh 2k_0 h}{4k_0} \\ & \int_{-h}^0 \cos^2 k_n(z+h) dz = \frac{2k_n h + \sin 2k_n h}{4k_n}, \quad n = m. \end{aligned}$$

Equation (11.20) is reduced to

$$k_n R_n \int_{-h}^0 \cos^2 k_n(z+h) dz = -k_n T_n \int_{-h}^0 \cos^2 k_n(z+h) dz \quad (11.21)$$

or

$$\begin{aligned} & -ik_0 I_0 \int_{-h}^0 \cosh^2 k_0(z+h) dz + ik_0 R_0 \int_{-h}^0 \cosh^2 k_0(z+h) dz \\ & = -ik_0 T_0 \int_{-h}^0 \cosh^2 k_0(z+h) dz. \end{aligned} \quad (11.22)$$

From Equations (11.21) and (11.22), we get

$$R_n = -T_n \quad (11.23)$$

and

$$I_0 = R_0 + T_0. \quad (11.24)$$

Another boundary condition that may be applied at  $x = 0$  is Darcy's law (Chwang, 1983; Chwang & Dong, 1984) which suggests that the porous flow velocity is linearly proportional to the pressure jump across the porous barrier and is shown as

$$\frac{\partial\phi_1}{\partial x} = \frac{\partial\phi_2}{\partial x} = u(z)e^{i\omega t} = \frac{b}{\mu}(\rho\frac{\partial\phi_2}{\partial t} - \rho\frac{\partial\phi_1}{\partial t}), \quad (11.25)$$

where  $\mu$  is the dynamic viscosity,  $b$  is a material constant of the porous barrier, and  $\rho$  is the density of the fluid. Substituting  $\phi_1$  and  $\phi_2$  into Equation (11.25) yields

$$\begin{aligned} & -ik_0T_0 \cosh k_0(z+h) - \sum_{n=1}^{\infty} k_nT_n \cos k_n(z+h) = \\ & \frac{b\rho i\omega}{\mu} \left[ T_0 \cosh k_0(z+h) + \sum_{n=1}^{\infty} T_n \cos k_n(z+h) \right. \\ & \left. - I_0 \cosh k_0(z+h) - R_0 \cosh k_0(z+h) - \sum_{n=1}^{\infty} R_n \cos k_n(z+h) \right]. \end{aligned} \quad (11.26)$$

Similarly, the orthogonality properties are applied to reduce Equation (11.26) to

$$\begin{aligned} & -ik_0T_0 \int_{-h}^0 \cosh^2 k_0(z+h) dz = \frac{b\rho i\omega}{\mu} \left[ T_0 \int_{-h}^0 \cosh^2 k_0(z+h) dz \right. \\ & \left. - I_0 \int_{-h}^0 \cosh^2 k_0(z+h) dz - R_0 \int_{-h}^0 \cosh^2 k_0(z+h) dz \right] \end{aligned} \quad (11.27)$$

or

$$\begin{aligned} & -k_nT_n \int_{-h}^0 \cos^2 k_n(z+h) dz = \frac{b\rho i\omega}{\mu} \left[ T_n \int_{-h}^0 \cos^2 k_n(z+h) dz \right. \\ & \left. - R_n \int_{-h}^0 \cos^2 k_n(z+h) dz \right]. \end{aligned} \quad (11.28)$$

The integral parts in Equation (11.27) and (11.28) are further eliminated, and the equations become

$$-ik_0T_0 = \frac{b\rho i\omega}{\mu} [T_0 - I_0 - R_0] \quad (11.29)$$

and

$$-k_nT_n = \frac{b\rho i\omega}{\mu} [T_n - R_n]. \quad (11.30)$$

Substituting  $I_0$  with  $R_0 + T_0$  (Equation (11.24)) and  $T_n$  with  $-R_n$  (Equation (11.23)) yields

$$-ik_0T_0 = \frac{b\rho i\omega}{\mu} \left[ T_0 - (R_0 + T_0) - R_0 \right] \quad (11.31)$$

and

$$k_nR_n = \frac{b\rho i\omega}{\mu} (-2R_n). \quad (11.32)$$

After arranging the terms in Equations (11.31) and (11.32), we obtain

$$R_0 = \frac{\mu k_0 T_0}{2b\rho\omega} \quad (11.33)$$

and

$$R_n = 0. \quad (11.34)$$

As proposed by Chwang (1983) and Chwang and Dong (1984), the porous effect parameter,  $G_0$ , is defined as

$$G_0 = \frac{b\rho\omega}{\mu k_0}. \quad (11.35)$$

$R_0$  can be expressed in terms of  $I_0$  as

$$R_0 = \frac{T_0}{2G_0} = \frac{I_0 - R_0}{2G_0} = \frac{I_0}{2G_0 + 1} \quad (11.36)$$

and  $T_0$  can be expressed in terms of  $I_0$  as

$$T_0 = I_0 \frac{2G_0}{2G_0 + 1}. \quad (11.37)$$

Once the relationships between the coefficients are developed, the coefficients are inserted back to the general solutions. The final forms of the general 2-D solutions in terms of  $I_0$  representing the wave motions in the regions on both sides of the porous barrier are

$$\begin{aligned} \phi_1 = & I_0 \cosh k_0(z + h) e^{-i(k_0x - \omega t)} \\ & + \frac{1}{2G_0 + 1} I_0 \cosh k_0(z + h) e^{i(k_0x + \omega t)} \end{aligned} \quad (11.38)$$

and

$$\phi_2 = \frac{2G_0}{2G_0 + 1} I_0 \cosh k_0(z + h) e^{-i(k_0x - \omega t)}. \quad (11.39)$$

Finally, the free surface elevations in regions 1 and 2 are deduced respectively using the velocity potentials  $\phi_1$  (Equation (11.38)) and  $\phi_2$  (Equation (11.39)) with the linearized dynamic free surface boundary condition (Equation (11.12)) as

$$\begin{aligned} \eta_1 &= a \left[ \cos(k_0x - \omega t) + \frac{1}{2G_0 + 1} \cos(k_0x + \omega t) \right] \\ &= \eta_0 + \frac{a}{2G_0 + 1} \cos(k_0x + \omega t) \end{aligned} \quad (11.40)$$

and

$$\eta_2 = a \frac{2G_0}{2G_0 + 1} \cos(k_0x - \omega t), \quad (11.41)$$

where  $\eta_0$  represents the incident wave profile, and  $a = H/2$  which is the amplitude of the incident waves.

## Chapter 12

# Experimentation on Head Loss Induced by Porous Screens and Wave Transformation Caused by Obstructing Structures

### 12.1 HEAD LOSS INDUCED BY FLOWS THROUGH A POROUS SCREEN

This part of the research focused on the experimental investigation of head loss associated with fluids flowing through porous screens under various flow rate conditions. The effects of screen material properties such as pore size, porosity, and angle of inclination on head loss were studied.

All the tests were carried out in a rectangular glass-walled flume. The flume has the dimensions of 25 ft in length, 1 ft in width, and 3 ft in depth. Water was supplied into the flume from a recirculation system consisting of an underground storage basin, an underground channel, an elevated head tank, and a pump system. A full cycle began with water being pumped from the underground storage basin to the elevated head tank such that a constant head could be maintained. The incoming flow from the head tank to the flume was controlled with valves to reach the desired flow rate condition. After the flow had passed the testing section of the flume, the water was conveyed back to the storage basin via the underground channel to complete the cycle. The flume and main components of the recirculation system are shown in Figure 12.1.

The porous screens were fabricated to the specifications shown in Table 12.1. A total of eight screens were made, and they were divided into two sets with four screens in each set. The first set has a pore diameter,  $D$ , of 1/4 inch. The second set has a pore diameter of 1/8 inch. One screen from each set carries a matching porosity. The porosities,  $\Phi$ , are 16.08%, 22.67%, 29.61%, and 40.31%. The screens are made of 11 gauge galvanized steel, and the pore pattern is the standard round 60 degree staggered pattern. This pattern allows



**Figure 12.1:** Flume (left) and main components of recirculation system (right).

the screen porosity to be calculated using Equation (12.1)

$$\Phi = \frac{90.69D^2}{C^2}, \quad (12.1)$$

where  $C$  is the center to center distance between any two pores, and  $D$  is the pore diameter.

Two screens of different pore sizes that carry a matching porosity are shown in Figure 12.2.

**Table 12.1:** Screen specifications.

set 1				
$D$ , in =	1/4			
$C$ , in =	3/8	7/16	1/2	19/32
$\Phi$ , % =	40.31	29.61	22.67	16.08
set 2				
$D$ , in =	1/8			
$C$ , in =	3/16	7/32	1/4	19/64
$\Phi$ , % =	40.31	29.61	22.67	16.08

Different flow rate conditions could be established by adjusting the flow control valves located on the pipes entering and exiting the head tank. The flow rates for each test ranged from 0.3 to 2.2 ft<sup>3</sup>/s, and an average of ten flow rates with an approximate increment of 0.2 ft<sup>3</sup>/s were established. A flow rate measuring system, product of Pulsar Process Measurement Inc., consisting of an ultrasonic water depth transducer, a flow velocity sensor (Speedy), and a controller unit (Ultra 5) was employed to measure the flow rates established for the tests. The ultrasonic water depth transducer and the flow velocity sensor were placed

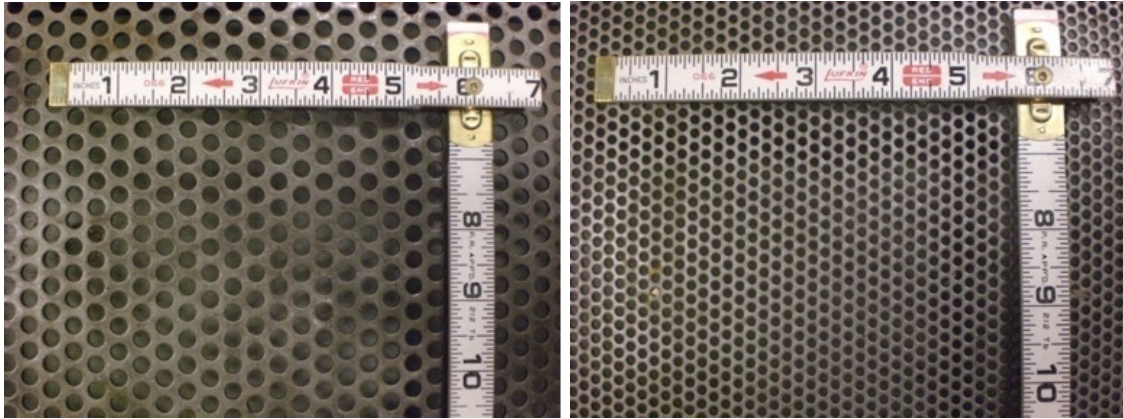


**Figure 12.2:** 1/4" diameter, 40.31% porosity (left), and 1/8" diameter, 40.31% porosity (right).

in the undisturbed region upstream of the screen being tested. Signals from both devices then were sent back to the controller unit for flow rate computation. The water depth upstream of the screen and the established flow rate were determined using the Pulsar system, while the water depth in the downstream section of the screen where the flow region was not significantly disturbed was measured with a point gauge. During a test, the porous screen being tested was secured in the flume with a mounting seat, which was placed on the bottom of the flume, and a brace, which was fastened on top of the rails of the flume. The screen was positioned at three different angles of inclination, which were  $90^\circ$ ,  $75^\circ$ , and  $63^\circ$ , to test the effect of inclination on head loss. With the known flow velocity, water depth, and flow rate information, the upstream and downstream heads could be calculated. The head loss was then determined. The Speedy velocity sensor and the Ultra 5 controller unit are shown in Figure 12.3.

## 12.2 WAVE TRANSFORMATION CAUSED BY A POROUS BARRIER

For the investigation of wave transformation caused by porous barriers, the flume used for the flow head loss study was converted into a closed end wave flume. A piston-typed wave maker with a 0.75 inch thick aluminum paddle attached to a double-carrier linear actuator was installed on one end of the flume. The position of the paddle could be prescribed through the control software to generate the desired incident wave conditions. A closed-loop feedback process which constantly corrects the paddle position by minimizing

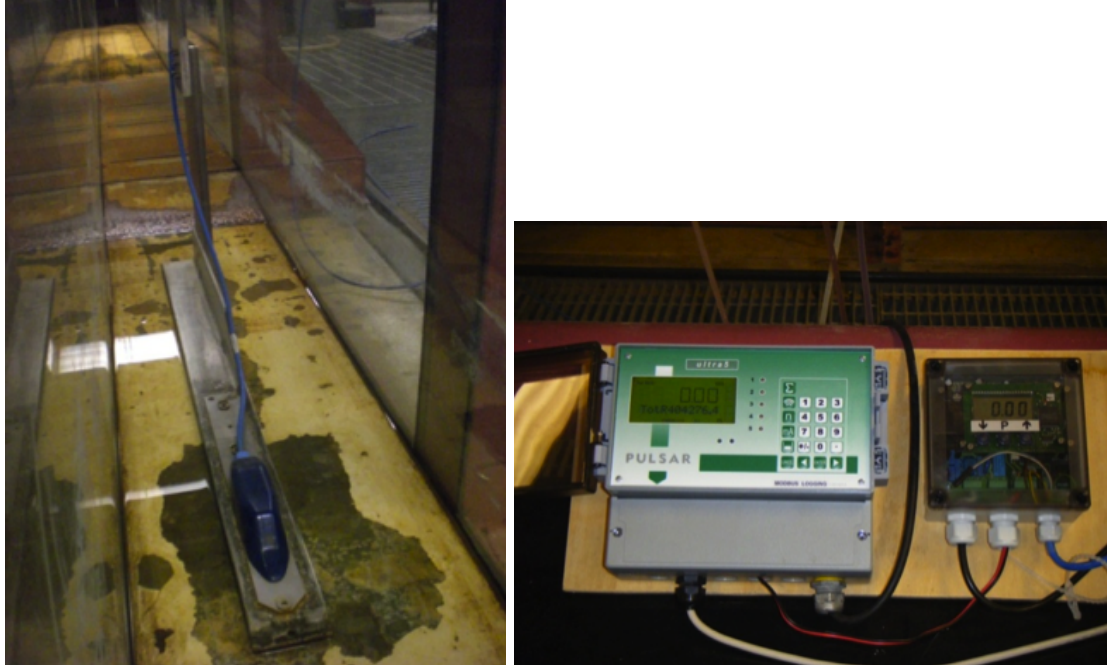


**Figure 12.3:** Speedy velocity sensor (left), and Ultra 5 controller (right) by Pulsar.

the position error between the targeted and actual paddle positions was also implemented in the control software. Figure 12.4 shows the wave maker.

In order to simulate an infinitely long wave flume, energy dissipators that were made of bags of gravel were placed on both ends of the flume to prevent unwanted waves from bouncing back into the testing domain. Resistance-typed wave gauges were used to record wave profiles. Prior to the tests, voltage versus water surface elevation relationships were developed to calibrate the gauges. Figure 12.5 shows the gauge calibration relationships.

As introduced previously, Chwang (1983) proposed using Darcy's law as one of the boundary conditions to interconnect the wave motions in the upstream and downstream regions of the porous barrier. The porous effect parameter,  $G_0$  (Equation (11.35)), is a function of incident wave conditions (e.g., frequency) as well as  $b$ , which is a barrier material constant that is dependent on, in this study, the porous screen properties such as porosity, pore diameter, and other factors. The main objectives of this part of the research were to experimentally determine  $b$  and to validate the use of Darcy's law as a boundary condition.

To carry out the tests, the flume was configured as shown in Figure 12.6. The undisturbed water depth,  $h$ , was set at 9 inches. The same screens (specifications included in

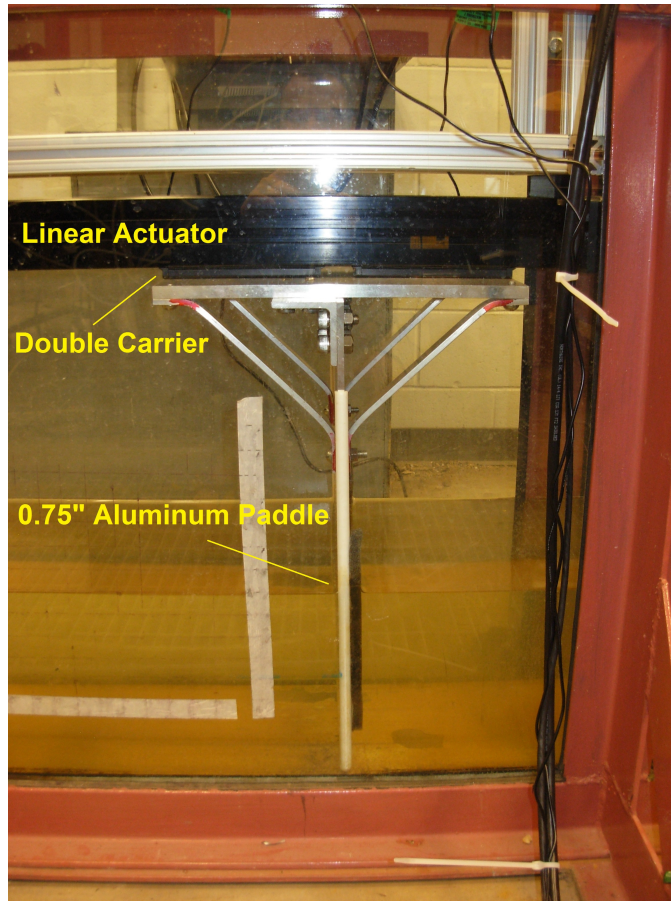


Figure 12.4: Wave maker.

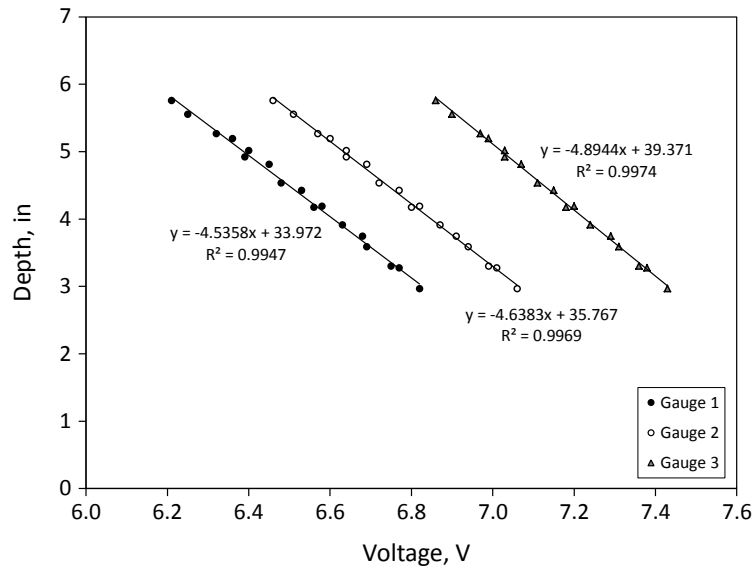
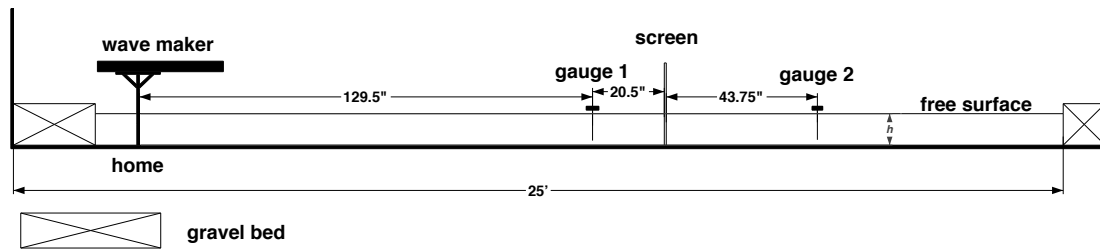


Figure 12.5: Wave gauge calibration relationships.

Table 12.1) used in the head loss study were reused as the porous barriers. For each test, a single screen was placed perpendicularly to the direction of incident waves. Sinusoidal incident waves with four different sets of wave properties were generated and propagated past the screen by prescribing the stroke lengths,  $S$ , and oscillating frequencies,  $f$ , to the wave maker. The information associated with the incident waves is shown in Table 12.2, where  $\varepsilon$  is the dimensionless wave height that was determined by normalizing the measured incident wave height with respect to  $h$ . A porous screen that was set up perpendicularly to the direction of incident waves is shown in Figure 12.7. Note that the gaps between the edges of the screen and the glass panels of the flume were stuffed with foam tapes to deter water from slipping through.



**Figure 12.6:** Wave flume configuration with a porous screen.

**Table 12.2:** Incident waves generated for wave transformation by porous screen tests.

ID	$\varepsilon$	$S$ , in	$f$ , Hz
1	0.265	0.825	1.78
2	0.235	0.75	2
3	0.246	0.825	2
4	0.23	1	1

Two wave gauges were employed to record wave profiles. Gauge 1 was placed 129.5 inches from the home position of the paddle and 20.5 inches upstream of the screen. Gauge 2 was placed 43.75 inches downstream of the screen. The profiles recorded by Gauge 1 contained components of the incident and reflected waves, whereas Gauge 2 recorded only the transmitted wave profiles. The locations of the gauges were carefully selected such that the wave profiles recorded were not affected by the evanescent waves which were formed within the vicinity of the screen. With the variations of incident wave condition, pore diameter,



**Figure 12.7:** Porous screen configured perpendicularly to direction of incident waves.

and porosity, sufficient data were produced for the analyses. In addition, the tests were conducted numerous times to ensure repeatability of the results.

It should be noted that the majority of the results presented in this study were based on the analyses done on the data (transmitted waves) recorded at Gauge 2. The reflected waves would require extensive effort and additional equipment to be decomposed from the more complex wave profiles recorded at Gauge 1, which was not within the scope of this research.

### **12.3 WAVE TRANSFORMATION CAUSED BY A SUBMERGED CAVITY**

For this part of the experimental investigation, the wave flume configuration from Section 12.2 was slightly modified as shown in Figure 12.8. Two movable sections of an up-leveled acrylic made floor separated by the distance of  $W^*$  were placed in the flume to create a trench section of varying opening sizes for the investigation of wave transformation caused by submerged cavities.

The undisturbed water depth,  $h$ , ahead and beyond the trench zone for all the test

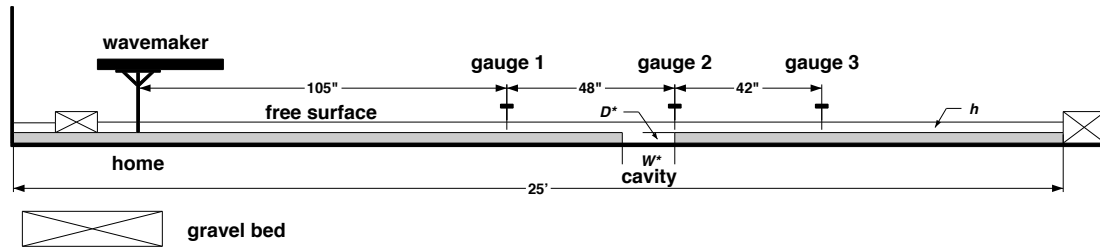


**Figure 12.8:** Wave flume configuration with a submerged cavity.

cases was set to 3 inches. By letting the trench depth,  $D^*$ , be 3 inches would result in a total water depth of 6 inches inside the trench zone. Incident solitary waves with dimensionless wave height  $\alpha$ , defined as  $\alpha = H/h$  where  $H$  is the wave height, of 0.42, 0.27, and 0.14 were generated to create different incident wave conditions. Four different dimensionless trench opening sizes  $W = W^*/h = 1, 1.9, 3.5,$  and 5 were tested to examine the effect of trench opening on the propagation of incident waves and flow pattern within the trench zone. The tests conducted with  $W = 1$  and 1.9 were dedicated for the analysis of flow pattern, while the recorded wave profiles (elevation) from the cases with trench openings of 3.5 and 5 were applied for comparisons against numerical solutions (Chang et al., 2011). Three resistance-typed wave gauges were placed along the flume to record the incident, reflected and transmitted wave profiles. Gauge 1 was 48 inches ahead of Gauge 2 that was aligned with the end face of the trench. Gauge 3 at the downstream of the trench was separated from Gauge 2 by 42 inches.

The Planar Laser Induced Fluorescence (PLIF) technique was utilized to visualize the flow pattern, especially wave induced vortices around the trench zone and the follow-up entrainment of the fluid particles, as an incident solitary wave propagated over the submerged trench. The laser module set over the trench zone as shown in Figure 12.9 has a wavelength of 532 nm (green light). A very thin laser sheet that was generated from a set of optic lenses was projected over the trench region as seen in Figure 12.10. By changing the focus of the lenses, the thickness of the laser sheet could be adjusted. The module output power of 20 mW was adequate for the laser to penetrate the maximum water depth of 6 inches (free surface to bottom of the trench), and the projection fan angle of 100 degree was also wide enough to cover the maximum trench opening of 15 inches.

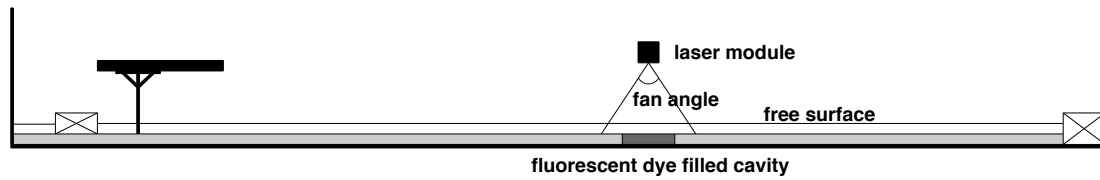


**Figure 12.9:** Configuration of laser module.

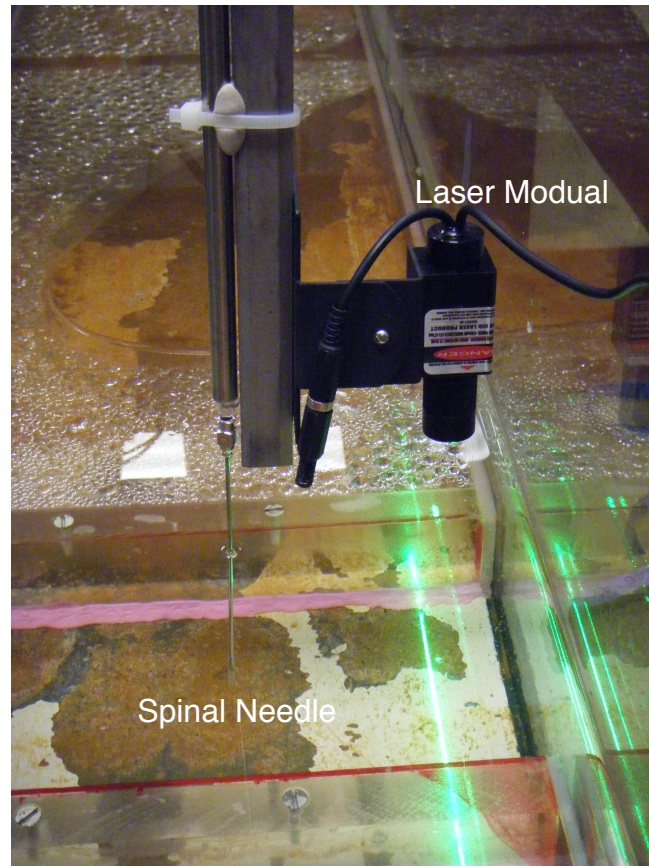


**Figure 12.10:** Laser sheet projected over submerged trench.

The fluorescent dye solution of Rhodamine B, Basic Violet 10, was filled in the trench region to enhance the visualization of the flow pattern and formation of the vortices as the dye molecules carried by the fluid motion were excited and illuminated by the laser as an incident wave propagated past the trench zone. Dye solutions with different concentrations were made and tested. It was found that mixing 0.003 grams of Rhodamine B with 1 liter of distilled water, 0.003 g/L, would provide the optimal flow pattern visualization. The dye solution was slowly injected into the trench through a 15 gauge spinal needle, which

was connected to a 1/8 inch diameter vinyl tubing. A clamp was used to control the flow of the dye solution into the trench. The dye injection process was gravity driven. The schematic and the image of the injection apparatus are included in Figures 12.11 and 12.12, respectively. A dye filled trench with laser sheet projected over it before the arrival of the incident wave is shown in Figure 12.13. Each test was recorded with a video camera, and selected image frames were further processed for analyses or for comparisons with the results obtained, for example, from numerical simulations.

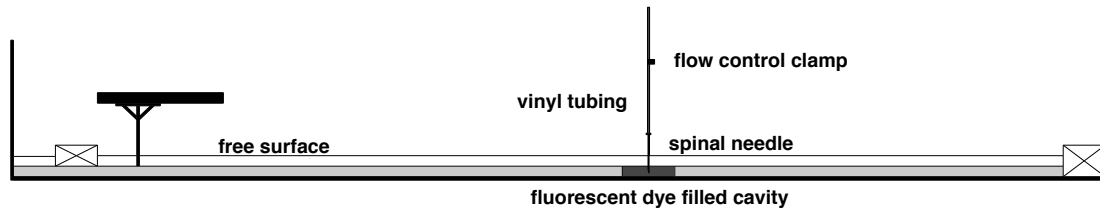


**Figure 12.11:** Configuration of fluorescent dye injection system.

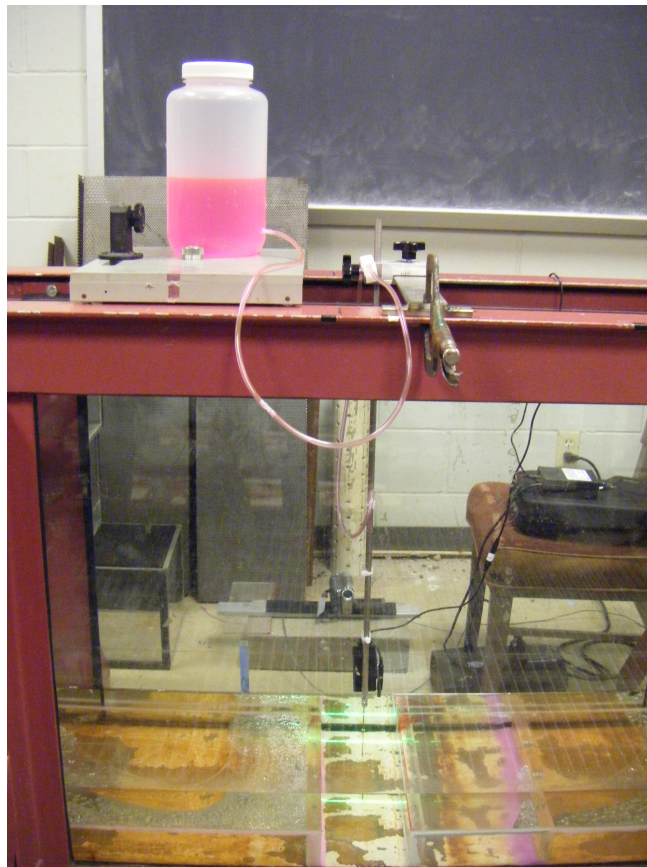


**Figure 12.12:** Gravity driven injection apparatus.

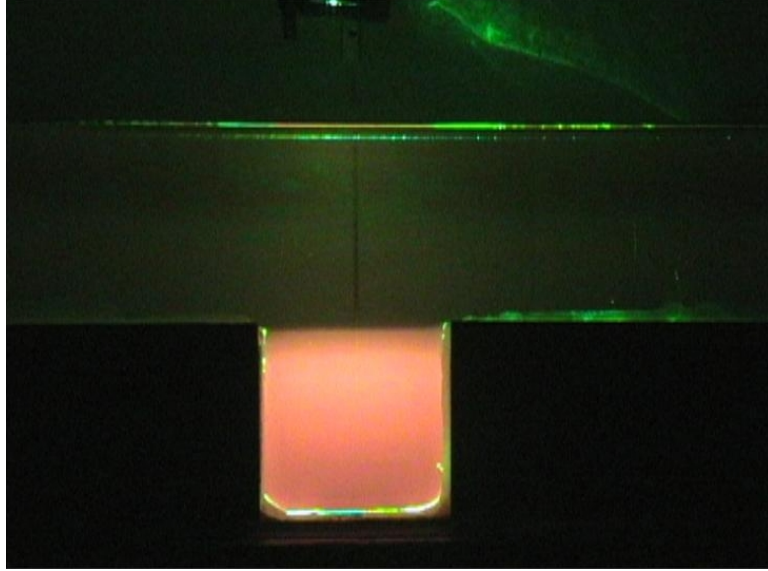


**Figure 12.13:** Submerged cavity filled with fluorescent dye solution.

## Chapter 13

### Results

#### 13.1 FLOW HEAD LOSS INDUCED BY A POROUS SCREEN

For the head loss study, more than one hundred tests were carried out in order to acquire sufficient data for the analysis of the effects of screen pore size, porosity, and angle of inclination on head loss. An average of 10 different flow rate conditions ranging from 0.3 to 2.2 ft<sup>3</sup>/s with a 0.2 ft<sup>3</sup>/s flow increment were developed for each test. Flow properties such as averaged velocity and depth in the regions upstream and downstream of the screen being tested were determined, and the head loss induced by the screen was calculated.

It can be observed from the experiments that the free surface drops exponentially to a much shallower depth downstream of the screen as the fluid flows through the screen. In addition, tiny air bubbles are ejected from the pores indicating that the fluid exits the pores with very high velocities. In the case of the screen with a larger porosity (e.g.,  $\Phi = 40.31\%$ ), the free surface appears to form a much smoother envelope descending towards the downstream uniform depth (photo on the left in Figure 13.1). In contrast, for the screen with a smaller porosity (e.g.,  $\Phi = 22.67\%$ ), a steeper and much turbulent free surface envelope can be noticed (photo on the right in Figure 13.1). The free surface downstream of the screen shows amplified fluctuation.

A series of plots of the calculated values of head loss (Equation (11.2)) against the corresponding values of the square of upstream averaged flow velocity were produced. Figure 13.2 shows the relationships between head loss and  $V_1^2$ , where  $V_1$  denotes the upstream averaged flow velocity, for the two sets of screens of pore diameters of 1/4 and 1/8 inches at the angle of inclination of 90 degree. It can be observed that head loss, in general, is linearly proportional to  $V_1^2$ . In addition, less head loss is induced with screens of greater porosities under the same flow rate condition (same  $V_1$ ).

The effect of screen pore size on head loss was also explored. Head loss versus  $V_1^2$

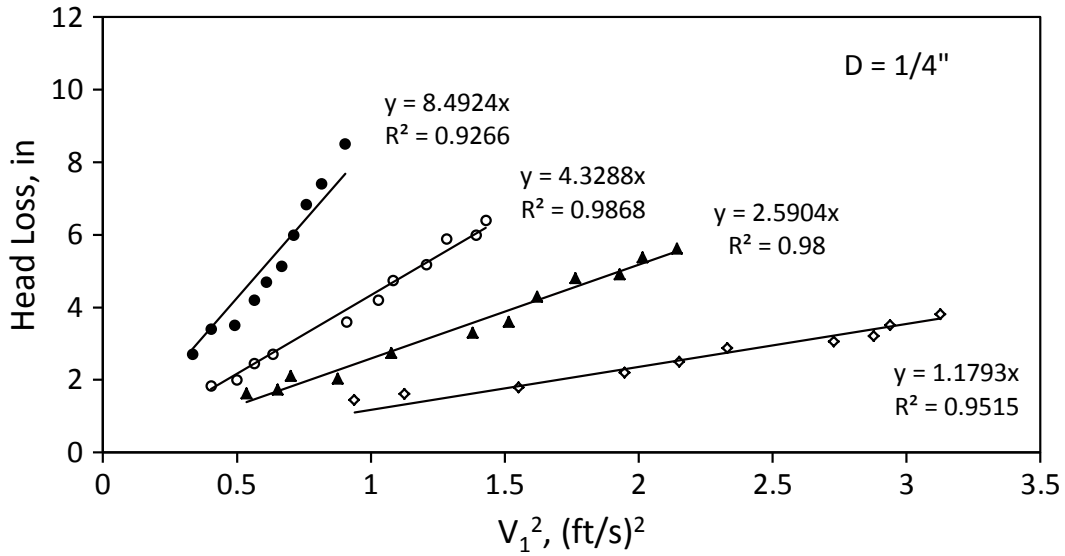


**Figure 13.1:** Free surface profiles downstream of screens,  $\Phi = 40.31\%$  (left) and  $\Phi = 22.67\%$  (right).

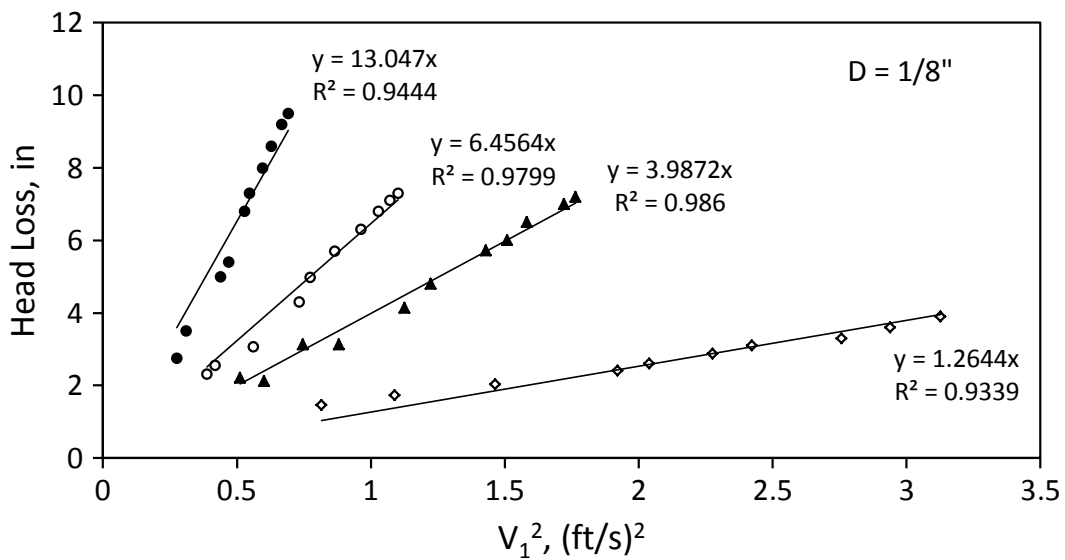
for screen pore sizes of 1/8 and 1/4 inches under various porosity conditions (e.g., 40.31%, 29.61%, 22.67%, and 16.08%) are plotted in Figure 13.3 and Figure 13.4. For screen porosity equals 40.31%, the measured data suggest that pore size does not show a prominent effect on head loss. As can be seen in the top sub-figure of Figure 13.3, no significant difference in head loss for the screens of different pore sizes can be observed; two sets of data points are on top of each other. For porosity less than 40.31%, in this case 29.61%, 22.67%, and 16.08%, pore size becomes an important factor in inducing head loss. As can be seen in the bottom sub-figure of Figure 13.3 and Figures 13.4, two trends, representing the two sets of screens with two different pore sizes, deviate from each other, where greater head loss is induced by screens with smaller pore size.

The porous screens were positioned at three angles of inclination,  $90^\circ$ ,  $75^\circ$ , and  $63^\circ$ , to test the effect of inclination on head loss. Figures 13.5 and 13.6 present the relationships between head loss and  $V_1^2$  for the sets of screens of pore diameters of 1/4 and 1/8 inches, respectively, at the three specified angles of inclination. The results demonstrate that less head loss was induced when the flow was passing through the screen inclined at lower angles. This physical phenomenon can be reasoned by relating the angle of inclination,  $\theta$ , to the averaged upstream flow velocity,  $V_1$ , as

$$V_{normal} = V_1 \sin \theta, \quad (13.1)$$



● Porosity = 16.08%   ○ Porosity = 22.67%   ▲ Porosity = 29.61%   ◇ Porosity = 40.31%



● Porosity = 16.08%   ○ Porosity = 22.67%   ▲ Porosity = 29.61%   ◇ Porosity = 40.31%

**Figure 13.2:** Relationships of head loss v.s. square of upstream averaged flow velocity,  $V_1^2$ .

where  $V_{normal}$  is the velocity component of  $V_1$  normal to the screen. Following Equation (13.1), the normal velocity is at its maximum and identical to  $V_1$  at  $90^\circ$  and starts to decrease as the angle of inclination decreases from  $90^\circ$ . As a result, the decrease in normal velocity leads to the reduction in head loss.

The averaged pore velocity which accounts for the effects of screen porosity and angle

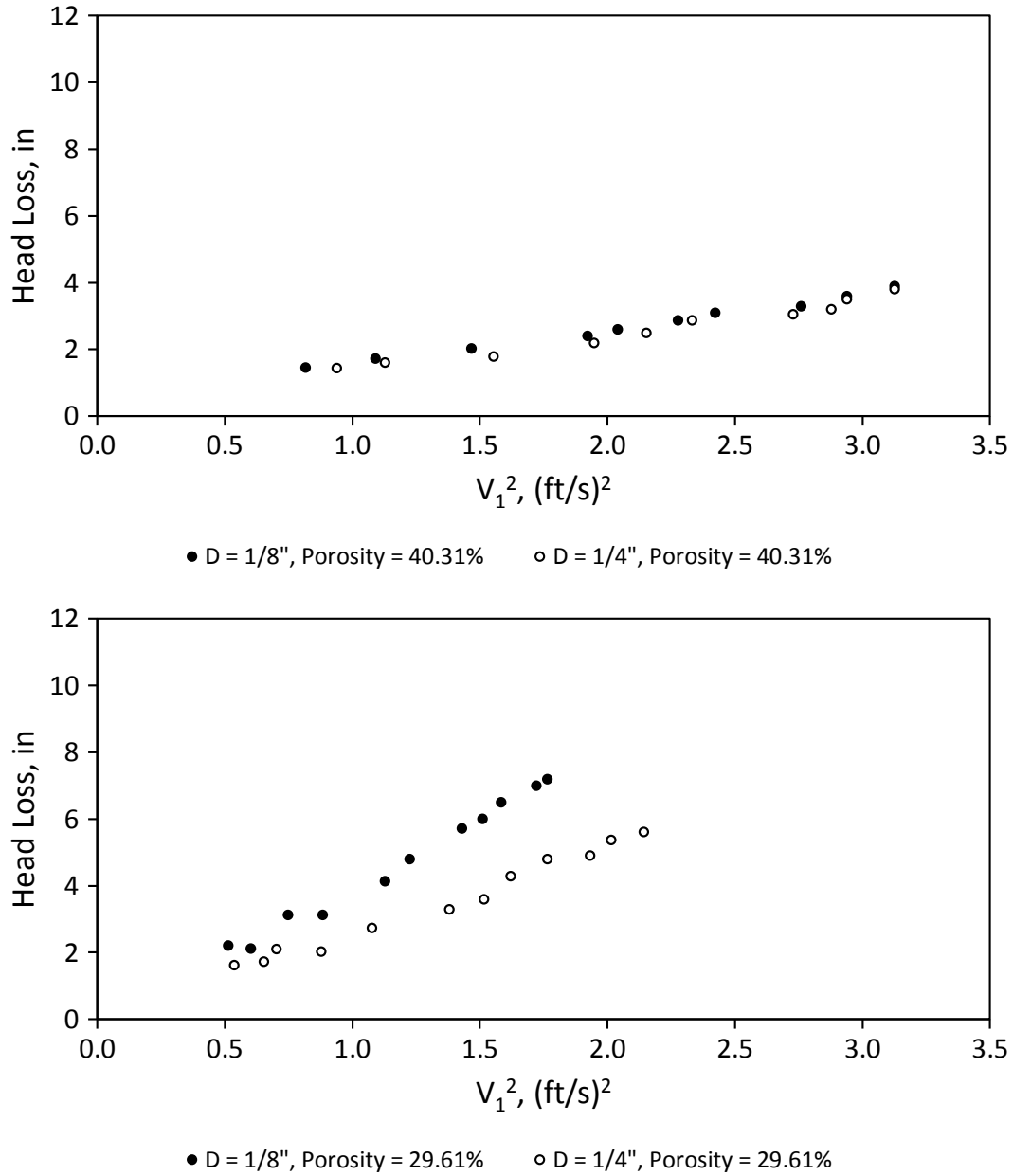


**Figure 13.3:** Effect of screen pore size on head loss for porosities of 40.31% and 29.61%.

of inclination is defined by Equation (13.1) as

$$V_p = \frac{V_1 \sin \theta}{\Phi},$$

where  $\Phi$  and  $\theta$  are respectively the porosity and angle of inclination of the screen. It is shown in Figure 13.7 that by plotting head loss versus the square of averaged pore velocity,

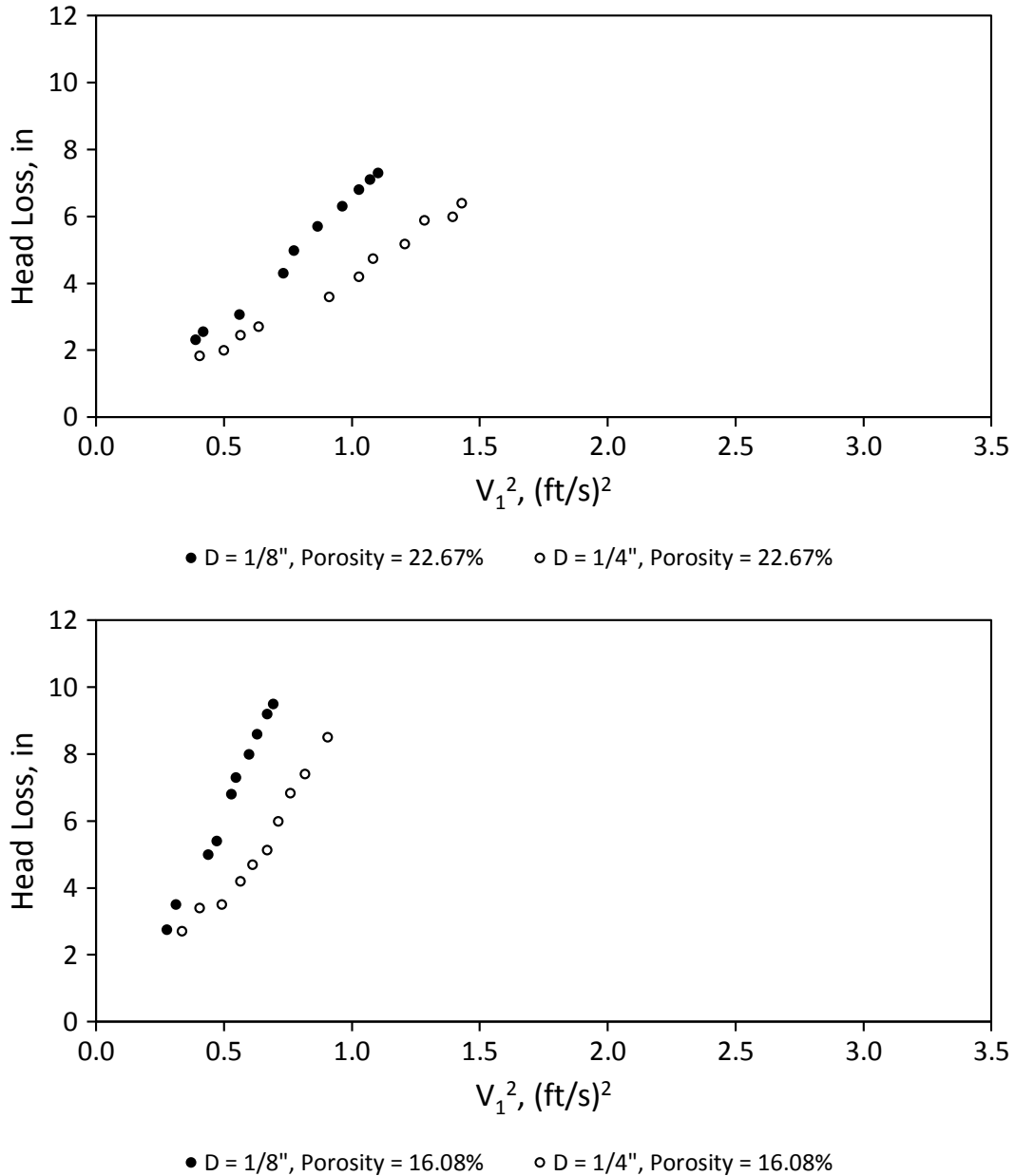


**Figure 13.4:** Effect of screen pore size on head loss for porosities of 22.67% and 16.08%.

the data points from the entire test cases (various screen porosities and angles of inclination) form two distinct linear trends for the screen sets of pore diameters of 1/4 and 1/8 inches. It is interesting to note that the data points for pore diameter equals 1/8 inches and porosity equals 40.31% (blue points) collocate with the data points for pore diameter of 1/4 inches (red points) demonstrating that pore size has insignificant influence on head loss when the porosity is higher (e.g.,  $\Phi = 40.31\%$  or higher) and shows impact on head loss with lower

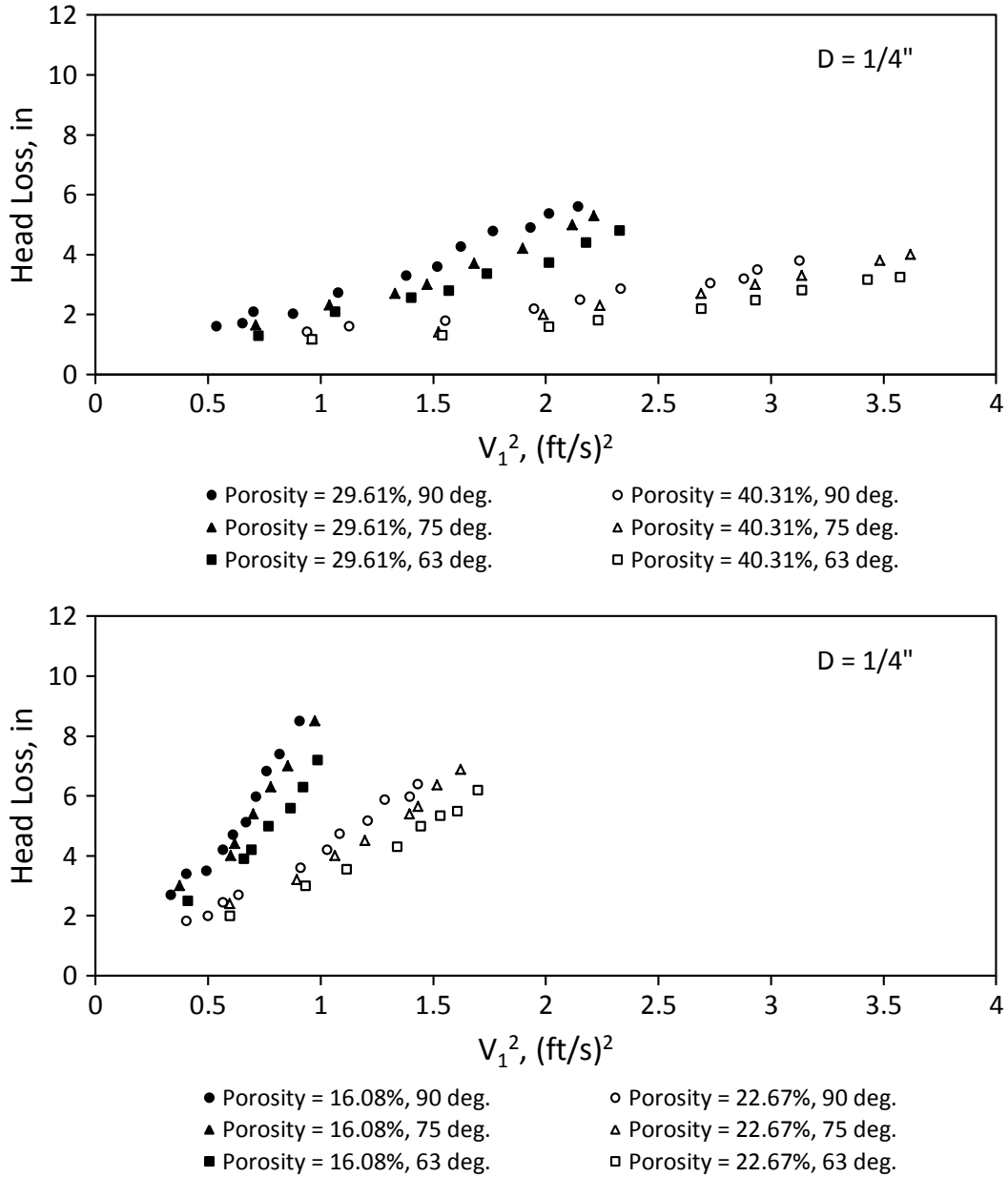


**Figure 13.5:** Effect of angle of inclination on head loss for pore diameter of 1/4".

porosities (29.61%, 22.67%, and 16.08%), which reconfirms the earlier findings indicated in Figure 13.3 and 13.4. The two linear models can be used for head loss prediction when the averaged pore velocity is known. For  $D = 1/4$  inches, head loss =  $0.215V_p^2$ . For  $D = 1/8$  inches and porosity less than 40.31%, head loss =  $0.329V_p^2$ .

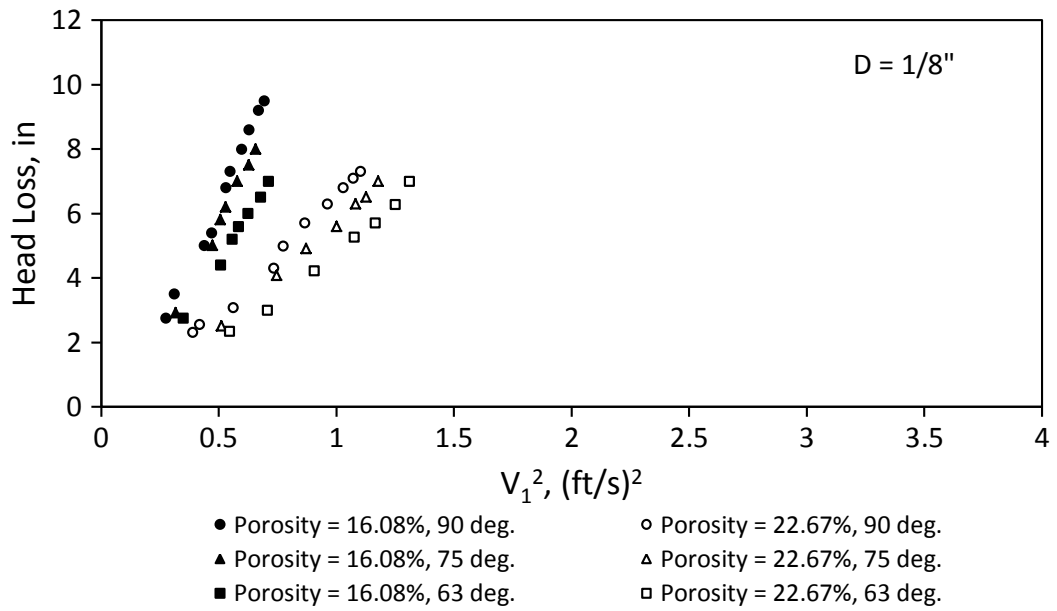
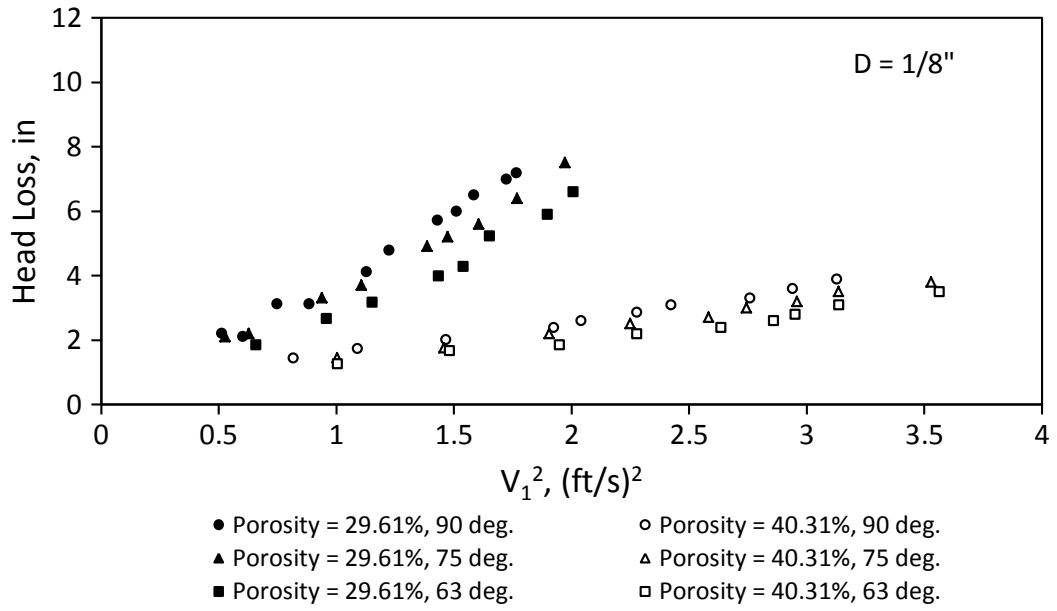
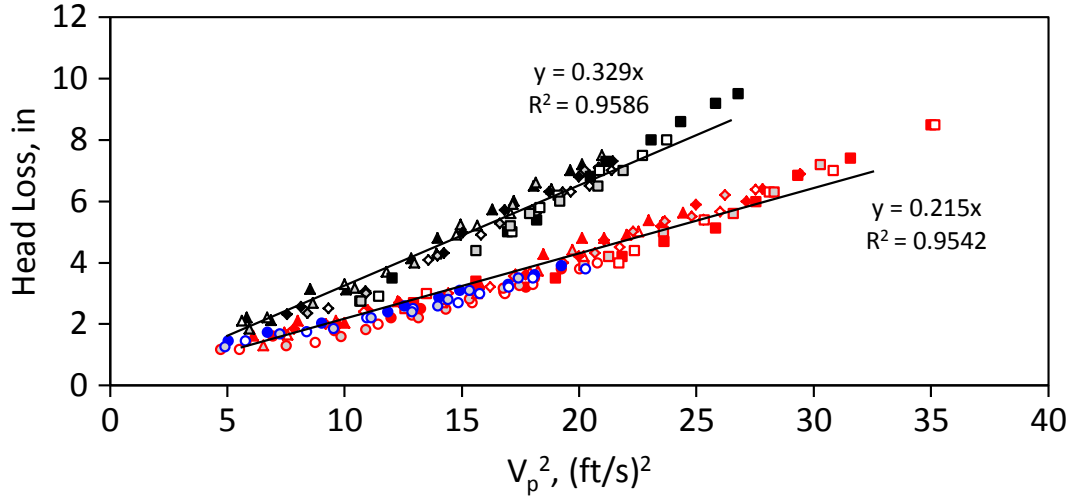


Figure 13.6: Effect of angle of inclination on head loss for pore diameter of 1/8".



Blue:  $D = 1/8''$ , Porosity = 40.31%, Angle = 90, 75, 63 deg.  
 Black:  $D = 1/8''$ , Porosity = 29.61, 22.67, 16.08%, Angle = 90, 75, 63 deg.  
 Red:  $D = 1/4''$ , Porosity = 40.31, 29.61, 22.67, 16.08%, Angle = 90, 75, 63 deg.

**Figure 13.7:** Relationships of head loss v.s. square of averaged pore velocity,  $V_p^2$ , for pore diameters of 1/4" and 1/8".

### 13.2 WAVE TRANSFORMATION CAUSED BY A POROUS BARRIER

The coefficients  $R_0$  and  $T_0$ , which are associated with the terms that represent the reflected and transmitted wave motions in the derived solutions (Section 11.2), are related to the incident wave condition and porous effect parameter,  $G_0$ , as shown by Equations (11.36) and (11.37), respectively, as

$$R_0 = I_0 \frac{1}{2G_0 + 1}$$

and

$$T_0 = I_0 \frac{2G_0}{2G_0 + 1}.$$

Based on the linear wave theory, wave energy is proportional to the square of wave height.

We can define the coefficient of reflection,  $C_R$ , and coefficient of transmission,  $C_T$ , as

$$C_R = \left(\frac{R_0}{I_0}\right)^2 = \frac{1}{(2G_0 + 1)^2} \quad (13.2)$$

and

$$C_T = \left(\frac{T_0}{I_0}\right)^2 = \left(\frac{2G_0}{2G_0 + 1}\right)^2 = \frac{4G_0^2}{(2G_0 + 1)^2}. \quad (13.3)$$

The coefficients may be interpreted respectively as the energy ratios of the reflected and transmitted waves to the incident waves. Figure 13.8 presents the relationships of  $C_R$ ,  $C_T$ , and  $C_R + C_T$  versus  $G_0$  to show the variation of wave energy for waves propagating past a porous barrier. It can be seen that as  $G_0$  approaches zero, the porous barrier becomes impermeable which indicates that the incident wave energy is completely reflected ( $C_R = 1$ ) and no wave transmission will occur ( $C_T = 0$ ). In contrast, the porous barrier is fully permeable as  $G_0$  tends to infinity. The entirety of the incident waves will be transmitted ( $C_R = 0$ ) through the barrier. However,  $C_T$  will not reach unity because a fraction of the energy is dissipated during the passing of the incident waves through the barrier.

For a wave system,  $C_R + C_T$  represents the net energy ratio of the system after the interaction between the waves and porous barrier. The value of  $C_R + C_T$  is equal to one at  $G_0 = 0$  and continues to decrease until the minimum energy level is reached at  $G_0 = 0.5$  (maximum energy dissipation). At this point, only 50% of the system energy remains. The remaining energy is carried evenly by the reflected and transmitted waves (25% of the incident wave energy each). This suggests that it would be more effective to use porous media that have  $G_0$  values close to 0.5 for applications that require energy dissipation. After passing the minimum point, the  $C_R + C_T$  curve follows the  $C_T$  curve closely as  $G_0$  becomes greater.

Another theoretical relationship associated with  $C_T$  can be presented with the introduction of a porous barrier related Reynolds number. By combining Equations (11.17) and (11.35), we obtain

$$G_0 = Re \left( \frac{\tanh k_0 h}{k_0 h} \right)^{\frac{1}{2}}, \quad (13.4)$$

where

$$Re = \frac{\rho b \sqrt{g h}}{\mu} \quad (13.5)$$

is the Reynolds number associated with the flows passing through the opening of the barrier. The relationships of  $C_T$  versus  $k_0 h$  for the cases of  $Re = 5$  and  $Re = 1$  are presented in

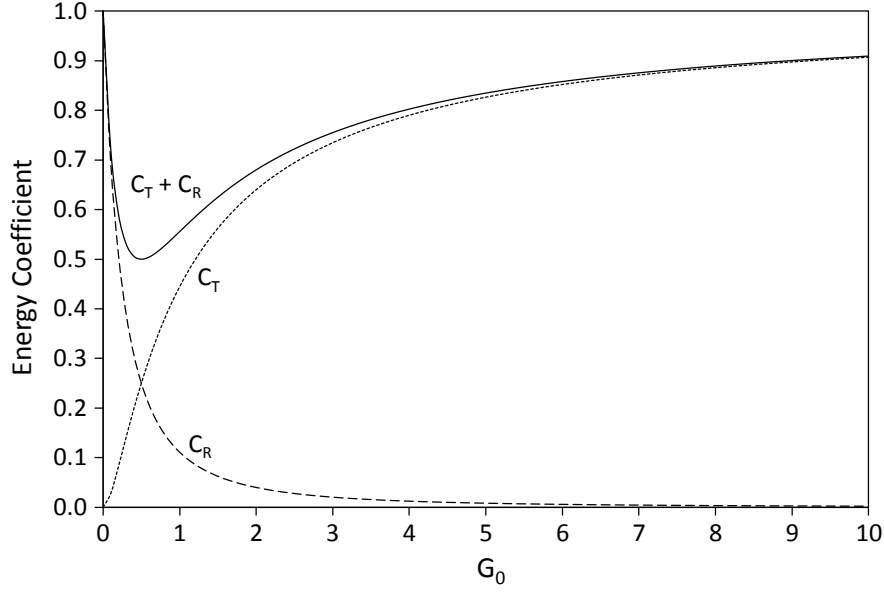


**Figure 13.8:** Theoretical relationships of energy coefficients v.s. porous effect parameter.

Figure 13.9. The wave number of the incident waves,  $k_0$ , is defined as  $k_0 = \frac{2\pi}{\lambda}$  where  $\lambda$  is the wavelength. Therefore, the larger the value of  $k_0 h$  reflects waves with shorter wavelength. It can be seen that  $C_T$  decreases as  $k_0 h$  increases which indicates that it is easier for the incident wave energy to be transmitted through the porous barrier for waves with relatively longer wavelength as opposed to shorter wavelength waves. It is also interesting to note that the porous barrier that yields a lower Reynolds number will have a lower coefficient of transmission under the same incident wave condition. Hence, the greater the Reynolds number (generally with a greater  $b$  value), the easier it is for wave energy to pass through the barrier.

In this research, porous screens as porous barriers were used for the investigation of wave transformation caused by the barriers. From Equation (11.35)

$$G_0 = \frac{b\rho\omega}{\mu k_0}$$

by combining with Equation (11.37) we have

$$b = \frac{G_0 \mu k_0}{\rho \omega} = \frac{\frac{T_0}{I_0} \mu k_0}{2(1 - \frac{T_0}{I_0}) \rho \omega} = \frac{C_T^{0.5} \mu k_0}{2(1 - C_T^{0.5}) \rho \omega}. \quad (13.6)$$

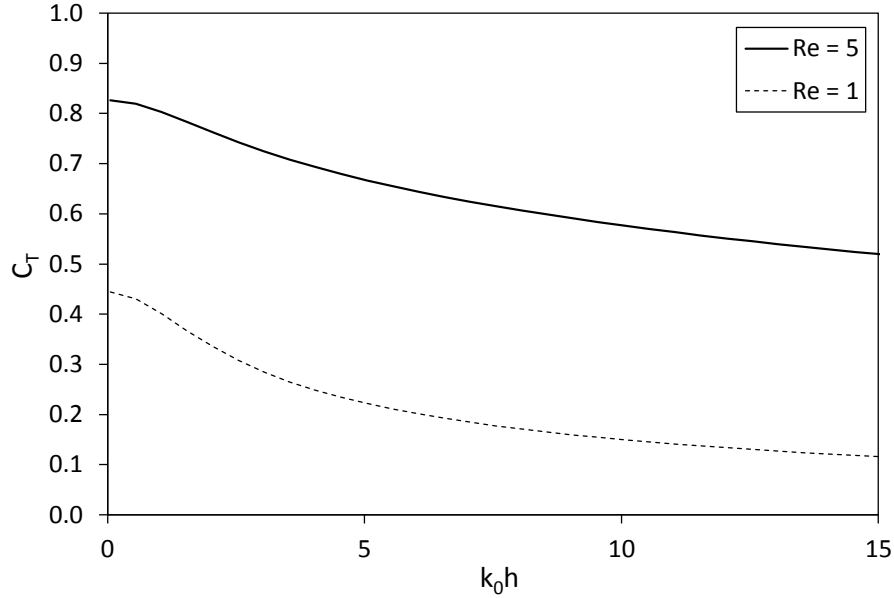


**Figure 13.9:** Theoretical relationship of  $C_T$  v.s.  $k_0 h$ .

Once  $T_0$  and  $I_0$  are determined experimentally, the value of  $b$  can be calculated by Equation (13.6). For each screen tested, two  $b$  values were deduced under the incident wave conditions 1 and 2 as specified in Table 13.1. Ideally, the  $b$  values should be very close to the material constant that is unique to a screen. However, the deduced  $b$  values were slightly different. The two values were averaged, and the resulting value is referred as the calibrated  $b$  value for a given screen tested. Table 13.2 summarizes the calibrated  $b$  values that were determined uniquely for the eight porous screens.

**Table 13.1:** Incident wave conditions generated for determination and verification of  $b$  values.

ID	$\varepsilon$	$k_0$ , rad/ft	$\omega$ , rad/sec
1	0.265	3.93	11.22
2	0.235	4.91	12.57
3	0.246	4.91	12.57
4	0.230	1.51	6.28

The derived analytical formulations in terms of the coefficient of transmission with the calibrated  $b$  values were verified with the incident wave conditions 3 and 4 (Table 13.1). The values of  $G_0$  for the porous screens were calculated using the calibrated  $b$  values and are summarized in Table 13.3. The corresponding  $C_T$  values were determined from the

**Table 13.2:** Calibrated  $b$  values of porous screens tested.

$D =$	1/8"	1/4"
$\Phi, \%$	$b, \text{ft}$	$b, \text{ft}$
40.31	$6.00 \times 10^{-6}$	$1.20 \times 10^{-5}$
29.61	$4.40 \times 10^{-6}$	$6.20 \times 10^{-6}$
22.67	$2.50 \times 10^{-6}$	$4.00 \times 10^{-6}$
16.08	$2.00 \times 10^{-6}$	$2.50 \times 10^{-6}$

recorded incident and transmitted wave heights. The data pairs ( $C_T$  and  $G_0$ ) were plotted against the theoretical  $C_T$  versus  $G_0$  curve as shown in Figure 13.10. The theoretical curve follows the data points closely. The comparisons in Figure 13.10 suggest that the calibrated  $b$  values are material constants and applicable for the same screens under other incident wave conditions. With the determined material properties of the porous screens, the derived theoretical model is proved to be able to make reasonable predictions on transmission of waves propagating through the screens. It is also demonstrated that Darcy's law may be adopted as a boundary condition in modeling waves propagating through porous barriers.

**Table 13.3:** Values of  $G_0$  and corresponding  $C_T$  for porous screens tested under incident wave conditions 3 and 4.

Incident Wave Condition 3					Incident Wave Condition 4				
$D =$	1/8"		1/4"		$D =$	1/8"		1/4"	
$\Phi, \%$	$C_T$	$G_0$	$C_T$	$G_0$	$\Phi, \%$	$C_T$	$G_0$	$C_T$	$G_0$
40.31	0.58	1.46	0.72	2.93	40.31	0.69	2.39	0.85	4.77
29.61	0.50	1.07	0.59	1.51	29.61	0.58	1.75	0.72	2.46
22.67	0.32	0.61	0.45	0.98	22.67	0.42	0.99	0.61	1.59
16.08	0.25	0.49	0.31	0.61	16.08	0.39	0.80	0.46	0.99

The theoretical transmitted wave profile for the downstream region of a porous barrier was derived and can be described by Equation (13.2) as

$$\eta_2 = a \frac{2G_0}{2G_0 + 1} \cos(k_0 x - \omega t),$$

where  $a$  is the amplitude of the incident waves. By using the calibrated  $b$  values and the wave parameters (e.g.,  $k_0$ ,  $\omega$ , and  $\varepsilon$ ) from the incident wave conditions 3 and 4 considered for model validation, the theoretically derived transmitted wave profiles were developed. The

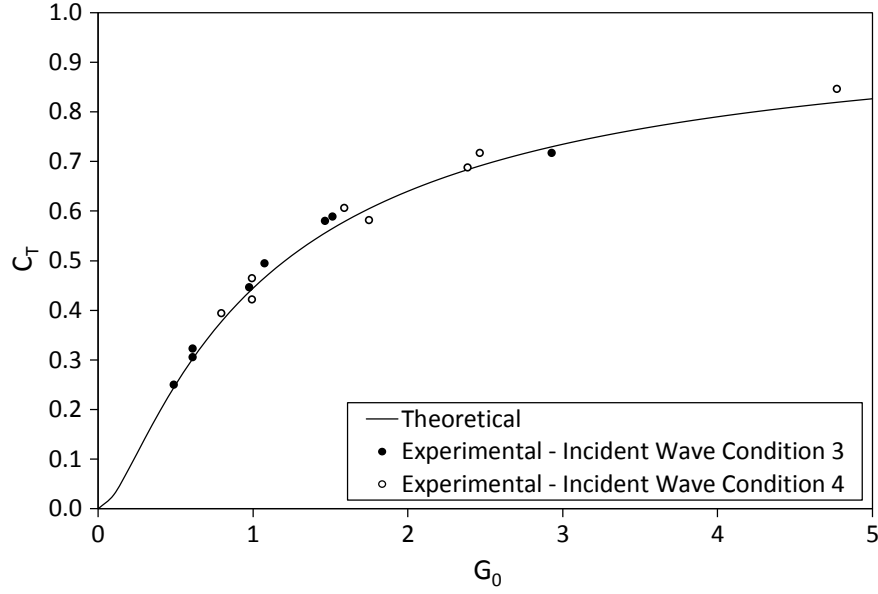


**Figure 13.10:** Comparisons of theoretical and experimental  $C_T$  values v.s.  $G_0$  calculated with calibrated  $b$  values under incident wave conditions 3 and 4.

comparisons between the theoretical and recorded wave profiles at the location of Gauge 2 (43.75 inches behind the screen) for the screens of 1/4 and 1/8 inches pore diameters with various porosities are shown in Figures 13.11 ~ 13.14 (Figures 13.11 and 13.12 for incident wave condition 3, Figures 13.13 and 13.14 for incident wave condition 4). In general, the wave heights and phases of the derived wave profiles agree well with the recorded transmitted wave profiles. It can also be observed that the fraction of incident wave energy transmitted through the screens decreases (reduction in transmitted wave height) as the porosities of the screens decrease (reduction in  $G_0$ ). When comparing between two screens with the same porosity, less incident wave energy gets transmitted through the screen with a smaller pore diameter, which suggests that pore diameter affects the transmission of wave energy. As discussed previously (Figure 13.9), incident waves with longer wavelength can pass through porous barriers more easily than waves with shorter wavelength. The reduction percentage of incident wave height can be defined as

$$\%_{red} = 100\left(1 - \frac{T_0}{I_0}\right), \quad (13.7)$$

and Table 13.4 summarizes the incident wave reduction percentages for the eight porous

screens under the incident wave conditions 3 (shorter waves) and 4 (longer waves). It is shown that greater wave reduction was induced by a screen with shorter incident waves. This experimental analysis also confirms the previous theoretical finding that wave attenuation is easier to achieve with waves of shorter wavelength.

**Table 13.4:** Wave reduction percentage comparisons.

$D =$	1/4"	1/4"	1/8"	1/8"
Incid. Wave ID	3	4	3	4
$k_0$ , rad/ft	4.91	1.51	4.91	1.51
$\Phi$ , %	Reduction, %	Reduction, %	Reduction, %	Reduction, %
40.31	15.3	8.0	23.8	17.0
29.61	23.3	15.3	29.6	23.7
22.67	33.2	22.1	43.1	35.0
16.08	44.7	31.8	50.0	37.2

### 13.3 WAVE TRANSFORMATION CAUSED BY A SUBMERGED CAVITY AND VISUALIZATION OF FLOW PATTERNS

The free surface elevations recorded at the specified gauge locations for selected cases of solitary waves propagating past a submerged trench have been reported in Chang et al. (2011) for comparisons with the results from a 2-D viscous flow model developed by solving the dimensionless stream function and vorticity equations given as

$$\nabla^2 \psi = -\omega \quad (13.8)$$

and

$$\frac{\partial \omega}{\partial T} + u \frac{\partial \omega}{\partial x} + v \frac{\partial \omega}{\partial y} = \frac{1}{R_e} \nabla^2 \omega, \quad (13.9)$$

where  $\psi$  = stream function,  $\omega$  = vorticity,  $\nabla^2$  is the Laplace operator,  $T$  = dimensionless time =  $\frac{t\sqrt{gh}}{h}$ ,  $u = \frac{\partial \psi}{\partial y}$ ,  $v = -\frac{\partial \psi}{\partial x}$ ,  $R_e = \frac{h\sqrt{gh}}{\nu}$  is the Reynolds number, and  $\nu$  is the kinematic viscosity of the fluid. This 2-D model solves the governing equations in a transient boundary-fitted grid system using the finite-analytic method. A two-step finite difference scheme is applied to solve the free surface boundary conditions. Detailed numerical formulations and

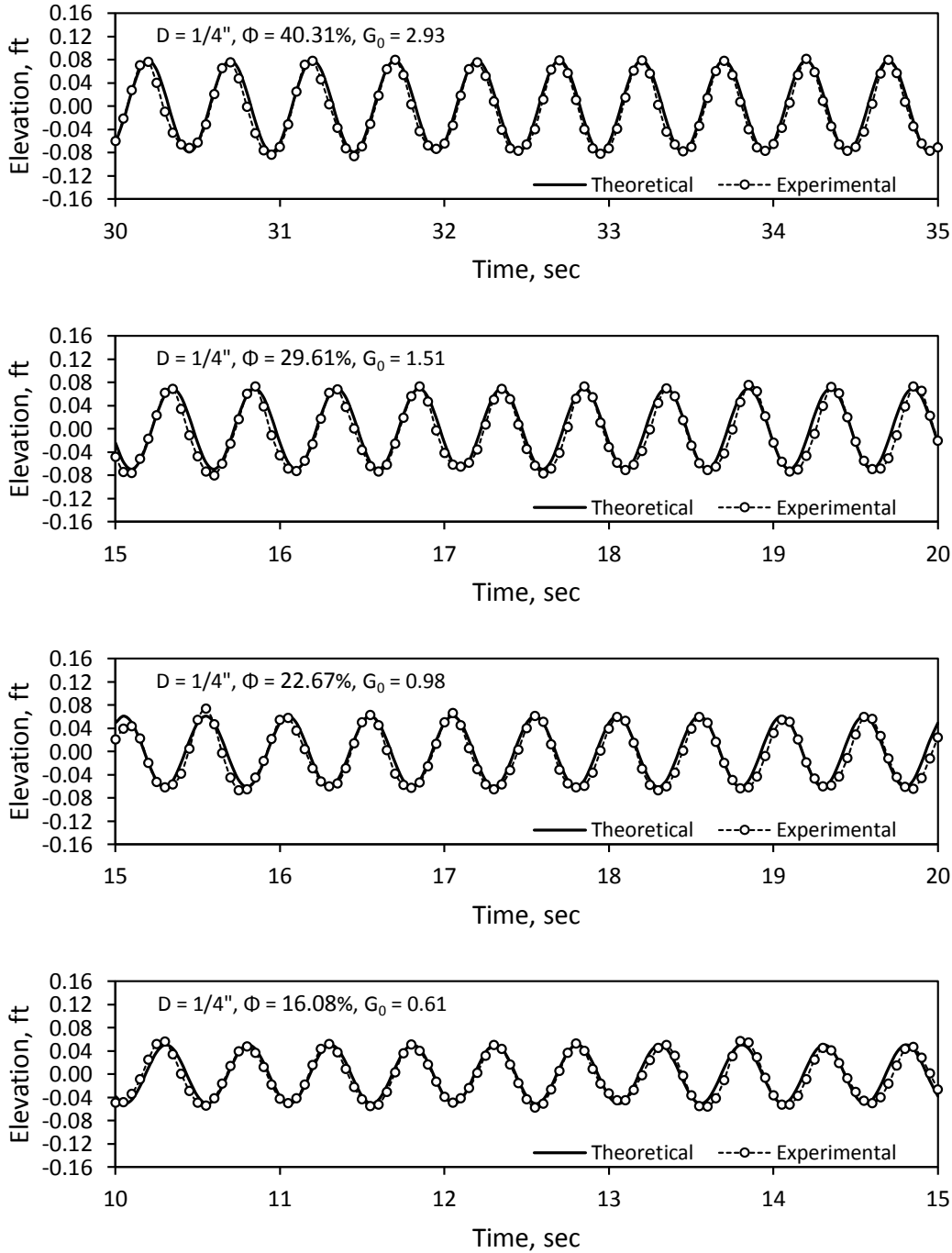


**Figure 13.11:** Transmitted wave profiles from screens of 0.25" pore diameter and porosities of 40.31%, 29.61%, 22.67%, and 16.08% (from top to bottom) under incident wave condition 3.

techniques can be found in Chang et al. (2011). In this results section, we focus through flow visualization to discuss the formation and development of induced vortices together with the trajectories and transporting distances of fluid particles under the action of solitary waves

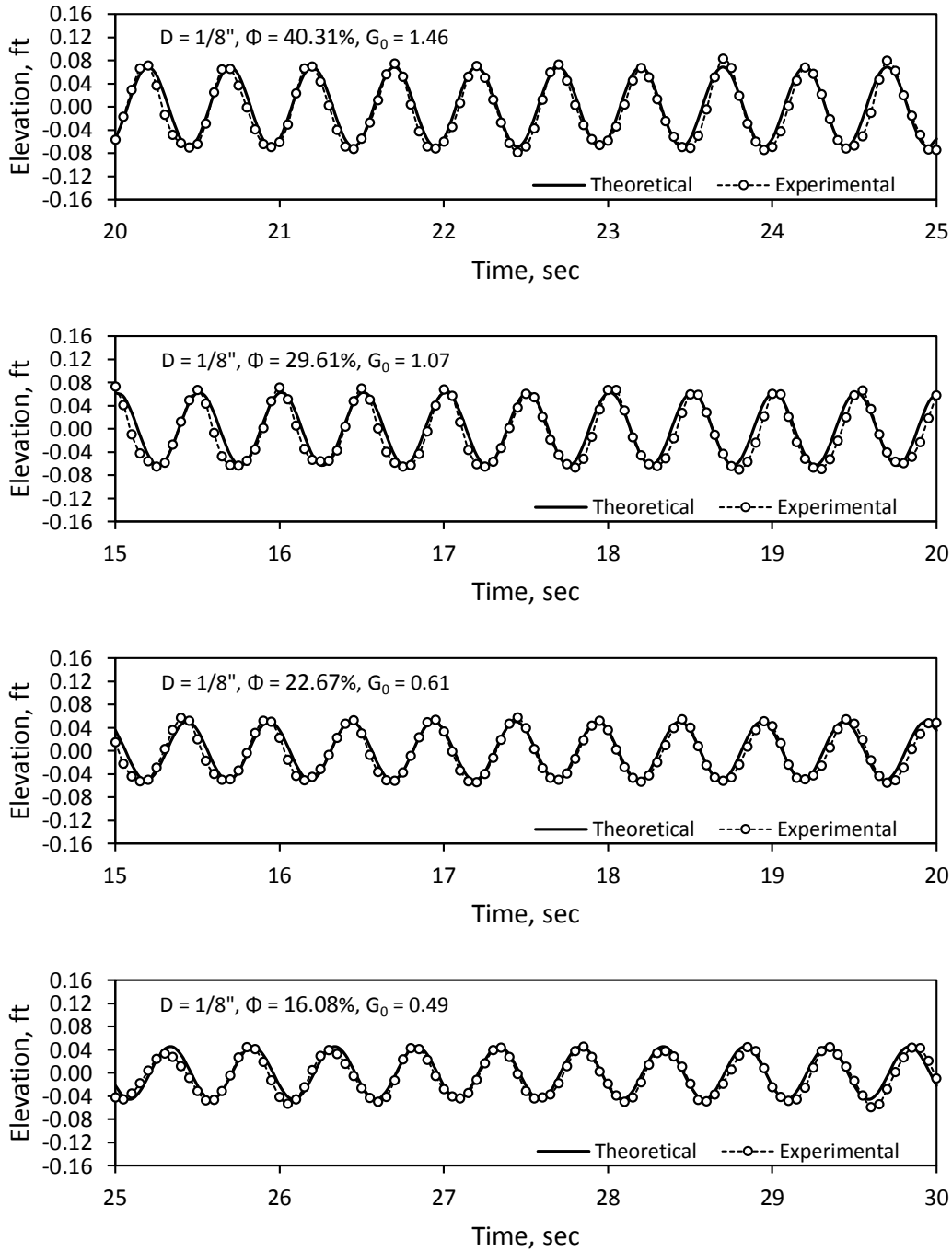


**Figure 13.12:** Transmitted wave profiles from screens of 0.125" pore diameter and porosities of 40.31%, 29.61%, 22.67%, and 16.08% (from top to bottom) under incident wave condition 3.

with or without a trench. Both the experimental and numerical results are presented.

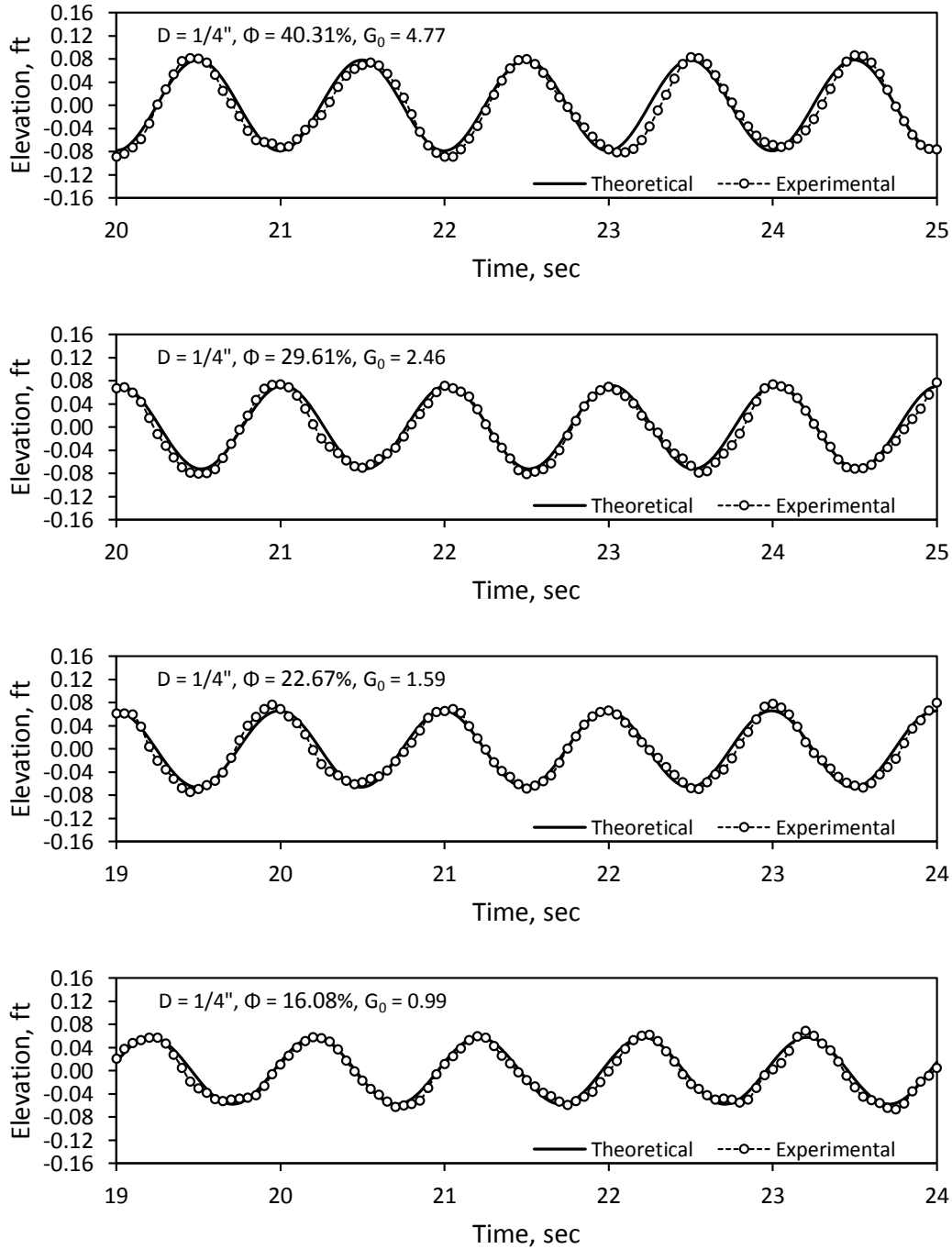


**Figure 13.13:** Transmitted wave profiles from screens of 0.25" pore diameter and porosities of 40.31%, 29.61%, 22.67%, and 16.08% (from top to bottom) under incident wave condition 4.

### 13.3.1 Flow Field Visualization

Visualization of dye enhanced flow patterns can assist the understanding of the physical process of fluid particles that are transported in and around a trench as a solitary wave

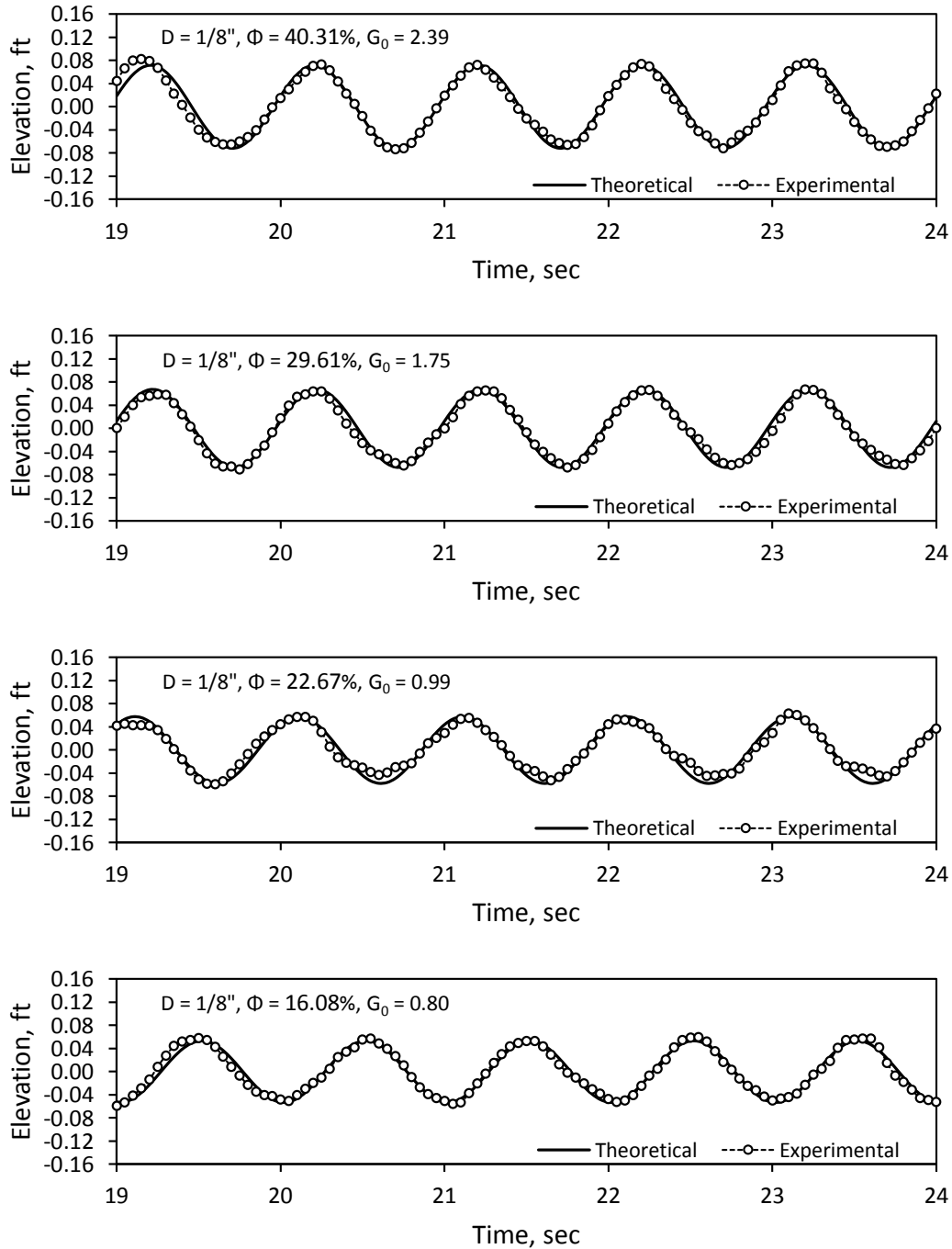


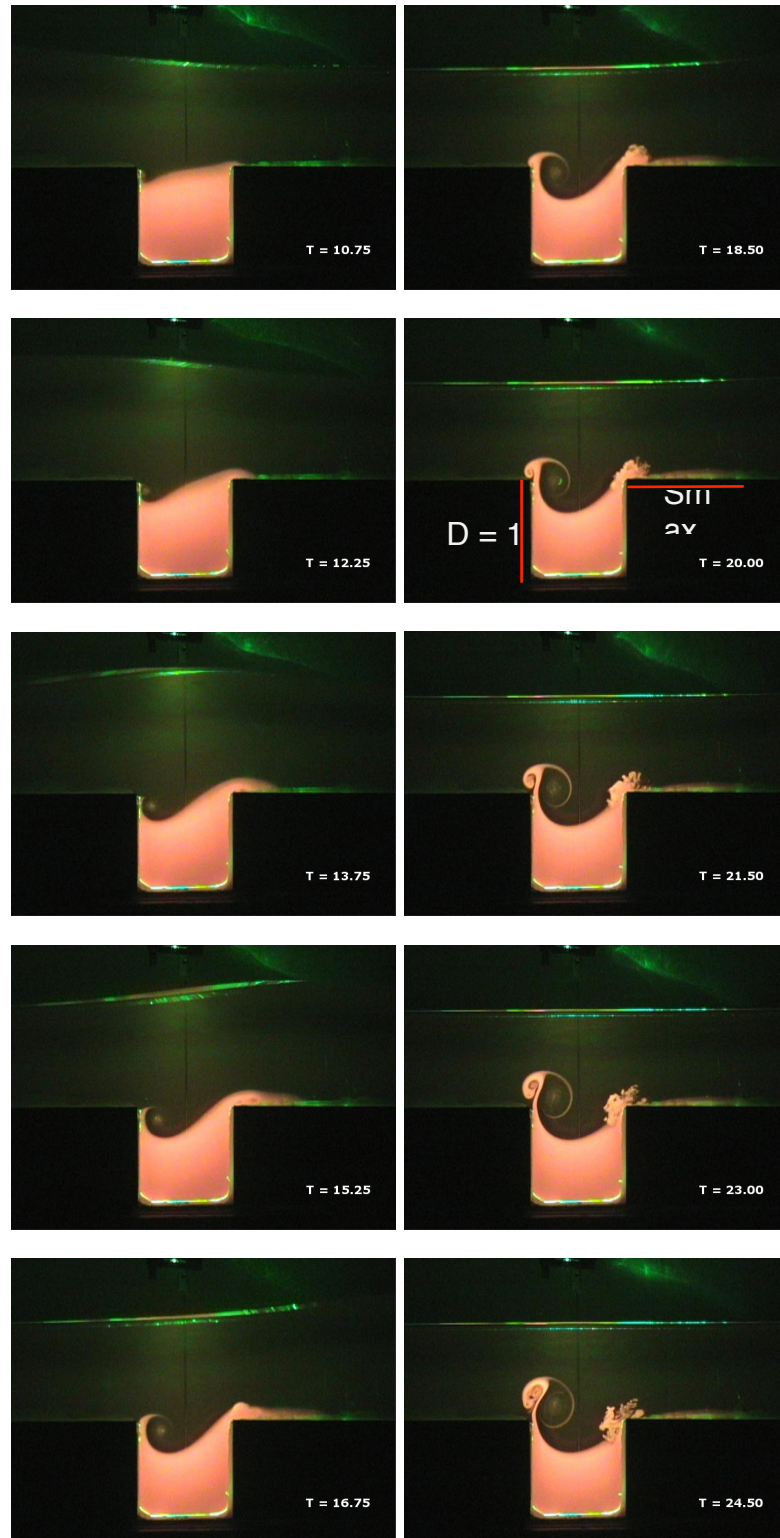
**Figure 13.14:** Transmitted wave profiles from screens of 0.125" pore diameter and porosities of 40.31%, 29.61%, 22.67%, and 16.08% (from top to bottom) under incident wave condition 4.

propagates past the depressed region. Considering the case of  $\alpha = 0.27$ ,  $D = 1$ , and  $W = 1$ , shown in Figure 13.15 is a sequence of images of flow patterns extracted from a recorded video describing the time evolution of the flow field and induced vortices around the trench

region. As an incident solitary wave propagates from left to right approaching the trench, the free surface elevation around the trench region gradually rises and accordingly the interface connecting the fluid layers above and within the trench experiences a gradual increase of the velocity and induced velocity gradient. The fluid particles above the interface push forwards while part of the fluid particles below the interface in return move backwards. As a result, a tilted interface of fluid particles is formed to follow for an initiation of a clockwise vortex at the leading edge of the trench.

In the region near the trailing edge of the trench, the forward moving fluid velocity carries the fluid particles including those from the lower trench layer towards downstream of the trench. As can be seen in Figure 13.15, the fluorescent dyed fluid is pushed out of the trench zone creating a long tail on the downstream acrylic floor. At time frames  $T = 15.25, 16.75, 18.50,$  and  $20.00$ , the vortex at the leading edge grows vertically and a constructed vortex pattern becomes more apparent while the downstream-transporting front continues to expand and more particles are entrained downstream. At the moment when the entire wave is about to pass the trench (e.g.,  $T = 20.00$ ), the downstream particle transporting distance nearly reaches the maximum ( $S_{max}$ ). Right after the wave has passed over, the fluid behind the wave begins to move towards the negative  $x$  direction. This reverse motion further enhances the growth of the clockwise vortex and circulation in the trench zone causing the withdrawal of fluid particles. A small portion of the fluid particles that have been transported out of the trench are shown to flow back into the trench, and a counterclockwise-circulating vortex appears adjacent to the clockwise-rolling vortex. The swirls continue to grow and rise until their eventual deformation near the free surface.

Considering a case with a larger trench opening, the visualization images showing the time evolution of the vortex pattern for  $\alpha = 0.27, D = 1,$  and  $W = 1.9$  are presented in Figure 13.16. The general fluid flow patterns and the formation and growth of the vortices are similar to those presented in Figure 13.15. However, the formed vortices around the leading edge of the trench, especially the clockwise vortex, is not as apparent as shown in the case of  $W = 1$  as a result of the weakened reverse fluid velocities for a larger opening.



Text

**Figure 13.15:** Images extracted from a recorded video showing time evolution of flow field and induced vortices for a solitary wave of  $\alpha = 0.27$  propagating past a trench with  $D = 1$  and  $W = 1$ .

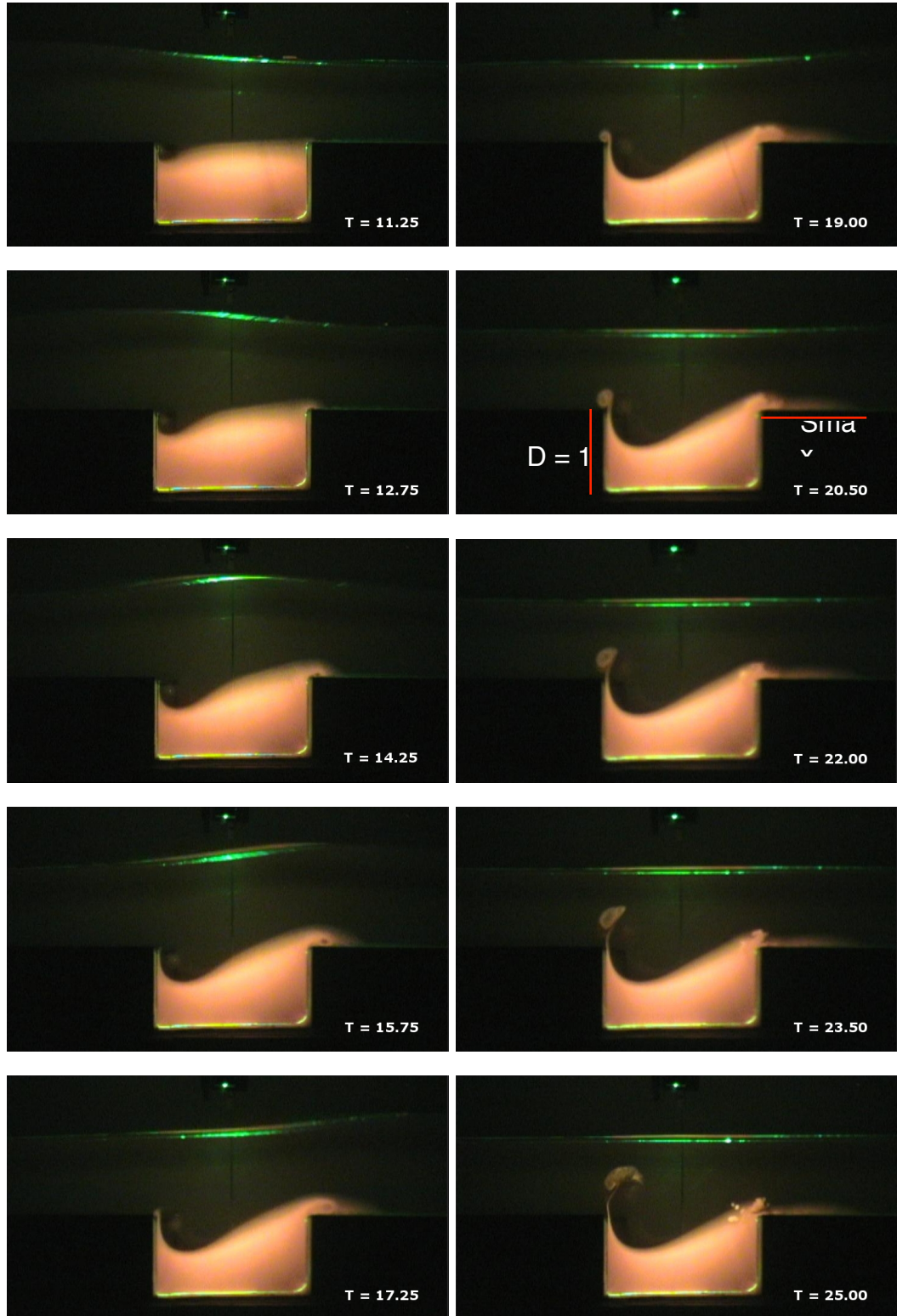


**Figure 13.16:** Images extracted from a recorded video showing time evolution of flow field and induced vortices for a solitary wave of  $\alpha = 0.27$  propagating past a trench with  $D = 1$  and  $W = 1.9$ .

### 13.3.2 Displacement of Moving Fluid Particles and Transport of Trench Contents

As shown in Figure 13.15, the downstream particle transporting distance can reach nearly the maximum value at the moment (e.g.,  $T = 20.00$ ) when the entire wave has almost passed the trench. Let's define the dimensionless maximum transporting distance as  $S_{max} = S_{max}^*/h$ . Before analyzing the effects of trench opening size and wave height on  $S_{max}$ , it is interesting to examine the particle trajectories under a solitary wave moving in a channel without a trench. Results from the performed dye tracing experiments for a solitary wave propagating over a trench can be used to check with the benchmark problems of particle trajectories for cases without a trench described by some of the analytical solutions. For solitary waves in the potential flow, the horizontal fluid velocities generally increase from the bottom to free surface. McCowan (1891) derived a formulation describing the depth-averaged trajectory of a fluid particle under the action of a solitary wave as

$$(\bar{\xi} - \beta)^2 + \bar{\eta}^2 + 2\beta\bar{\eta} \cot m(Z + \bar{\eta}) = \beta^2 \quad (13.10)$$

in which  $\bar{\xi}$  and  $\bar{\eta}$  are respectively the averaged displacements in the horizontal and vertical directions,  $Z$  is the particle's undisturbed original vertical position measured from the bottom of the fluid domain,  $\beta$  is the first approximation of wave expansion coefficient, and  $m$  is the effective wave number. The coefficient of  $\beta$  and  $m$  are given with approximated expressions as

$$\beta = 2\sqrt{\frac{\alpha}{3}} \quad (13.11)$$

and

$$m = \sqrt{3\alpha}. \quad (13.12)$$

Equation (13.10) can be simplified by neglecting the higher order term of  $\bar{\eta}^2$  and approximating  $Z + \bar{\eta} \approx Z$  as

$$(\bar{\xi} - \beta)^2 + 2\beta\bar{\eta} \cot mZ = \beta^2. \quad (13.13)$$

Equation (13.13) may be rearranged as

$$\bar{\eta} = \frac{[-(\bar{\xi} - \beta)^2 + \beta^2]}{(2\beta \cot mZ)}. \quad (13.14)$$

According to the characteristics of a solitary wave, the valid range of  $\bar{\xi}$  satisfies the condition described as  $0 \leq \bar{\xi} \leq 2\beta$  with  $\bar{\eta} \geq 0$ . When  $\bar{\eta} = 0$ , we have  $\bar{\xi} \in [0, 2\beta]$ . Therefore, the first-order approximation of the maximum horizontal displacement of a fluid particle is

$$\bar{\xi}_{max} = 2\beta = 4\sqrt{\frac{\alpha}{3}}. \quad (13.15)$$

This is equivalent to the solution of Longuet-Higgins (1981) derived by the fundamental solution of wave profile and wave celerity of a solitary wave with the concept of Bernoulli equation.

Equation (13.15) reflects an averaged maximum displacement of a moving fluid particle under the action of a propagating solitary wave. For a small amplitude solitary wave, Equation (13.15) may provide a good estimation on particle traveling distance. However, for a large amplitude wave, the difference of the horizontal displacement between particles positioned at the free surface and bottom of the fluid domain may not be negligible. As a test case, Figure 13.17 illustrates the trajectories of a free surface particle for a solitary wave with  $\alpha = 0.69$  propagating in a domain of uniform depth. The solid line denotes the experimental measurements by Longuet-Higgins (1981) while the circle symbols, presented at a dimensionless time interval of 0.05, represent the numerical results from the developed 2-D viscous flow model by Chang et al. (2011) as described previously. Generally, the experimental data and numerical results are in good agreement with a small deviation at the final stage of the motion, where the experimentally generated trailing waves for this extreme wave height condition may have caused the difference. It can be seen in Figure 13.17 that the vertical displacement can be up to 0.69 of the specified water depth,  $h$ , while the horizontal distance can reach about 3.0. The averaged horizontal displacement from Equation (13.15) is about 1.92, which is roughly 36% less than the measured horizontal displacement.

The maximum horizontal displacement of fluid particles,  $S_{max}$ , initially located at

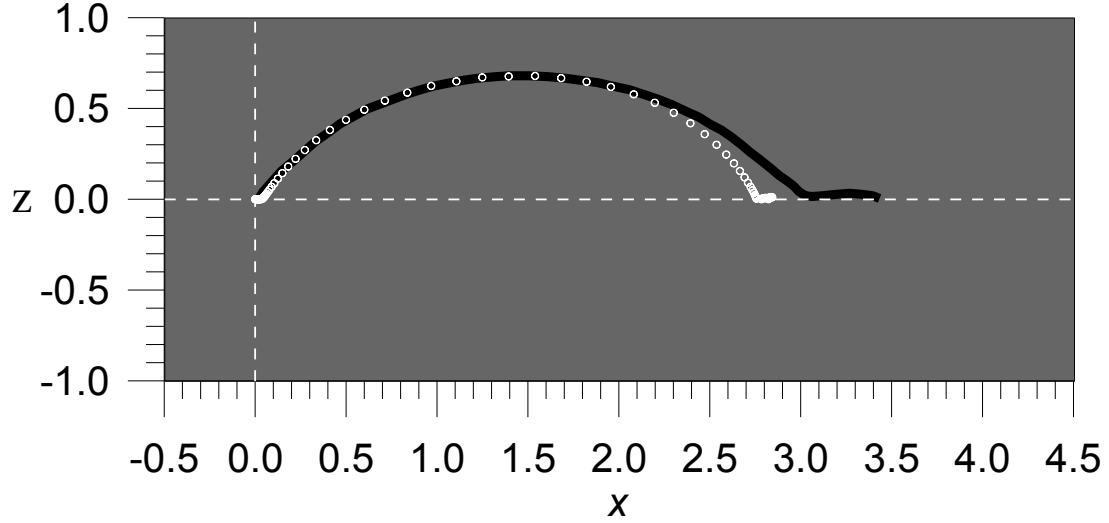


**Figure 13.17:** Trajectories of a free surface particle for a solitary wave propagating in a domain of uniform depth. Black line denotes the observed data from Longuet-Higgins (1981) and white circle symbols represent the result from the 2-D viscous flow model by Chang et al. (2011).

different vertical levels is one of the interesting kinematics to be examined. Results from various wave theories, numerical simulations, and experimental measurements showing the variations of  $S_{max}$  versus wave height,  $\alpha$ , for the fluid particles initially situated at the free surface or bottom of a fluid domain are presented in Figure 13.18. The Fenton's (1972) ninth order solutions shown in Figure 13.18 were obtained from the formulations given as

$$S_{max} \Big|_{bottom} = \sqrt{\frac{16\alpha}{3}} (1 + 0.375\alpha - 0.546979\alpha^2 - 0.0748352\alpha^3 - 0.0433862\alpha^4 - 0.0226978\alpha^5 - 0.0430576\alpha^6 - 0.0170864\alpha^7 - 0.362114\alpha^8) \quad (13.16)$$

and

$$S_{max} \Big|_{free\ surface} = \sqrt{\frac{16\alpha}{3}} (1 + 0.375\alpha + 0.253022\alpha^2 + 0.0537308\alpha^3 + 0.0860583\alpha^4 + 0.0511546\alpha^5 + 0.0636512\alpha^6 + 0.0572738\alpha^7 + 0.0724525\alpha^8). \quad (13.17)$$

The results from the 2-D model by Chang et al. (2011) for an inviscid fluid are in good agreement with Fenton's solutions for both the bottom and free surface particles, especially when  $\alpha < 0.5$ . For the free surface particles, the 2-D flow model produces slightly

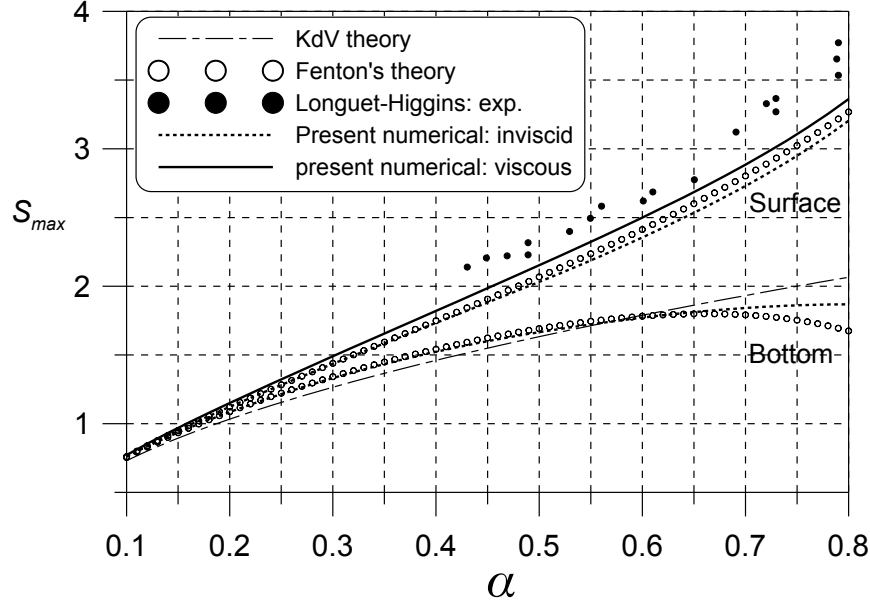


**Figure 13.18:** Variations of maximum transported distance  $S_{max}$  versus dimensionless wave height  $\alpha$  for fluid particles initially positioned at the free surface and bottom. Dashed line: KdV first order theory; Hollow circle: Fenton's (1972) ninth-order analytical solution; Solid circle: experimental data from Longuet-Higgins (1981); Dotted line: 2-D inviscid model; Solid line: 2-D viscous model.

greater values of  $S_{max}$  for the case of a viscous fluid than those considering an inviscid fluid. The viscous solutions are shown to be slightly less than the experimental data of Longuet-Higgins (1981). As explained above for the comparisons in Figure 13.17, this may be a result caused by the difference between the theoretically and experimentally generated waves. The increased scattering of the measured data is shown within the region of  $\alpha > 0.7$ . The results using the KdV theory, which are similar to the solutions from Equation (13.13), are also included in Figure 13.18 to show the values of vertically averaged horizontal displacement. As shown in Figure 13.18, when  $\alpha < 0.25$ , the horizontal displacements of moving particles either at the free surface or at the bottom do not show significant difference. However, for cases with relative large wave heights (e.g.,  $\alpha > 0.3$ ), as expected the free surface displacements are shown to deviate with greater values from the bottom displacements.

For the case with a submerged trench, the fluid particles around the interface especially near the trailing edge of the trench are subject to be transported downstream by the wave induced horizontal motion when a solitary wave passes over. The observed dye tracing distance measured from the trailing edge of the trench can be used to examine the horizontally

transported distance, or displacement,  $S^*$ , of a moving particle, as shown in Figure 13.19. The value of  $S^*$  is primarily controlled by the wave induced motion at  $z = -h$  ( $z = 0$  plane is at the undisturbed free surface), which in principle is close to the displacement of bottom particles in a domain of uniform water depth  $h$  (without a trench). The variations of  $S_{max}$  (with a trench) versus  $\alpha$  for cases in combinations of  $W = 0.5, 1.0, 2.0$  and  $D = 0.5, 1.0$  were computed using the 2-D flow model and presented in Figure 13.20. Here,  $S_{max}$  is the maximum traveling distance of the transported fluid particles along the channel bottom downstream of the trench. The results indicate that the change in trench depth,  $D$ , has an insignificant effect on the maximum displacement of the fluid particles. Even the increase of the trench opening,  $W$ , does not affect  $S_{max}$  much. The roughly estimated maximum displacement from the measurements taken in this study for the cases of  $\alpha = 0.27$ ,  $W = 1$ , and  $D = 1$  (at  $T = 20$ , Figure 13.15) as well as  $\alpha = 0.27$ ,  $W = 1.9$  and  $D = 1$  (at  $T = 22$ , Figure 13.16) are also included in Figure 13.20 for comparison purposes. The measured data are within the ranges of the results obtained from the numerical simulations.

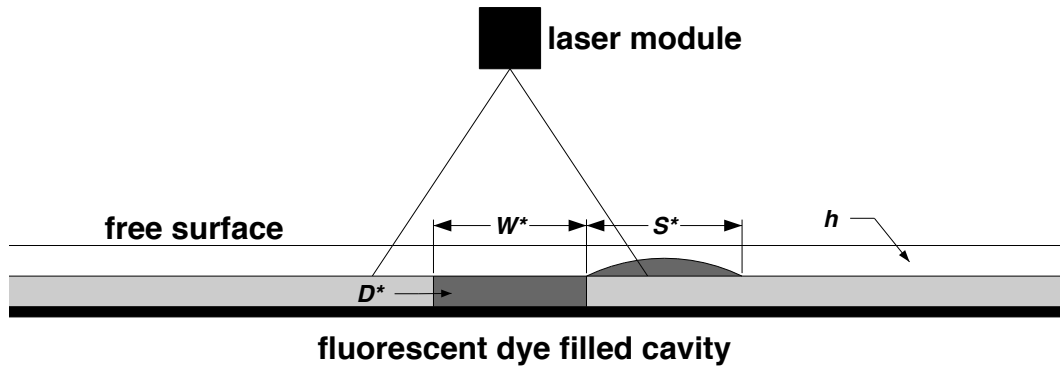


**Figure 13.19:** Fluorescent dye filled submerged cavity.

As a solitary wave propagates past a submerged trench, part of the fluid particles within the trench is transported outside through the induced vortices and carrying of the horizontal velocities near the interface. The computed results showing the percentage of the particles moved away from a trench having the dimensions of  $W = 0.5$  and  $D = 0.5$  are presented in Figure 13.21. Three different wave height conditions are examined. A trench sketch is drawn, and the white space denoted as  $A_{out}$  represents the total amount of the particles transported outside of the trench under the conditions of  $\alpha = 0.6$ ,  $W = 0.5$ ,

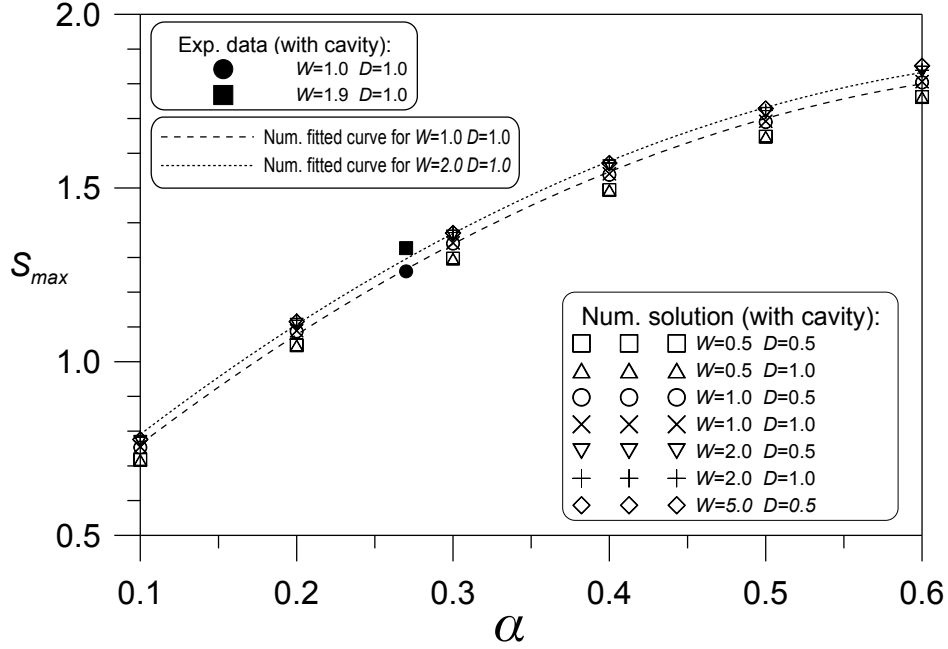


**Figure 13.20:** Variations of  $S_{max}$  versus  $\alpha$  for cases in combinations of  $W = 0.5, 1.0, 2.0$  and  $D = 0.5, 1.0$  and experimentally estimated data from limited cases.

$D = 0.5$ , and  $T = 50$ . The determination of  $A_{out}$  can be important to understanding the mechanism of trench scouring or particle transport. The results in Figure 13.21 reveal that the values of  $A_{out}$  after a long simulation time nearly reach steady state, indicating a negligible transport rate at later times. The incident wave height,  $\alpha$ , is shown to have a greater influence on particle disturbance and therefore affects the total amount of the transported fluid particles. With the increase of  $\alpha$ , the values of  $A_{out}$  increase. As can be seen, for example, the incident wave heights of  $\alpha = 0.2$  and  $\alpha = 0.6$  can entrain nearly 40% and 70%, respectively, of the particles that are initially settled in the trench. Therefore, any materials that are accumulated in a submerged trench can be disturbed and transported, especially by large wave motions, to the surrounding areas and as a result raise the concerns of environmental impact.

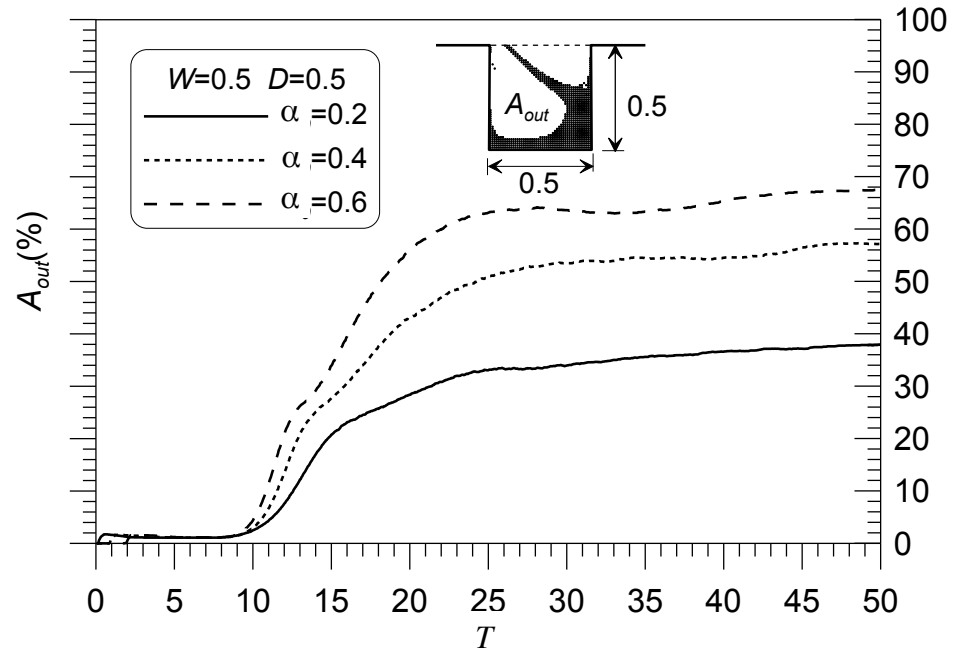


**Figure 13.21:** Time variations of particle removal percentage from a trench by solitary waves of various wave heights.

## Chapter 14

### Conclusions and Future Studies

In this part of the research, head loss induced due to flows passing through porous screens was investigated. The effects of screen pore size, porosity, and angle of inclination on head loss were experimentally analyzed. An average of ten flow rate conditions ranging from 0.3 to 2.2 ft<sup>3</sup>/s with a 0.2 ft<sup>3</sup>/s flow increment were established and run through the screens with pore diameters of 1/4 and 1/8 inches and porosities of 40.31%, 29.61%, 22.67%, and 16.08%. During the tests, the screens were also positioned at three angles of inclination, 90°, 75°, and 63°. Based on the results from over one hundred tests, it was found that head loss in general was linearly proportional to the square of averaged upstream flow velocity. Less head loss was induced with the screens of greater porosities under the same flow rate condition. The effect of pore size on head loss was not significant when comparing between the screens of pore diameters of 1/4 and 1/8 inches and porosity of 40.31%. In addition, less head loss was induced when the screen was positioned at a lower angle of inclination under the same flow rate condition. Finally, two linear models, which could be used to predict head loss, were deduced from the relationships between head loss and the square of averaged pore velocity. The averaged pore velocity incorporates the effects of screen porosity and angle of inclination, which makes the models easy to apply. For future studies, the inclusion of the effect of screen pore size into the calculation of averaged pore velocity is recommended such that a single universal linear model may be developed to conveniently predict head loss caused by a porous screen with the screen properties (e.g., pore size, porosity, angle of inclination) and upstream averaged flow velocity known.

Wave transformation caused by porous barriers was the second topic studied analytically and experimentally. The solutions in terms of velocity potential for the propagation and transmission of a monochromatic wave through a porous barrier were derived based on the linear wave theory. Darcy's law was adopted as a boundary condition to interconnect

the wave motions on both sides of the barrier. The porous effect of the barrier was represented by the porous effect parameter,  $G_0$ , which is dependent on the screen material constant,  $b$ . A series of theoretical relationships between the coefficient of transmission,  $C_T$ , and other parameters such as  $G_0$  and  $k_0$  were developed. These relationships showed that more incident wave energy would be transmitted as the porous effect of the barrier increased. For applications that require energy dissipation, porous barriers that yield  $G_0$  values close or equal to 0.5 would be most efficient in dissipating wave energy. Lastly, incident waves with a longer wavelength would be harder to attenuate by a porous barrier as compared to shorter wavelength waves. Experiments were carried out to validate the theoretical findings. A piston-type wave maker system was built in a flume for generating various incident wave conditions. The porous screens that were used in the head loss study were used as porous barriers. A total of four incident wave conditions were generated. The values of the material constant,  $b$ , were calibrated for the eight screens using two of the incident wave conditions. The calibrated  $b$  values then were verified with the remaining two incident wave conditions. The derived transmitted wave profiles were compared against the recorded wave profiles, and a good agreement was demonstrated. In addition, the developed theoretical relationships associated with  $C_T$  were cross validated by the experimental data. The theoretical curves and experimental data agreed well with each other indicating that the derived solutions and the use of Darcy's law as a boundary condition were valid. For future studies, it is recommended to test the proposed theories with more incident wave conditions (i.e., different wave height, wavelength, etc.) such that additional data can be collected to establish a wider range of  $G_0$  values and improve the accuracy of the calibrated  $b$  values. The study can also be extended to the case of non-linear wave conditions (e.g., solitary waves) to confirm whether the values of  $b$  are still valid as material constants under non-linear wave conditions.

The last topic focused on the visualization of vortices and flow patterns induced by solitary waves propagating over a submerged trench. As a solitary wave approaches the trench, the interface connecting the fluid layers above and inside of the trench experiences an increase in velocity and induced velocity gradient causing the fluid particles in the trench to be transported downstream. Vortices near the leading edge of the trench are also formed.

An up-leveled acrylic made floor consisting of two movable sections that were separated by an adjustable opening was placed in the wave flume to simulate the submerged trench. Solitary waves with various wave heights were generated by the wave maker system. The PLIF technique was used to illuminate the fluorescent dye enhanced flow features within and near the trench, while the time evolution of the features were recorded with a video camera. Images at specific instants were extracted and processed for analysis. The growth of the induced vortices and the process of particle entrainment were observed. The maximum particle transporting distance estimated from the extracted images were compared to the values predicted by models that are based on different theories. For future studies, the PLIF technique can be applied to visualize flow features that are induced by water waves propagating over other types of structures, such as submerged breakwaters.

## References

- Andrieu, H., Creutin, J. D., Delrieu, G., & Faure, D. (1997). Use of a Weather Radar for the Hydrology of a Mountainous Area. Part I: Radar Measurement Interpretation. *Journal of Hydrology*, *193*(1–4), 1–25.
- Austin, P. M. (1987). Relation Between Measured Radar Reflectivity and Surface Rainfall. *Monthly Weather Review*, *115*(5), 1053–1070.
- Berne, A., & Krajewski, W. F. (2013). Radar for Hydrology: Unfulfilled Promise or Unrecognized Potential? *Advances in Water Resources*, *51*, 357–366.
- Biggs, E. M., & Atkinson, P. M. (2011). A Comparison of Gauge and Radar Precipitation Data for Simulating an Extreme Hydrological Event in the Severn Uplands, UK. *Hydrological Processes*, *25*(5), 795–810.
- Borga, M. (2002). Accuracy of Radar Rainfall Estimates for Streamflow Simulation. *Journal of Hydrology*, *267*(1–2), 26–39.
- Chang, C.-H., Chu, T., Wang, K.-H., & Tang, C.-J. (2011). Study of Solitary-wave-induced Fluid Motions and Vortices in a Cavity Using a Two-dimensional Viscous Flow Model. *Journal of Engineering Mechanics*, *137*(11), 769–778.
- Chen, C.-J., Naseri-Neshat, H., & Ho, K.-S. (1981). Finite-analytic Numerical Solution of Heat Transfer in Two-dimensional Cavity Flow. *Numerical Heat Transfer*, *4*(2), 179–197.
- Cho, I. H., & Kim, M. H. (2008). Wave Absorbing System Using Inclined Perforated Plates. *Journal of Fluid Mechanics*, *608*, 1–20.
- Christensen, R. (1990). *Linear Models for Multivariate, Time Series, and Spatial Data*. New York: Springer Verlag.
- Chu, H.-J., Lin, Y.-P., Huang, C.-W., Hsu, C.-Y., & Chen, H.-Y. (2010). Modelling the Hydrologic Effects of Dynamic Land-use Change Using a Distributed Hydrologic Model and a Spatial Land-use Allocation Model. *Hydrological Processes*, *24*(18), 2538–2554.

- Chwang, A. T. (1983). A Porous Wavemaker Theory. *Journal of Fluid Mechanics*, *132*, 395–406.
- Chwang, A. T., & Chan, A. T. (1998). Interaction Between Porous Media and Wave Motion. *Annual Review of Fluid Mechanics*, *30*, 53–84.
- Chwang, A. T., & Dong, Z. (1984). Wave-trapping Due to a Porous Plate. *Proceedings of 15 ONR Symposium on Naval Hydrodynamics*, 407–414.
- Cole, S. J., & Moore, R. J. (2009). Distributed Hydrological Modelling Using Weather Radar in Gauged and Ungauged Basins. *Advances in Water Resources*, *32*(7), 1107–1120.
- Constantin, A., & Villari, G. (2008). Particle Trajectories in Linear Water Waves. *Journal of Mathematical Fluid Mechanics*, *10*, 1–18.
- Creutin, J. D., Andrieu, H., & Faure, D. (1997). Use of a Weather Radar for the Hydrology of a Mountainous Area. Part II: Radar Measurement Validation. *Journal of Hydrology*, *193*(1–4), 26–44.
- Dalrymple, R. A., Losada, M. A., & Martin, P. A. (1991). Reflection and Transmission from Porous Structures under Oblique Wave Attack. *Journal of Fluid Mechanics*, *224*, 625–644.
- Darwiche, M. K. M., Williams, A. N., & Wang, K.-H. (1994). Wave Interaction with Semi-porous Cylindrical Breakwater. *Journal of Waterway, Port, Coastal and Ocean Engineering*, *120*(4), 382–403.
- Dolciné, L., Andrieu, H., & French, M. N. (1997). Rainfall Forecasting in a Mountainous Region Using a Weather Radar and Ground Meteorological Observations. *Physics and Chemistry of the Earth*, *22*(3–4), 247–252.
- Doviak, R. J. (1983). A Survey of Radar Rain Measurement Techniques. *Journal of Climate and Applied Meteorology*, *22*(5), 832–849.
- Duncan, M. R., Austin, B., Fabry, F., & Austin, G. L. (1993). The Effect of Gauge Sampling Density on the Accuracy of Streamflow Prediction for Rural Catchments. *Journal of Hydrology*, *142*(1–4), 445–476.
- Dutta, D., & Nakayama, K. (2009). Effects of Spatial Grid Resolution on River Flow and Surface Inundation Simulation by Physically Based Distributed Modelling Approach. *Hydrological Processes*, *23*(4), 534–545.

- Ehret, U. (2003). *Rainfall and Flood Nowcasting in Small Catchments Using Weather Radar* (Doctoral dissertation). Universität Stuttgart.
- Evans, D. V. (1990). The Use of Porous Screens as Wave Dampers in Narrow Wave Tanks. *Journal of Engineering Mathematics*, 24(3), 203–212.
- Fang, Z., Bedient, P. B., Benavides, J., & Zimmer, A. L. (2008). Enhanced Radar-based Flood Alert System and Floodplain Map Library. *Journal of Hydrologic Engineering*, 13(10), 926–938.
- Fenton, J. (1972). A Ninth-order Solution for the Solitary Wave. *Journal of Fluid Mechanics*, 53, 257–271.
- Florie, C. J. L., & Hoek, M. J. v. d. (1981). Irreversible Energy Losses of Flow Through Porous and Perforated Plates. *Nuclear Engineering and Design*, 68(2), 147–152.
- Fulton, R. A., Breidenbach, J. P., Seo, D.-J., Miller, D. A., & O'Bannon, T. (1998). The WSR-88D Rainfall Algorithm. *Weather and Forecasting*, 13, 377–395.
- Goda, K. (1979). A Multistep Technique with Implicit Difference Schemes for Calculating Two- or Three-dimensional Cavity Flows. *Journal of Computational Physics*, 30(1), 76–95.
- Goovaerts, P. (1997). *Geostatistics for Natural Resources Evaluation*. New York: Oxford University Press.
- Goovaerts, P. (2000). Geostatistical Approaches for Incorporating Elevation into the Spatial Interpolation of Rainfall. *Journal of Hydrology*, 228(1–2), 113–129.
- Grimshaw, R. (1971). The Solitary Wave in Water of Variable Depth. Part 2. *Journal of Fluid Mechanics*, 46, 611–622.
- Haberlandt, U. (2007). Geostatistical Interpolation of Hourly Precipitation from Rain Gauges and Radar for a Large-scale Extreme Rainfall Event. *Journal of Hydrology*, 332(1–2), 144–157.
- Hengl, T. (2009). *A Practical Guide to Geostatistical Mapping* (2nd ed.). Amsterdam: University of Amsterdam.
- Hengl, T., Heuvelink, G. B. M., & Stein, A. (2003). *Comparison of Kriging with External Drift and Regression-kriging* (Tech. Rep.). ITC. Retrieved from [http://www.itc.nl/library/Academic\\_output/](http://www.itc.nl/library/Academic_output/)

- Ho, J., Coonrod, J., Hanna, L. J., & Mefford, B. W. (2011). Hydrodynamic Modelling Study of a Fish Exclusion System for a River Diversion. *River Research and Applications*, 27(2), 184–192.
- Hossain, F., Anagnostou, E. N., Dinku, T., & Borga, M. (2004). Hydrological Model Sensitivity to Parameter and Radar Rainfall Estimation Uncertainty. *Hydrological Processes*, 18(17), 3277–3291.
- Hu, H. M., & Wang, K.-H. (2004). A Hybrid Finite-analytic Algorithm for Solving Three-dimensional Advection-diffusion Equations. *International Journal of Computational Methods*, 1(3), 407–430.
- Huang, L. H., & Chao, H. I. (1992). Reflection and Transmission of Water Wave by Porous Breakwater. *Journal of Waterway, Port, Coastal and Ocean Engineering*, 118(5), 437–452.
- Huff, F. A. (1970). Sampling Errors in Measurement of Mean Precipitation. *Journal of Applied Meteorology*, 9, 35–44.
- Iwatsu, R., Ishii, K., Kawamura, T., Kuwahara, K., & Hyun, J. M. (1989). Numerical Simulation of Three-dimensional Flow Structure in a Driven Cavity. *Fluid Dynamics Research*, 5(3), 173–189.
- Jorgeson, J., & Julien, P. (2005). Peak Flow Forecasting with Radar Precipitation and the Distributed Model CASC2D. *Water International*, 30(1), 40–49.
- Khakbaz, B., Imam, B., Hsu, K., & Sorooshian, S. (2012). From Lumped to Distributed via Semi-distributed: Calibration Strategies for Semi-distributed Hydrologic Models. *Journal of Hydrology*, 418–419, 61–77.
- Krajewski, W. F. (1987). Cokriging Radar-rainfall and Rain Gage Data. *Journal of Geophysical Research*, 92(D8), 9571–9580.
- Krämer, S., & Verworn, H.-R. (2009). Improved Radar Data Processing Algorithms for Quantitative Rainfall Estimation in Real Time. *Water Science and Technology*, 60(1), 175–184.
- Krige, D. G. (1951). A Statistical Approach to Some Basic Mine Valuation Problems on the Witwatersrand. *Journal of the Chemical, Metallurgical and Mining Society of South Africa*, 52(6), 119–139.

- Laws, E. M., & Livesey, J. L. (1978). Flow Through Screens. *Annual Review of Fluid Mechanics*, 10, 247–266.
- Lloyd, C. D. (2005). Assessing the Effect of Integrating Elevation Data into the Estimation of Monthly Precipitation in Great Britain. *Journal of Hydrology*, 308(1–4), 128–150.
- Longuet-Higgins, M. S. (1981). Trajectories of Particles at the Surface of Steep Solitary Waves. *Journal of Fluid Mechanics*, 110, 239–247.
- Looper, J. P., Vieux, B. E., & Moreno, M. A. (2012). Assessing the Impacts of Precipitation Bias on Distributed Hydrologic Model Calibration and Prediction Accuracy. *Journal of Hydrology*, 418–419, 110–122.
- Madsen, P. A. (1983). Wave Reflection from a Vertical Permeable Wave Absorber. *Coastal Engineering*, 7, 381–396.
- Mandapaka, P. V., Villarini, G., Seo, B.-C., & Krajewski, W. F. (2010). Effect of Radar-rainfall Uncertainties on the Spatial Characterization of Rainfall Events. *Journal of Geophysical Research*, 115(D17), D17110.
- Matheron, G. (1969). *Le Krigeage Universel* (Vol. 1). Fontainebleau: Cahiers du Centre de Morphologie Mathématique, École des Mines de Paris.
- McCowan, J. (1891). On the Solitary Wave. *The London, Edinburgh, and Dublin Philosophical Magazine and Journal of Science*, 32(5), 45–58.
- Odeh, I. O. A., McBratney, A. B., & Chittleborough, D. J. (1994). Spatial Prediction of Soil Properties from Landform Attributes Derived from a Digital Elevation Model. *Geoderma*, 63(3–4), 197–214.
- Odeh, I. O. A., McBratney, A. B., & Chittleborough, D. J. (1995). Further Results on Prediction of Soil Properties from Terrain Attributes: Heterotopic Cokriging and Regression-kriging. *Geoderma*, 67(3–4), 215–226.
- Orasi, A., Lasinio, G. J., & Ferrari, C. (2009). Comparison of Calibration Methods for the Reconstruction of Space-time Rainfall Fields During a Rain Enhancement Experiment in Southern Italy. *Environmetrics*, 20(7), 812–834.
- Paudel, M., Nelson, E. J., Downer, C. W., & Hotchkiss, R. (2011). Comparing the Capability of Distributed and Lumped Hydrologic Models for Analyzing the Effects of Land Use Change. *Journal of Hydroinformatics*, 13(3), 461–473.

- Price, R. K. (1971). Bottom Drift for the Solitary Wave. *Journal of Geophysical Research*, 76(6), 1600–1602.
- Pritchard, D., & Hogg, A. J. (2003). On Fine Sediment Transport by Long Waves in the Swash Zone of a Plane Beach. *Journal of Fluid Mechanics*, 493, 255–275.
- R Core Team. (2013). *R: a Language and Environment for Statistical Computing*. Vienna, Austria: R Foundation for Statistical Computing.
- Russo, F., Napolitano, F., & Gorgucci, E. (2005). Rainfall Monitoring Systems over an Urban Area: the City of Rome. *Hydrological Processes*, 19(5), 1007–1019.
- Sander, J., & Hutter, K. (1991). On the Development of the Theory of the Solitary Wave. A Historical Essay. *Acta Mechanica*, 86, 111–152.
- Santiago, C. R. C., Chu, T., & Wang, K.-H. (2007). *Study of the Head Loss Associated with a Fluid Flowing Through a Porous Screen* (Tech. Rep.). Houston: University of Houston.
- Schuermans, J. M., Bierkens, M. F. P., Pebesma, E. J., & Uijlenhoet, R. (2007). Automatic Prediction of High-resolution Daily Rainfall Fields for Multiple Extents: the Potential of Operational Radar. *Journal of Hydrometeorology*, 8(6), 1204–1224.
- Severino, E., & Alpuim, T. (2005). Spatiotemporal Models in the Estimation of Area Precipitation. *Environmetrics*, 16(8), 773–802.
- Sharif, H. O., Hassan, A. A., Bin-Shafique, S., Xie, H., & Zeitler, J. (2010). Hydrologic Modeling of an Extreme Flood in the Guadalupe River in Texas. *Journal of the American Water Resources Association*, 46(5), 881–891.
- Sharif, H. O., Yates, D., Roberts, R., & Mueller, C. (2006). The Use of an Automated Nowcasting System to Forecast Flash Floods in an Urban Watershed. *Journal of Hydrometeorology*, 7(1), 190–202.
- Silverman, B. A., Rogers, L. K., & Dahl, D. (1981). On the Sampling Variance of Raingage Networks. *Journal of Applied Meteorology*, 20, 1468–1478.
- Steiner, M., Smith, J. A., Burges, S. J., Alonso, C. V., & Darden, R. W. (1999). Effect of Bias Adjustment and Rain Gauge Data Quality Control on Radar Rainfall Estimation. *Water Resources Research*, 35(8), 2487–2503.

- Stellman, K. M., Fuelberg, H. E., Garza, R., & Mullusky, M. (2001). An Examination of Radar and Rain Gauge-derived Mean Areal Precipitation over Georgia Watersheds. *Weather and Forecasting*, *16*(1), 133–144.
- Thiessen, A. H., & Alter, J. C. (1911). Precipitation Averages for Large Areas. *Monthly Weather Review*, *39*(7), 1082–1084.
- Ting, F. C. K. (1994). Wave Interaction with Fluid Mud in Rectangular Trench. *Journal of Waterway, Port, Coastal and Ocean Engineering*, *120*(2), 154–178.
- Vieux, B. E., Park, J.-H., & Kang, B. (2009). Distributed Hydrologic Prediction: Sensitivity to Accuracy of Initial Soil Moisture Conditions and Radar Rainfall Input. *Journal of Hydrologic Engineering*, *14*(7), 671–689.
- Vischel, T., Pegram, G. G. S., Sinclair, S., Wagner, W., & Bartsch, A. (2008). Comparison of Soil Moisture Fields Estimated by Catchment Modelling and Remote Sensing: a Case Study in South Africa. *Hydrology and Earth System Sciences*, *12*(3), 751–767.
- Wang, G., & Xu, Z. (2011). Assessment on the Function of Reservoirs for Flood Control During Typhoon Seasons Based on a Distributed Hydrological Model. *Hydrological Processes*, *25*(16), 2506–2517.
- Wang, K.-H., & Ren, X. (1993). Water Waves on Flexible and Porous Breakwaters. *Journal of Engineering Mechanics*, *119*(5), 1025–1047.
- Wang, K.-H., & Ren, X. (1994). Wave Interaction with a Concentric Porous Cylinder System. *Ocean Engineering*, *21*(4), 343–360.
- Wilson, J. W., & Brandes, E. A. (1979). Radar Measurement of Rainfall—a Summary. *Bulletin of the American Meteorological Society*, *60*(9), 1048–1058.
- Wu, L., Wang, B., & Geng, S. (2005). Growing Typhoon Influence on East Asia. *Geophysical Research Letters*, *32*(18), L18703.
- Yeh, H. H., & Shrestha, M. (1989). Free-surface Flow Through Screen. *Journal of Hydraulic Engineering*, *115*(10), 1371–1385.
- Yip, T. L., & Chwang, A. T. (2000). Perforated Wall Breakwater with Internal Horizontal Plate. *Journal of Engineering Mechanics*, *126*(5), 533–538.

- Zhang, X., & Srinivasan, R. (2010). GIS-based Spatial Precipitation Estimation Using next Generation Radar and Raingauge Data. *Environmental Modelling & Software*, 25(12), 1781–1788.
- Zhong, Z., & Wang, K. H. (2006). Solitary Wave Interaction with a Concentric Porous Cylinder System. *Ocean Engineering*, 33(7), 927–949.

